

Chapter 4

Tooling



**Frank Vollertsen, Joseph Seven, Hamza Messaoudi,
Merlin Mikulewitsch, Andreas Fischer, Gert Goch, Salar Mehrafsun,
Oltmann Riemer, Peter Maaß, Florian Böhmermann,
Iwona Piotrowska-Kurczewski, Phil Gralla, Frederik Elsner-Dörge,
Jost Vehmeyer, Melanie Willert, Axel Meier, Igor Zahn,
Ekkard Brinksmeier and Christian Robert**

F. Vollertsen (✉) · J. Seven (✉) · H. Messaoudi (✉) · S. Mehrafsun
BIAS—Bremer Institut für angewandte Strahltechnik GmbH, Bremen, Germany
e-mail: info-mbs@bias.de

J. Seven
e-mail: seven@bias.de

H. Messaoudi
e-mail: messaoudi@bias.de

F. Vollertsen
Faculty of Production Engineering-Production Engineering GmbH, University of Bremen,
Bremen, Germany

M. Mikulewitsch · A. Fischer · G. Goch
BIMAQ—Bremen Institute for Metrology, Automation and Quality Science,
University of Bremen, Bremen, Germany

G. Goch
University of North Carolina, Charlotte, USA

O. Riemer (✉) · M. Willert
Leibniz-Institut für Werkstofforientierte Technologien—IWT, University of Bremen,
Bremen, Germany
e-mail: riemer@iwt.uni-bremen.de; oriemer@lfm.uni-bremen.de

O. Riemer
LFM—Laboratory for Precision Machining, Leibniz Institute for Materials
Engineering—IWT, Bremen, Germany

P. Maaß · I. Piotrowska-Kurczewski · P. Gralla · J. Vehmeyer
Center for Industrial Mathematics, University of Bremen, Bremen, Germany

4.1 Introduction to Tooling

Frank Vollertsen

Forming as a shaping process, in which the tool is used as an analog memory for the workpiece geometry, requires precise tools. Especially in micro forming, it is not only the geometry of the basic tool bodies that plays a role, but also their surface topology, since it can be used considerably to control the material flow. The determination of the permissible tolerances has so far been an only empirically solved problem, whereby the applied trial-and-error methods in the development of tool kits end up being costly in the tool development for new workpiece geometries. The method of tolerance engineering described in Sect. 2.5 (Influence of tool geometry on process stability in micro metal forming) provides a remedy for this with regard to the scatter occurring as a result of the forming processes. In addition, the wear of the tools has to be taken into account, which is the topic in Sect. 4.2 (Increase of tool life in micro deep drawing). In Sect. 4.2 the various issues of tool wear are discussed, including the measurement and the results of the wear, which determine the tool life.

Knowledge about tool wear and protection methods like hard coatings (see Sect. 4.2 for test results) are used to design forming tools. For the manufacture of tool elements, which have typical dimensions of some mm and feature sizes in the range of some 10 μm , both new and enhanced standard methods are applied. One new method is the 3D laser directed chemical etching (laser chemical etching, LCM). This method was initially used in a 2D variant for cutting thin sheet from delicate materials like nitinol. The control of the cutting depth is limited in these cases to ensure an appropriate cutting depth for complete material separation. 3D shaping makes proper control of the removal process in all three dimensions necessary. Section 4.3 (Controlled and scalable laser chemical removal for the manufacturing of micro forming tools) introduces the process development towards a fast process for 3D removal without disturbances and a path planning method for optimized workpiece (i.e. tool) quality. One of the features of the process is the ability to generate sharp edges. Section 4.4 (Process behavior in laser chemical machining and strategies for industrial use) addresses one problem with the introduction of the LCM method into

F. Böhmermann · F. Elsner-Dörge · A. Meier
Labor für Mikrozerspanung—LFM, Leibniz Institute for Materials
Engineering—IWT, Bremen, Germany

I. Zahn
Bremer Goldschlaegerei (BEGO), Bremen, Germany

E. Brinksmeier · C. Robert
LFM Laboratory for Precision Machining, Leibniz-Institut für Werkstofforientierte
Technologien—IWT, University of Bremen, Bremen, Germany

I. Piotrowska-Kurczewski
University of Bremen, Bremen, Germany

industrial use. While the process is very attractive to industry as it uses a low power cw laser instead of expensive ultra-short pulse lasers, there might be problems due to the usage of sulfuric acid or phosphorus acid as etchants. Therefore, alternative etchants like citric acid and others were tested and are presented in Sect. 4.4. Section 4.4 also shows the feasibility of optimizing the cell layout for the process by FEM simulation. Computational fluid dynamics (CFD) is used to design the cells for a laminar and homogeneous flow across the workpiece.

While it is shown in Sect. 4.3 that sound control of the overall geometry of the tool is possible using laser chemical etching, the control of the surface microstructure appears to be difficult with this method. Due to the fact that the surface structure plays an important role in the material flow in (micro) forming, two sections present results on that. The standard method of tool-making by milling was investigated in respect to the development of surface structures and their prediction and control by optimization methods. The results in Sect. 4.5 (Flexible manufacture of tribologically optimized forming tools) show the structures that develop and how to predict the processing parameters, starting with the desired structure in an inverse optimization. One problem which had to be solved to master this inverse calculation was tool deflection by passive forces during cutting and tool wear during the milling process. Different tool wear models were tested and compared concerning accuracy and calculation time. Due to the small dimensions of the cutting tool, the deflection is much more pronounced than in conventional cutting. An additional size effect is the transition between the interaction modes of the tool and workpiece, i.e. ploughing or cutting appears, depending on the actual conditions. The related knowledge from Sect. 4.5 was used in Sect. 4.6 (Predictive compensation measures for the prevention of shape deviations of micromilled dental products) to optimize the milling of small free-form parts, i.e. dental prostheses. Like the work in Sect. 4.4, also the work in Sect. 4.6 was done together with industrial partners, having a discrete problem to be solved. This kind of knowledge transfer was also done in other work; see e.g. Sect. 2.4 (Conditioning of part properties) and Sect. 5.3 (Inspection of functional surfaces on micro components in the interior of cavities). The challenge in the work shown in Sect. 4.6 was to develop a method for optimized tool paths independent from the actual machine tool.

The second method for the control of the surface structure of tools was again a new method, which is elaborated in Sect. 4.7 (Thermo-chemical-mechanical shaping of diamond for micro forming dies). It is well known that diamond coatings and solid diamond tools (see Sect. 4.2) are suited for forming, especially for aluminum alloys, therefore the surface structure of such tools is of interest. On the other hand, diamond surfaces are very durable and therefore difficult to machine. Starting from the assumption that chemical wear of diamond cutting tools is dominant when cutting iron parts, experiments were conducted to use the diffusion of carbon into iron as a measure for structuring the diamond surface. This work led to a method based on a mechanism with thermal, mechanical and chemical aspects. The mechanisms and the achievable structures in diamond surfaces are explained in Sect. 4.7.

4.2 Increase of Tool Life in Micro Deep Drawing

Joseph Seven* and Frank Vollertsen

Abstract Micro metal parts are usually produced in large lot sizes at high production rates. In order to achieve sufficient product quality, excessive tool wear has to be avoided. In the micro range, so-called scaling effects and their influence on tool wear in micro forming have not been investigated so far. For the investigation, tests in micro deep drawing were carried out with metal sheets ($s < 50 \mu\text{m}$) of pure aluminum A199.5, a copper alloy E-Cu58 and stainless steel 1.4301. The failure mechanisms of the micro cups produced were identified as bottom fracture and cup wall damage, and tool wear was measured and characterized with optical measurements and EDX analyses. Moreover, micro cups can be produced by DLC- and PVD-coated tools in a dry forming process. To investigate the wear behavior in a continuous process, a forming tool was developed with an integrated blanking and deep drawing die. The tool wear was measured optically, and the wear mechanisms could be identified in a combined micro and deep drawing process. As a result, the tool could be modified by a manufacturing in selective laser melting and the tool life increased by 290%. Furthermore, a method for tool wear examination in long-term tests was developed. In lateral micro upsetting, the tool wear history can be examined by analyzing the formed product. Several tool materials and coatings were tested with up to 500,000 strokes.

Keywords Deep drawing • Micro forming • Tool wear

4.2.1 Introduction

A long tool life is an important requirement for cost-efficient mass production. The tool life defines how long the tool can be used in production, which determines the downtime and productivity. Wear mechanisms during macro forming experiments have been studied. However, experiments in the micro range revealed that so-called scaling effects [Vol08] influence the tool wear behavior [Gei01]. Scaling effects comprise technical and physical properties that do not correlate linearly with a linear change of the tool geometry. In deep drawing experiments, the influence of scaling (1–8 mm punch diameter) was first analyzed by Justinger et al. [Jus07]. They determined that the tool size influences the friction. The results show that the friction increases with a decreasing punch diameter. In order to understand the wear mechanisms in this range, Manabe et al. [Man08] manufactured a combined blanking and deep drawing die. With this tool, circular blanks were cut in a first step and in the second step deep drawn to micro cups. These tests were performed as single tests as well as under static conditions. However, the dominant tool wear mechanisms and the influence on tool life in mass production have not been investigated so far.

Thus, the goal of this work is to increase the tool life for cost-efficient mass production in micro deep drawing. First, the tool life is defined in simple micro deep drawing experiments. The tool life is determined by micro cup failures. To further analyze the tool, a setup is constructed that allows a continuous mass production of micro cups. A forming tool was manufactured with an integrated blanking and deep drawing die. In these long-term tests, the tool life was increased by the characterization of tool wear and the subsequent modification of the dies. Furthermore, a simple method was developed to determine exactly the tool life. In lateral micro upsetting, a wire is penetrated by a punch in a long-term test. As the tool geometry is reproduced on the formed wire, the tool wear history of the tool can be examined. This method allows a simple investigation of different tool materials and serves as a simplified method for the selection of the tool material.

It is shown that the wear mechanisms in deep drawing depend on the microstructure, which also influences the tool life. Moreover, it is demonstrated that the tool can be modified according to the dominant wear mechanisms, which increases the tool life. The experiments also reveal that it is possible to substitute the deep drawing with a fast and economical lateral micro upsetting method to investigate tool wear mechanisms and the influence on tool life.

4.2.2 Definitions

4.2.2.1 Tool Life

In this section, the tool life of micro deep drawing dies is defined by how long micro cups can be produced without cup failures. In deep drawing, there are two typical cup failures – bottom tears and wrinkle formations. These failures occur when the tool geometry or blank holder pressure is not chosen properly. Furthermore, the process conditions can be changed during the production as a result of tool wear [Hu10]. If so, the friction between the tools increases, which leads to higher process forces and bottom tears. Another cup failure is cup wall damage, which can occur due to worn areas on the die radius [Hu10]. In this case, the circular blank cannot be uniformly deep drawn, which results in a cup with non-uniform cup walls.

4.2.2.2 Dry Forming

Dry forming comprises forming technologies without using lubricants. For economic and geo-ecological reasons, it is important to use lubricant-free forming processes in future [Vol18]. In the dry forming process, the friction is typically reduced by surface modifications like coatings and structures. Especially in the

micro range, surface modifications have a great potential for efficient forming technologies [Hu11a]. Due to scaling effects, the influence of lubrication is reduced [Vol08]. Another advantage of lubricant-free forming is that an additional process step can be omitted, because cleaning of the lubricated products is not necessary. Cleaning of micro parts is especially difficult because the surface tension of the lubricant is relatively high compared to the macro range, which leads to the adherence of the micro parts.

4.2.3 Experimental Setups

4.2.3.1 Reciprocating Ball-on-Plate Test

A ball-on-plate test was applied to examine the friction coefficient of a sample [Hu11a]. The principle of the experimental setup is shown in Fig. 4.1.

A counter tool of X5CrNi18-10 mounted on a vertical spindle is moved to the workpiece and loaded with the force $F_z = 5\text{ N}$. The workpiece is mounted on a linear table, which is reciprocating at an oscillating distance of 5 mm and a velocity of 1 mm/s. The forces in x- and z-direction F_z and F_x are measured and recorded with a force sensor integrated into the spindle. The workpiece and the counter tool were cleaned before each experiment with 2-propanol. The experiments were carried out in dry conditions.

4.2.3.2 Micro Deep Drawing

Single tests in micro deep drawing were performed to identify the process parameters and characteristics of the wear behavior of micro deep drawing dies.

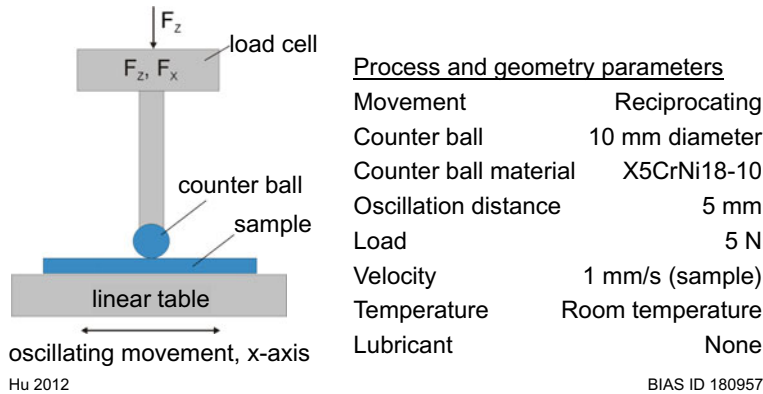
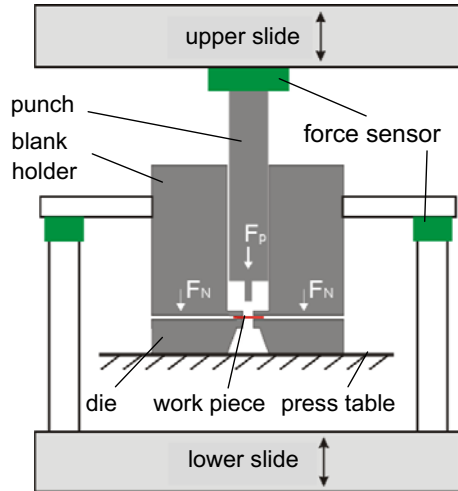


Fig. 4.1 Principle of the experimental setup for a ball-on-plate test

Fig. 4.2 Principle of experimental setup for micro deep drawing



Hu 2011

BIAS ID 180959

Furthermore, the tool life and the failure mechanisms are determined. The experiments were carried out on a highly dynamic micro forming press [Sch08b] with two axes. The machine axes are driven by electrical linear motors with a maximum acceleration of 10 g and a maximum velocity of 3.2 m/s. The positioning error is below 3 μm at maximum acceleration and the positioning error is below 1 μm up to a stroke of 8 mm. The tool for the deep drawing process [Hu10] is shown in Fig. 4.2. Circular blanks are applied as workpieces for the deep drawing process. The blank holder, which is moved by the lower axis of the press, applies a pressure on the workpiece. The circular blank is deep drawn through the punch to a micro cup. The punch is moved by the upper axis. Both the forming punch and the blank holder are linked to a piezo force sensor, type Kistler 9311B, which has a measuring accuracy of 0.01 N.

4.2.3.3 Combined Blanking and Deep Drawing

The continuous mass production of micro cups requires a forming tool that can both cut and draw a foil. In a first step, the tool cuts the foil to a circular blank and in the second step the circular blank is deep drawn to a micro cup [Hu10]. The tool is built into a highly dynamic micro forming press [Sch08b]. This press with the integrated tool can produce micro cups in high quantities with 200 strokes per minute. For the progressive production, a feed system and sample reels are deployed for the feed of the sample foils. Figure 4.3 shows the steps inside the tool [Flo14a].

First, the blank holder is open and the blank (red line) can be transported by the feed system. Then the blank holder is closed and a pressure is applied on the blank (step 2). The combined blanking and deep drawing die cuts a circular blank (step 3)

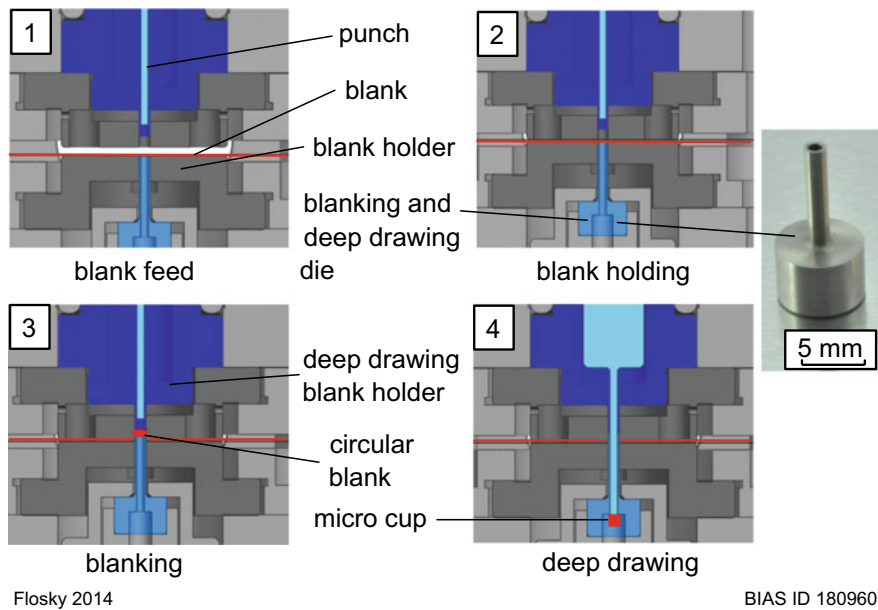


Fig. 4.3 Production steps in a combined blanking and deep drawing process

Table 4.1 Tool geometries for the combined blanking and deep drawing

Punch diameter	0.9 mm
Blanking diameter	1.7 mm
Inner diameter of deep drawing die	1.0 mm
Drawing gap	0.075 mm
Die radius	0.15 mm

and in step 4 the deep drawing punch deforms the circular blank. This production cycle is repeated until no micro cups can be produced any more. The tool geometries are listed in Table 4.1.

To investigate the running-in behavior at the beginning of the process, thermocouples are used and fixed in the tool [Flo14b]. The temperature is measured in a process with 400 strokes per minute without workpiece. Due to a wrong positioning of the tool, friction occurs through the contact between tool and tool guide. In the first 10 s, the temperature increases by 2 K and during the next 2 min there is a further increase of 1 K. Without positioning errors, the temperature remains almost constant and fluctuates with 0.5 K.

4.2.3.4 Lateral Micro Upsetting

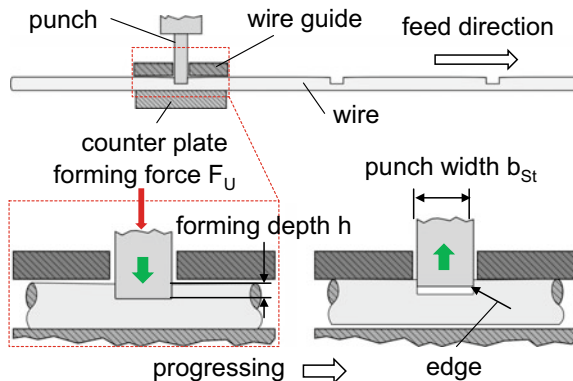
Wear measurements in long-term tests requires a tool, which includes a long installation of the setup as well as expensive micro tools for only one test series. Moreover, the punch force cannot be attributed to the wear behavior, as the punch force is influenced by different parameters separately. Therefore, a method was developed to investigate the wear behavior [Sev18]. A lateral micro upsetting is used. The setup and process of the method is shown in Fig. 4.4. A punch penetrates a wire with a defined forming depth and a measured forming force. Then the punch reverses. As this is a progressive process, the wire is fed by a feed system so that the punch can deform the wire in a continuous process with different strokes per minute. To ensure that the forming process is reducible, the wire is fed through the wire guide. Compared to the combined blanking and deep drawing process, the lateral micro upsetting can be built simply and fast, the sample can be attributed for each punch force, and the micro tools per test series are cheaper. This method is used for the wear examination of different tool materials and coatings in a continuous dry forming process. Additionally, the tool geometry is measured by negative reproduction in polyvinyl siloxane without dismounting the punch.

4.2.4 Measurement Methods

4.2.4.1 Confocal Microscope

An optical and contact-free 3D laser scanning microscope Keyence VK-X210 is used for the recording of the tool state and surface measurements. The microscope has a maximum total magnification of 24,000 with a measurement uncertainty of 1 nm. The pictures can be analyzed with the software VK-Analyzer.

Fig. 4.4 Principle of setup and process of lateral micro upsetting



4.2.4.2 Negative Reproduction of Tool Geometry with Silicone

During the continuous micro cup production, the tool needs to be investigated for any tool wear. Dismounting and mounting the blanking and deep drawing die takes too much time and causes additional downtimes. Moreover, it could lead to unintentional defects in the process. The tool wear could be influenced additionally by wrong positioning when remounting the die. So a quality control without dismounting and remounting is necessary [Flo15]. The negative reproduction with polyvinyl siloxane offers a fast and simple investigation, of which an example is shown in Fig. 4.5 [Flo15]. Compared to a dismounting and mounting (duration of up to 1 h) this method takes only a few minutes.

On both microscopic pictures, there is the same tool pattern. Wear characteristics like grooves, spalling and deformations are all reproduced and can be measured in the negative reproduction with a confocal microscope. The red circle in the original picture shows residues of the cleaning material. The forming accuracy of the silicone reproduction is proved by a nominal-actual comparison of the geometry between the original tool and tool reproduction [Flo15]. Wear characteristics are measurable down to 1 μm , but the roughness cannot be reproduced with this measurement method.

4.2.5 Materials

4.2.5.1 Workpieces

Aluminum EN AW-1050A (Al99.5), copper alloy Cu-ETP (E-Cu58) and stainless steel 1.4301 were used as workpiece materials. For the reciprocating ball-on-plate

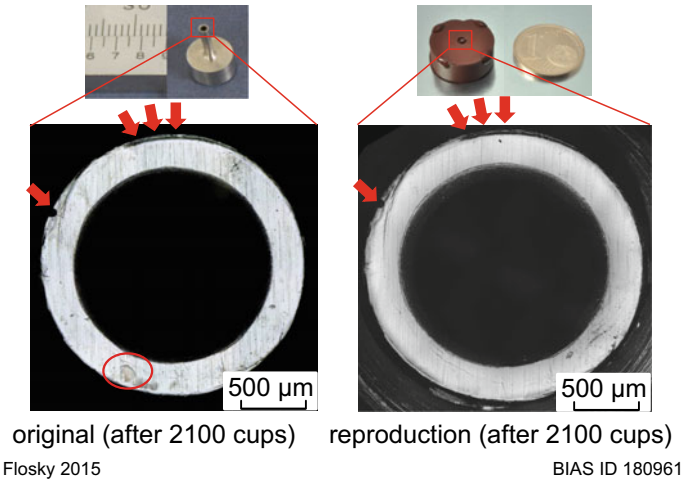


Fig. 4.5 Comparison between original tool (left) and tool reproduction (right)

test, the plates were made of 1.4301. In micro deep drawing, circular blanks of 1.4301 with a thickness of 25 μm were deep drawn. The circular blanks were cut by a nanosecond pulsed Nd:YAG laser with a wavelength of 1064 nm. In a combined blanking and deep drawing process, foils of Al99.5, E-Cu58 and 1.4301 ($s = 50 \mu\text{m}$) were cut to circular blanks, which were deep drawn to micro cups. In lateral micro upsetting, a 300 μm thick wire of 1.4301 was formed.

4.2.5.2 Tools

The tools in this work were made of conventional cold work steel 1.2379, Co–Cr alloy Stellite 21, high-speed steel 1.3343, powder metallurgical high-speed steel ASP23, hard metal MG30 and diamond. In the reciprocating ball-on-plate test, a ball of 1.2379 was on the plate. In micro deep drawing, the deep drawing die was made of 1.2379. Figure 4.6a shows a micro deep drawing die. Furthermore, a diamond deep drawing die is used for dry experiments.

In a combined blanking and deep drawing process, both 1.2379 and Stellite 21 were used for the manufacturing of a combined blanking and deep drawing die (see Fig. 4.6b). The blanking and deep drawing die of Stellite 21 was manufactured by selective laser melting (SLM) [Flo16]. A CAD model of the tool is transformed into a sliced model with a defined layer thickness and generated in a powder bed. The SLM technology is near-net-shape, but the tool must be micro milled and micro ground in a finishing process step. The advantage of the powder metallurgical materials used is the homogeneous microstructure with fine carbides. The relative density of Stellite 21 is above 99.95% and the hardness 38 HRC.

For the experiments in lateral micro upsetting, several materials can be used because of the simple geometry of the punch. Punches of 1.2379, ASP23, HSS and HM were manufactured.

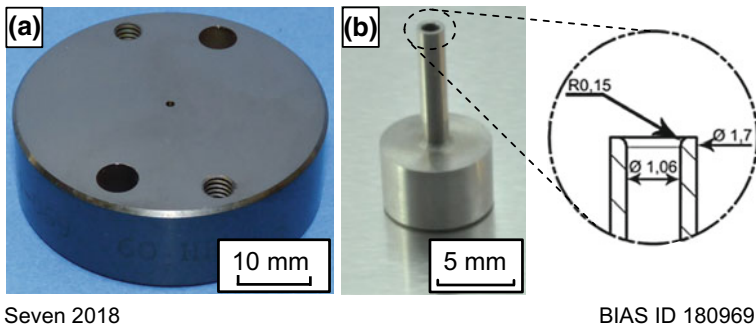


Fig. 4.6 Micro deep drawing die (a) and combined blanking and deep drawing die (b)

4.2.5.3 Coatings

Coatings are a potential method to reduce tool wear. In the ball-on-plate test, the plate of 1.2379 was modified with a DLC coating from Plasma-Consult (coating type PlascoDur). The hardness of the coating was measured before the tribotest with a Fischerscope H100VP XP from Fischer Types. The hardness of the DLC coating reached a maximum of about 2000 HV at the indentation depth of about 0.2 μm and decreased with further indentation down to 1400 HV at the indentation depth of 0.8 μm . This DLC coating was also used on a deep drawing die in micro deep drawing tests (see Fig. 4.7a). Furthermore, a PVD coating of TiN was applied on a deep drawing die and tested (Fig. 4.7b). For the lateral micro upsetting of the wire, hard metal punches were coated with the materials AlCrN, TiSiN, TiN and AlTiN (Fig. 4.7c).

4.2.6 Results

4.2.6.1 Characteristics of Tool Wear in Micro Deep Drawing

The tool life in the experiments is defined by the time micro cups within specifications are produced [Hu10]. For the experimental setup, the micro deep drawing is used. Figure 4.8 shows the maximal punch force and the failure rate of the micro cups depending on the number of experiments. The micro cups from the first 100 experiments have a failure rate of 0–20%, which might have resulted from the non-uniform properties of the thin foil used. After the first 100 experiments, there is a failure rate of 100%. The failures found are bottom tears and cup wall damage (see Fig. 4.8). Bottom tears are a result of a too high punch force [Hu10]. Tool wear causes higher friction, which leads to larger punch forces and bottom tears.

In the subsequent experiments, the worn area becomes smoother as a result of adhesion between the blank and tool, while some other worn areas are much worse [Hu10]. The result is a non-uniform distribution of friction along the forming

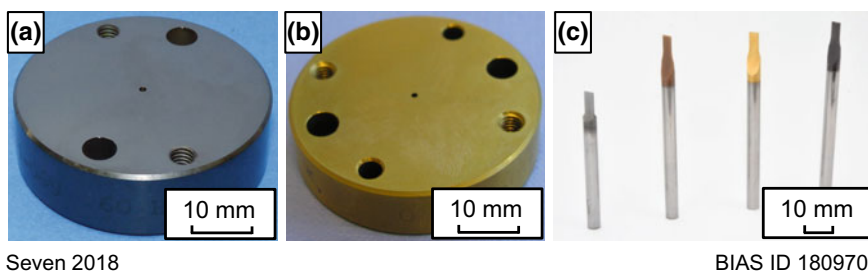


Fig. 4.7 DLC (a)- and PVD (b)-coated micro deep drawing dies and PVD-coated punches for lateral micro upsetting (c)

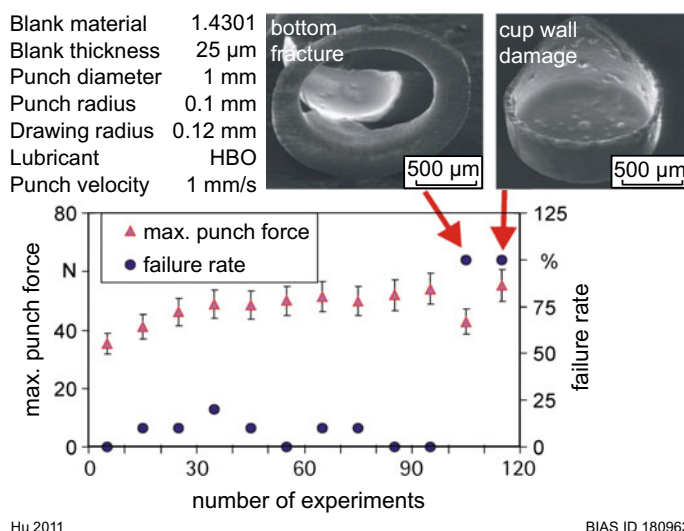


Fig. 4.8 Maximal punch force and failure rate of micro cups depending on number of experiments

zone. Thus, the circular blank is deep drawn non-uniformly into the die resulting in micro cups with cup wall damages. Figure 4.8 shows an example of a micro cup with cup wall damage. The maximum punch force of cups within specifications and with wall damage is almost equal. Therefore, tool wear cannot be detected by a change of punch forces and the tool life does not correlate with the maximum punch force.

The abrasion and adhesion between the tool and workpiece strongly influence the wear behavior. Therefore, the comparison of the tool wear is analyzed with a confocal microscope before and after several deep drawing cycles [Hu10]. The change of the roughness is visible in a before-and-after comparison and can be measured optically with the confocal microscope. Moreover, residues of the blank material on the draw radius caused by adhesion are measurable [Hu10]. Figure 4.9 shows the die radius of a micro deep drawing die with a residue of the circular blank. The residue is shown with a scanning electron microscope and characterized with an EDX analysis. The EDX analysis shows parts of Ni which are contained only in the blank material 1.4301 (X5CrNi18-10) and not in the tool material 1.2379 (X153CrMoV12). These residues cause cup wall damage as the circular blank is not properly deep drawn over the draw radius. Thus, the main wear mechanism occurring on the draw radius is adhesion.

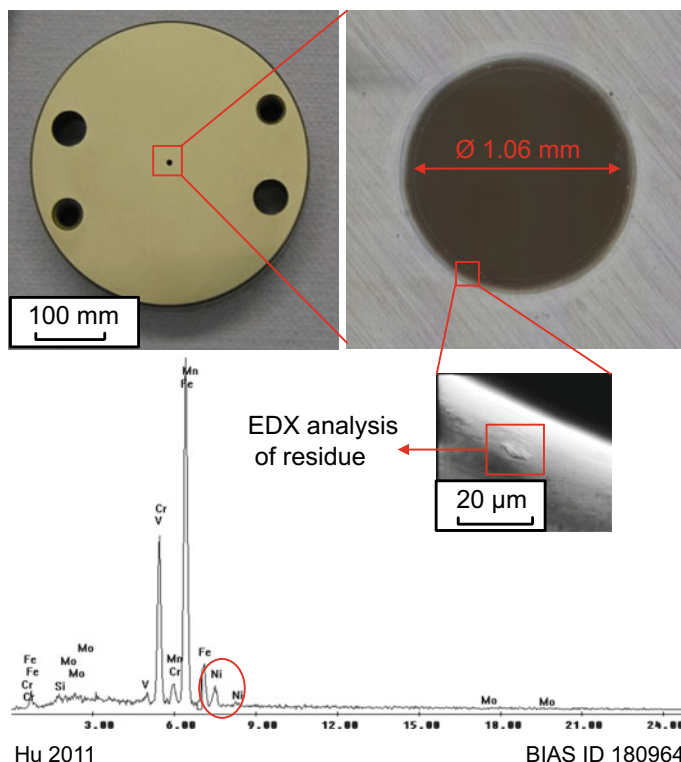


Fig. 4.9 EDX analysis of a residue on the draw radius of the die

4.2.6.2 Wear Behavior of Combined Blanking and Deep Drawing Dies

Compared to the single tests in micro deep drawing, there is an additional blanking of the foil in the combined blanking and deep drawing process. The blank is fed from the sample reel to the tool. With this setup, the combined blanking and deep drawing die produces micro cups with 200 strokes per minute.

In a continuous process with the lubricant Lubrimax Edel C from Steidle GmbH, 80,000 cups of Al99.5, 210,000 cups of 1.4301 and 300,000 cups of E-Cu58 could be produced [Flo14a]. After these strokes the tools failed. Figure 4.10 shows examples of the main characteristics of the wear behavior for the continuous blanking and deep drawing process. On the left, there is the surface of a new blanking and deep drawing tool. In the right picture, wear patterns are visible. The outer diameter is clearly smaller as a result of abrasive wear. Due to a wrong positioning of the tool, there is a bigger contact and stronger abrasion between the tool and blank holder. Other defects are edge disruptions caused through surface

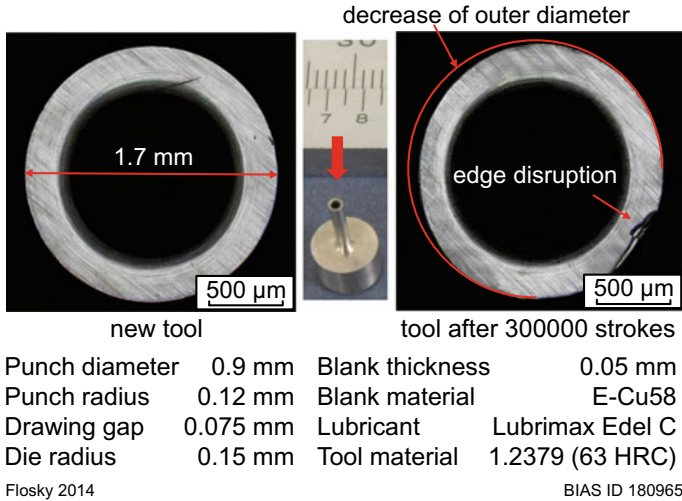


Fig. 4.10 New tool (left) and tool after 300,000 produced cups (right)

fatigue [Flo14a]. In cross-section, these tools show a high density of scattered pores and carbides with sizes up to 35 μm [Flo13]. Carbides in this range act as notches and can cause pitting and edge disruptions. For all tool material and workpiece material combinations, similar wear mechanisms were identified.

Furthermore, different drawing ratios were used for the production of Al99.5 cups [Flo13], one tool with a 1.6 mm outer diameter (drawing ratio 1.78) and one tool with an outer diameter of 1.7 mm (drawing ratio 1.89). The smaller tool (1.6 mm $\hat{=}$ 1.78) failed after 20,000 strokes and the larger one (1.7 $\hat{=}$ 1.89) after 80,000 strokes. So the wear of a smaller tool is larger. The smaller the tool surface the greater the influence of scattered carbides and pores [Flo13]. Moreover, a smaller tool surface leads to a higher contact pressure, which causes a higher dynamic stress. Related to the tool failure, it was observed that significant wear occurred just on the blanking edge and not on the draw radius.

The given results show that continuous micro cup production in a combined blanking and deep drawing is possible. The dominant wear mechanisms of the blanking and deep drawing die are identified with the decrease of the outer diameter through abrasion and edge disruptions on the blanking edge. The tool wear is mainly dependent on the microstructure, as carbides and pores can lead to pitting and edge disruptions. Compared to the failure mechanism in micro deep drawing, the tool life does not end through adhesion on the die radius. In a combined blanking and deep drawing process, the cup production is determined due to edge disruptions on the blanking edge.

4.2.6.3 SLM Tool in Combined Blanking and Deep Drawing

Carbides and pores in big sizes act as metallographic notches resulting in edge disruptions. The tool of the powder metallurgical material Stellite 21 generated by SLM [Flo16] has a homogeneous structure with fine carbides. The relative density of Stellite 21 is above 99.95% and the hardness is 38 HRC. In the following long-term test, the workpiece material Al99.5 ($s = 50\text{ }\mu\text{m}$) is tested with the lubricant Lubrimax Edel C and the same conditions as in Table 4.1. With the tool material 1.2379, 80,000 micro cups were produced. Compared to this, a total of 231,000 micro cups could be produced with the SLM tool, which means an increase of 290% [Flo16].

Figure 4.11 shows a comparison of the tool failures between the conventional (1.2379) and the powder metallurgical (Stellite 21) tool [Flo16]. The hardness of 1.2379 (63 HRC) is higher than the hardness of Stellite 21 (38 HRC). The harder material is more brittle, which is proved by the chippings on the blanking edge (red circle, 1.2379). Due to the broken blanking edge, the circular blank is cut tilted by the die. The tilted circular blank causes a micro cup failure as the tilted circular blank cannot be deep drawn properly [Flo16]. The surface and the edge of the SLM tool show some deformations. As Stellite 21 has a higher ductility and a fine microstructure, there are no edge chippings. The influence of edge chippings on

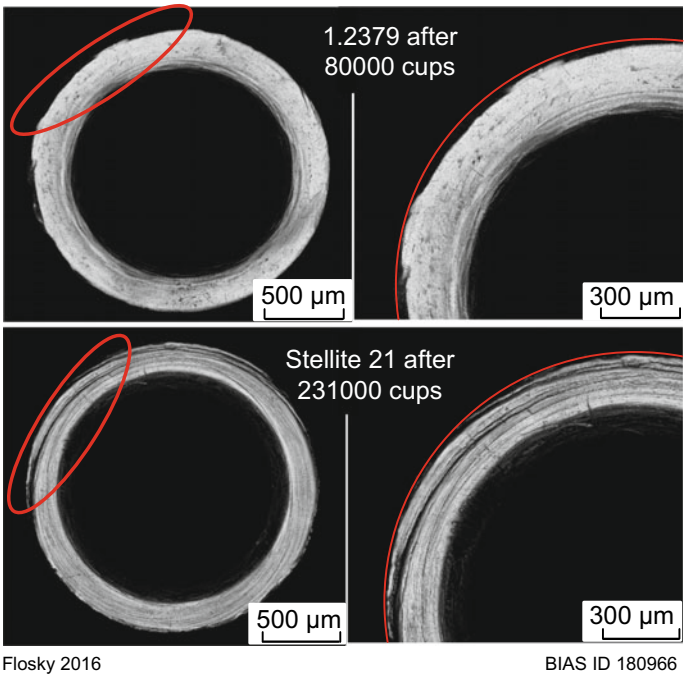


Fig. 4.11 Comparison of tool failures between 1.2379 and Stellite 21

tool life is greater than that of edge deformations because of the tilted cut of the circular blanks [Flo16]. Accordingly, tool materials with fine and homogeneous microstructures are required for the desired long tool life.

4.2.6.4 Dry Forming Processes

Coatings are a potential method to optimize the wear behavior. DLC and TiN coatings were used to reduce friction and wear. In a reciprocating ball-on-plate test, a sample of 1.2379 was tested with and without a DLC coating [Hu12] (see Fig. 4.12).

The tests were carried out in dry conditions. The balls are made of 1.4301 with a diameter of 10 mm. At a normal load of 5 N, the friction coefficient of the uncoated sample increases after 100 s steeply from 0.3 to more than 0.7. The friction coefficient for the DLC-coated sample is clearly lower with $\mu = 0.166$. Moreover, no damage due to the eggshell effect, cracks or spalling is observed on the DLC-coated sample [Hu12].

This DLC coating was applied on a deep drawing die to investigate the application in a dry micro deep drawing process. No damage on the produced micro cups was detected [Hu12]. The punch force of the DLC-coated die was measured and compared to a process with a lubricant and an uncoated die. In Fig. 4.13 the average punch force over the punch stroke is shown for both processes [Hu12].

The punch force of a lubricated process with an uncoated die is higher than a dry forming process with a DLC-coated die. Hence, the DLC coating can reduce the friction between the blank and die better than a lubricant. A similar result was achieved with a TiN-coated die, whereas the friction was higher than by a DLC-coated die [Hu11a]. Moreover, a dry and lubricated forming process was carried out with a TiN-coated die which reveals nearly no influence of the lubricant. According to the results, the DLC and TiN coatings can be used for application on micro deep drawing dies in dry forming processes. The punch force can be reduced

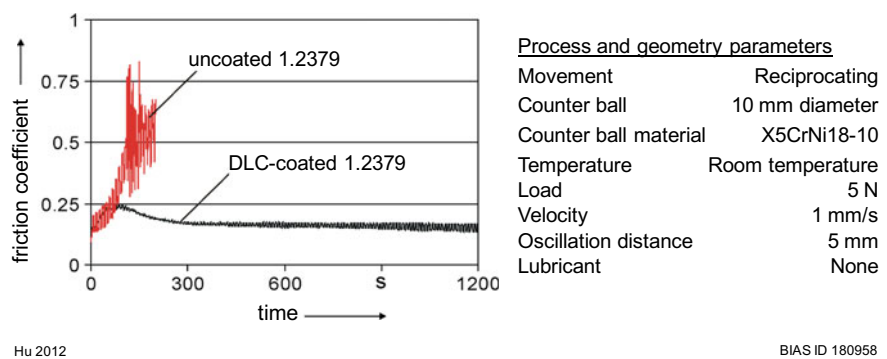


Fig. 4.12 Ball on plate test of uncoated and DLC-coated 1.2379

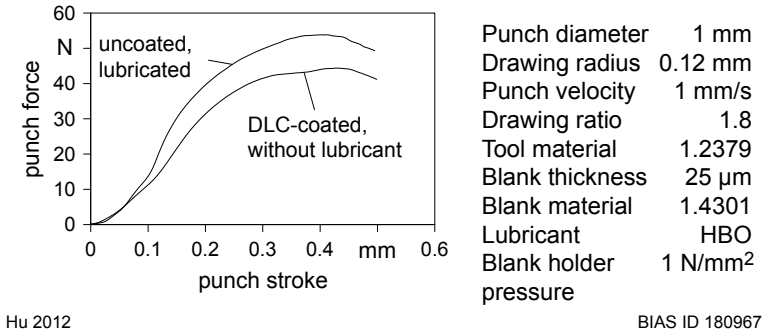


Fig. 4.13 Comparison of punch force versus punch stroke curves of micro deep drawing with DLC-coated and uncoated tools

in a dry process with a coated die better than in a lubricated process with an uncoated die.

Besides DLC- and TiN-coated deep drawing dies, a cubic diamond with the size of $3.5 \times 3.5 \times 2 \text{ mm}^3$ and a bore with 1 mm diameter (see Fig. 4.14b) are used as tool material for single experiments in deep drawing [Vol15]. Figure 4.14a shows the tool holder, in which the diamond is put and glued. The die radius is produced by an ultrashort pulse laser. In Fig. 4.14c, a cup of 1.4301 is shown with a diameter of 1 mm and a sheet thickness of 25 μ m. The cup can be produced with the diamond die without any cup failures. The advantages of diamond dies are the material costs and the tribological properties.

Especially in the micro range, much less material is needed for the production of tools. The disadvantage lies in the difficult manufacturing of diamond tools with complex geometry due to the difficult processing of diamond.

Next to ball-on-plate and micro deep drawing tests, cups of Al99.5 were produced in a dry blanking and deep drawing process [Flo14]. The same conditions as in Table 4.1 were applied with the tool material 1.2379 and a blank thickness of

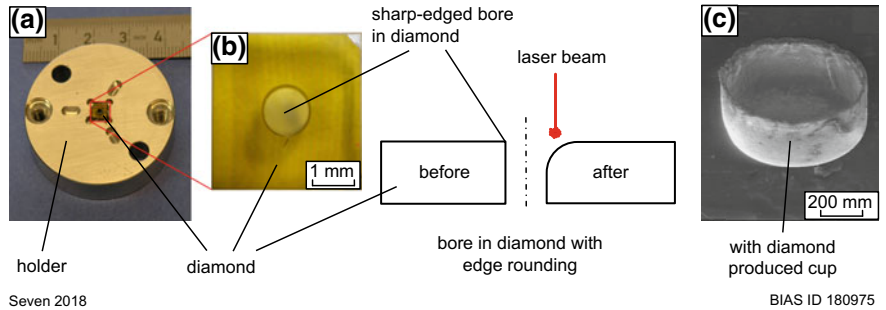


Fig. 4.14 Tool holder for diamond die (a), diamond die with laser-produced die radius (b) and with diamond die produced cup (c)

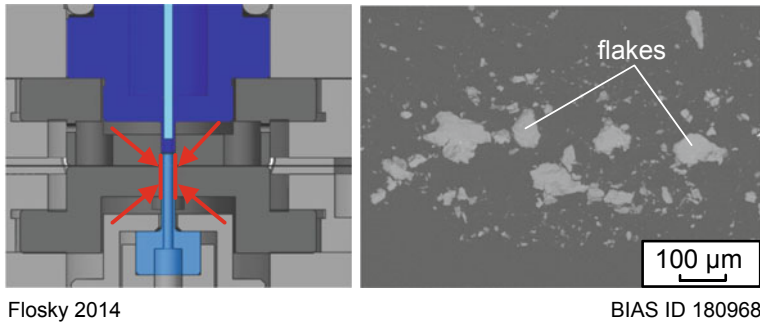


Fig. 4.15 Area influenced by flakes (left) and flakes on the surface of the blanking and deep drawing die (right)

50 μm . The result shows that micro cups can also be produced in a dry process, but the tool failed after 30 cups. Flakes are formed through the blanking process and get between the tool and blank holder (see Fig. 4.15, red line). Resulting from the higher friction, the blanking forces increase so that bottom tears appear and the tool fails. The flakes can be detected on the surface of the blanking and deep drawing die with an EDX analysis. To investigate the wear in a continuous test without the influence of flakes, the tool was cleaned with ethanol after every 10 micro cups. 4,300 micro cups were produced until tool failure [Flo14a]. Furthermore, observation of the quality of the dry formed micro cups indicates that there is no significant difference compared to micro cups produced with lubricant.

The results show that coatings can be used for reducing the friction in a ball-on-plate test and the punch force in micro deep drawing in dry conditions. Micro cups can be produced in a dry forming process with and without coatings. Due to the small tool size in the micro range, diamond tools are a cost-efficient method for producing micro cups. In a combined blanking and deep drawing process, a lubricant is necessary for the transport and removal of the flakes, as flakes cause higher friction and bottom tears. Thus, the tool life in a dry combined blanking and deep drawing process is mainly dependent on the removal of the flakes.

4.2.6.5 Wear Behavior in Lateral Micro Upsetting

In lateral micro upsetting, long-term tests were carried out to examine the wear behavior of several tool materials with and without coatings. The punches penetrate a wire with a forming velocity of 18 mm/s and 350 strokes per minute. The tool materials used are 1.2379, 1.3343, ASP23 and hard metal. Moreover, punches made of hard metal were coated with the materials AlTiN, TiSiN, TiN and AlCrN in a PVD process by Oerlikon Balzers. After 500,000 strokes, the tool wear was measured with a confocal microscope and compared in Fig. 4.16.

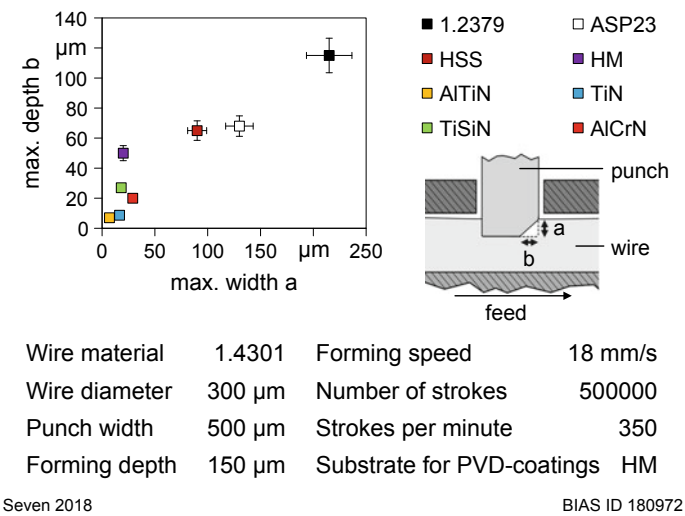


Fig. 4.16 Tool wear of different tool materials with and without coating after 500,000 strokes

The quality of the tool materials correlates with the expected wear behavior. 1.2379, with a hardness of 780 HV and an inhomogeneous structure, shows the highest tool wear after 500,000 strokes. ASP23 has a hardness of 880 HV and the structure is more homogeneous and finer than the structure of 1.2379. In the micro range, the quality of the structure is more important with a highly dynamic, permanent load (see Sect. 4.2.6.2). Thus, the tool wear of ASP23 is lower. Hard metal has both a high hardness (1520 HV) and a fine structure, which results in lower tool wear. The PVD-coated hard metal punches, due to the improved hardness (2300–3500 HV), show the best wear behavior. In a comparison of the coated punches, it was found that a surface with a higher roughness leads to higher tool wear. Moreover, a high influence of the substrate is observed by testing a punch of HSS (800 HV) with the coating AlTiN (3300 HV). The coating is damaged due to eggshell effects, which leads to a strongly progressive wear and results in the highest tool wear of the coated punches.

Analysis of the wire surfaces assumes that punch features are formed into the wire while penetrating the wire. The hard metal punch after 500,000 strokes is measured with a confocal microscope and compared to the wire surface of the 500,000th stroke (see Fig. 4.17).

On both surfaces, similar features as disruptions are visible. The yellow marked line shows a disruption with a depth of 5 μm . The feature within the red square contains a depth of 1 μm . As a result, by a penetration depth of 150 μm in lateral micro upsetting, punch features up to 1 μm are reproduced on the formed wire. Furthermore, the forming accuracy of the reproduction was determined by a comparison between the height profiles of the tool and wire [Sev18]. The reproduction of the geometry allows the investigation of tool wear for each stroke. As a

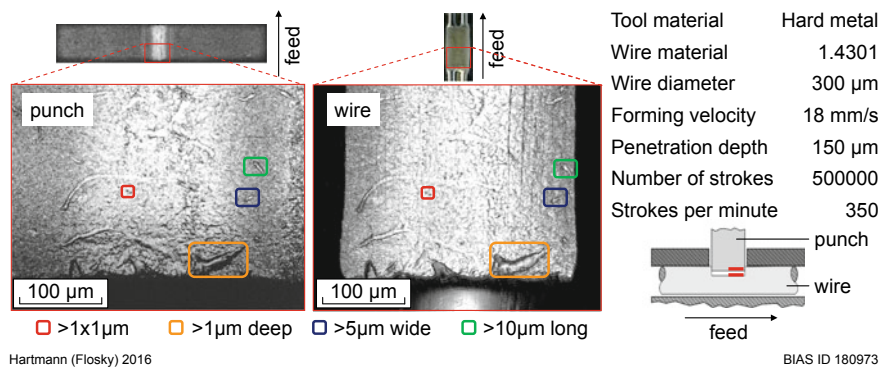


Fig. 4.17 Reproduction of punch features on wire surface in lateral upsetting

result, the tool wear can be tracked by the wire reproductions and the tool wear history determined in lateral micro upsetting. Through the tool wear history, it is possible to determine exactly when the wear occurred and exactly when the tool life is ended. In Fig. 4.18, two reproductions on the wire through the AlTiN-coated punch are shown in microscopic pictures.

The left wire reproduction belongs to the 200,000th stroke and the right one to the 250,000th stroke. After 200,000 strokes, no tool wear on the surface or edge can be measured, whereas after 250,000 strokes an edge disruption has occurred (see Fig. 4.18, white arrow). Hence, the punch is used in this experiment up to 200,000 strokes without any tool wear. To identify the exact stroke when wear first appears, the wire surface of each stroke has to be measured between the 200,000th and 250,000th stroke.

The investigations showed that lateral micro upsetting is a potential method to measure tool wear inline by using the analysis of wire reproductions. The tool geometry is reproduced on the wire with a forming accuracy below 1.5 µm. Thus,

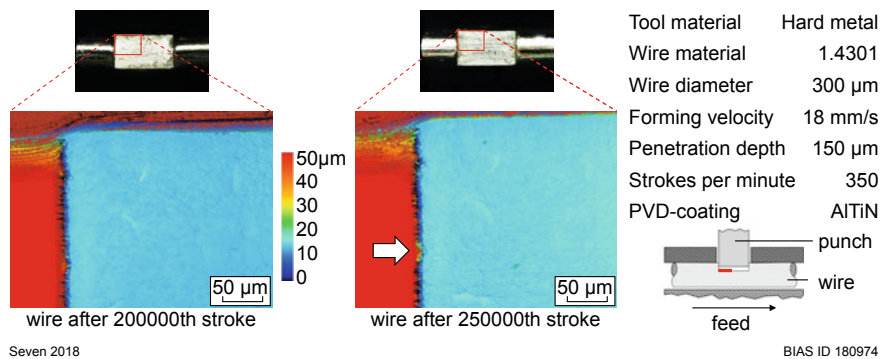


Fig. 4.18 Tool wear history of AlTiN-coated punch in lateral upsetting

the tool wear history can be analyzed by every wire reproduction of each stroke, which allows the exact determination of the tool life. Furthermore, there are several advantages of measuring tool wear by analyzing the formed product instead of analyzing the tool itself. No stopping of the production is necessary, which leads to reduced downtimes, the accessibility on the formed product is better, and no positioning errors occur from dismounting and remounting the tool.

4.3 Controlled and Scalable Laser Chemical Removal for the Manufacturing of Micro Forming Tools

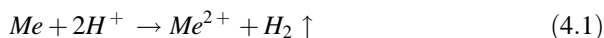
Hamza Messaoudi*, Merlin Mikulewitsch, Andreas Fischer, Gert Goch and Frank Vollertsen

Abstract Laser chemical machining (LCM) is a promising micro processing method that is based on laser-induced thermal activation of anodic material dissolution and enables a gentle and selective micro structuring of metallic materials. However, profound understanding of the removal mechanisms as well as comparative studies with competing processes regarding quality and efficiency are still required to use this process, not only for 2D cutting but also for 3D removal and to further widen the industrial acceptance of the LCM process. For this reason, an analytical modeling to calculate the temperature distribution at the workpiece surface is developed. The spatial correlation with the resulting removal geometry makes it possible to determine the limit temperatures for a disturbance-free regime, as well as the boiling-related gas bubble formation and adhesion as the main cause for the occurring removal disturbances. Moreover, a closed-loop quality control based on inverse process models and an adaptive controller is designed to compensate the deviations of quality features of single or sequences of removals. Using post-production measurements, it is shown that the desired geometry can be achieved with shape deviations of $2.4\text{ }\mu\text{m}$ within only 3 pre-production steps. Furthermore, comparison of the machining quality with micro milling reveals that the LCM process is characterized by a high dimensional accuracy and sharp edge radii ($11.2 \pm 1.3\text{ }\mu\text{m}$) especially for structure sizes $<200\text{ }\mu\text{m}$. Besides, additional examples of LCM-manufactured micro forming tools in different materials are presented to prove the process flexibility and diversity. Thereby, the achieved removal velocities in LCM of up to 1.25 mm/min in self-passivating metals are found to be comparable with those obtained in electrochemical machining.

Keywords Laser micro machining • Predictive model • Quality

4.3.1 Process Fundamentals

Laser irradiation is used in laser chemical machining as a localized and selective heat source that can induce a suitable thermal impact for the activation of a heterogeneous chemical reaction between a liquid environment and a metallic surface, and results in an anodic metal dissolution under the formation of hydrogen and water-soluble metallic salts following the chemical reaction [Bae11]:

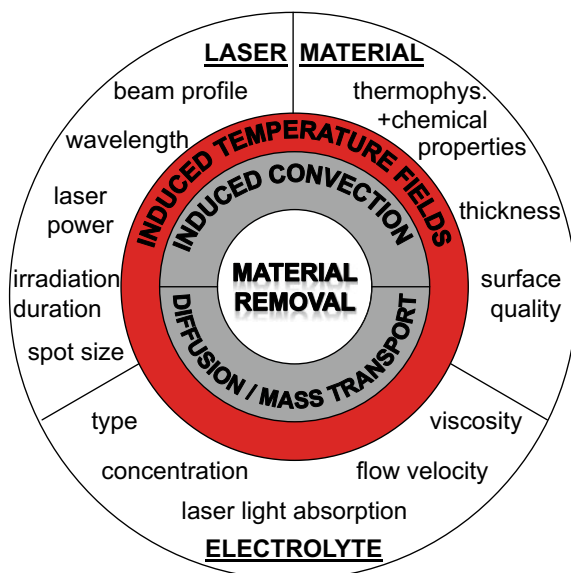


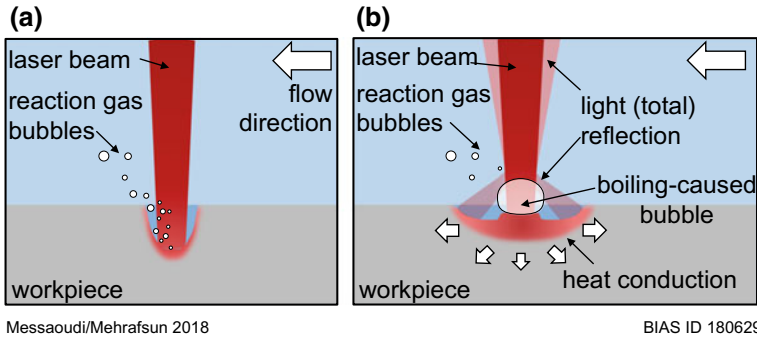
In LCM, the laser-induced heat impact can induce or enhance reactions at the metal-liquid interface via changes in the electrochemical Nernst potential. The locally induced temperature gradients result in the generation of a thermobattery, allowing a current flow within the metal between the center of the incident laser light and its periphery. Despite the low generated electromotive forces (some 0.1 V for a temperature rise of 100 K), the electric field strengths are very high due to the small battery dimensions [Bae11]. Thus, self-passivating metals lose their natural passivation property, allowing then the dissolution of the base material [Ste10].

Within the LCM process the laser-induced temperatures define both the proton activity within the redox reaction and the electrochemical potential at the workpiece surface [But03]. It is therefore evident that certain threshold temperatures are required in order to realize a material removal above the background etching rate ($<10^{-8}$ $\mu\text{m/s}$) [Now96]. Thereby, the laser-induced temperatures depend on different factors that include the laser, material and electrolyte parameters, as illustrated in Fig. 4.19.

Beside the temperature, the electrochemical potential also depends on the chemical activity of the dissolved metal ions and on the mass transport limitation [Ste10]. The latter mainly determines the removal speed within the aqueous electrolytes. Further, the convective flow also represents an important factor by determining the transport of reaction products as well as the provision and exchange of reactants. Increased convection can enhance the reaction rates by several orders of magnitude. At high laser intensities, electrolyte boiling can occur, resulting in the

Fig. 4.19 Schematic illustration of the relevant parameters and the dominant induced factors in laser chemical machining





Messaoudi/Mehrafsun 2018

BIAS ID 180629

Fig. 4.20 LCM process with **a** disturbance-free removal and **b** disturbed removal caused by adhering boiling-related gas bubble

formation of vapor gas bubbles. In addition to Yavas et al. [Yav94], it has been reported that the bubbles formed result in removal disturbances that impede the controllability of the LCM process [Meh13]. Figure 4.20 shows a schematic illustration of the effect of adhering boiling gas bubbles on the LCM process. Depending on its size and dynamics, the bubble affects the amount and distribution of the deposited laser energy differently. It can shield the workpiece surface against the electrolyte, resulting in a reduced material dissolution reaction [Mes17a] and in the deposition of metallic salts and oxides [Eck17a]. However, the thermal impact due to the laser-workpiece interaction results in a lateral heat conduction towards the periphery, which explains partially the W-like removal profile. With increasing gas bubble size, the effect of light (total) reflection is assumed to increase too due to the transition from an optically dense medium (electrolyte) into an optically thinner medium (gaseous volume of gas bubble). The adhering bubble can act like a scattering center and deflect a part of the incoming laser beam to its periphery (light deflection effect). While the shielding effect results in a reduced removal depth and the deposition of metal salts and oxides, the light reflections lead to a broadening or a dislocation of the removal cavity [Meh18].

4.3.2 LCM Machines Concepts

Depending on the production requirements, two LCM process variants are used. For micro tool fabrication and deep structuring, the electrolyte-jet based LCM (JLCM) method using a coaxial electrolyte jet-stream with respect to the laser beam is suitable (Fig. 4.21). The etchant jet-stream provides a fast exchange of reactants which is assumed to enhance the removal rates. The feed velocity v_{feed} of the workpiece is controlled by an xyz -linear stage that allows the workpiece to be adjusted with respect to the focal position [Meh13].

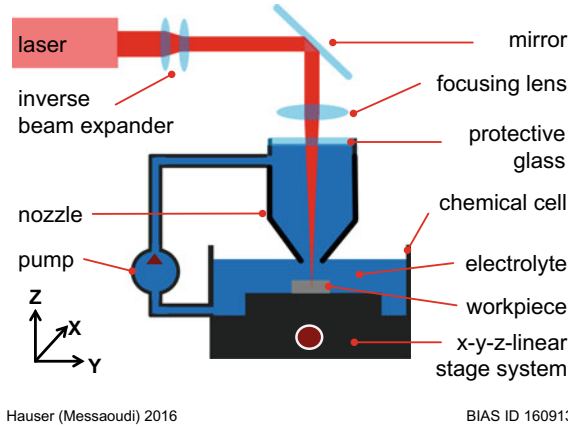


Fig. 4.21 Schematic illustration of the main components of the electrolyte-jet based LCM machine (JLCM)

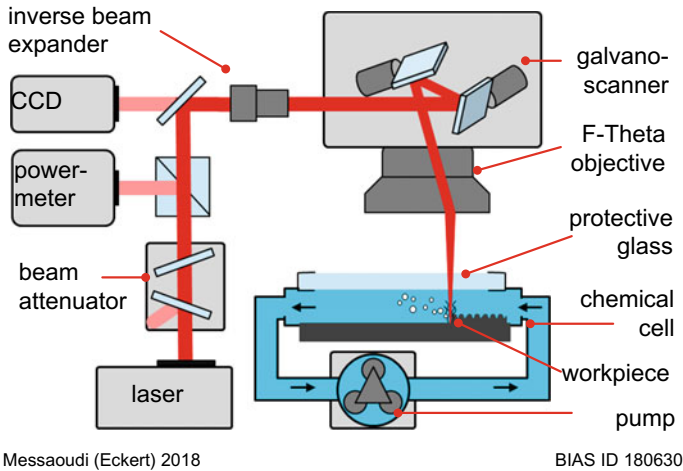


Fig. 4.22 Schematic illustration of the main components of the scanner-based LCM machine (SLCM)

For surface finishing and texturing, the scanner-based LCM (SLCM) can be applied, as depicted in Fig. 4.22 [Eck17a]. This is based on a closed process cell and a scanner system and allows flexible and safe machining of the metallic workpiece surface. In comparison to the JLCM setup, the workpiece is mounted in an etching chamber, where the electrolyte is pumped as a cross-jet through a $25 \text{ mm} \times 2 \text{ mm}$ cross-section with a maximum velocity v_{flow} of 2 m/s.

One of the key challenges in laser chemical processing is to ensure a controllable and homogeneous laser energy deposition on the workpiece, considering the

propagation throughout the aqueous etchant environment. In both concepts, fiber lasers emitting continuous-wave (cw) laser irradiation at a wavelength of $\lambda = 1080$ nm were used. The focus diameter d_{spot} of the incident laser beam can be varied between 24 and 74 μm in the JLCM machine and between 30.5 and 110 μm in SLCM using a flexible setting on an inversely positioned beam expander.

4.3.3 Influence of the Process Parameters on the Material Removal

4.3.3.1 Influence of the Electrolyte

The electrolyte is a decisive factor for the material dissolution reaction. Often, aqueous acid solutions such as phosphoric (H_3PO_4) and sulfuric (H_2SO_4) acids are used as electrolyte media. These ensure the highest efficiency, as was demonstrated by Nowak et al. [Now96] and Stephen et al. [Ste11]. However, more environmentally friendly electrolytes such as sodium chloride (NaCl) and sodium nitrate (NaNO_3) solutions were tested and compared with the acidic solutions [Hau15a]. The results will be discussed in more detail in Sect. 4.4.

Beside the nature and concentration of the electrolyte, the flow velocity v_{flow} and the wavelength-dependent transmission coefficient τ_E also represent important parameters in laser chemical removal. On the one hand, it was demonstrated that the increase of electrolyte feed rate from 0.5 to 20 m/s improves the aspect ratio (*depth/width*) in dependence on the laser power by factors up to 5 due to the ever narrowing cavities with the feed rate [Ste11]. On the other hand, the transmission coefficient of the electrolyte is mainly determined by the length of laser light propagation through the electrolyte [Mes14]. For example, the transmission coefficient τ_E decreases from 96 to 55% when the propagation path through a 5 molar phosphoric acid solution increases from 2 to 50 mm.

4.3.3.2 Influence of the Material

With respect to the electrolyte solution, the self-passivation of the material used is usually required in laser chemical machining. In many works, a wide range of materials has been determined to be well machinable. These included titanium [Hau15a], memory shape alloys (e.g. nickel-titanium alloys) [Ste10], stainless steel [Now96] and cobalt-chromium alloys (Stellite 21) [Mes17b].

Thereby, the amount and quality of the material dissolution is dependent on the chemical reactivity of the material elements. In [Hau15a] it was shown that the LCM of titanium in a 5 molar H_3PO_4 results in up to 39% higher removal rates and up to 30% deeper cavities in comparison with Stellite 21. This can be explained by the higher electronegativities of cobalt (63%) and chromium (25%), as the main

elements in Stellite 21, in comparison with that of titanium. Higher electronegativity impedes the tendency to release electrons and thereby slows down the speed of the chemical reaction.

Moreover, the formation of gas bubbles, which could be related to the chemical reaction and to the electrolyte boiling, is on the one hand dependent on the material used and on the other hand exerts a significant influence on the machining quality [Meh16b]. For example, the machining of titanium in phosphoric acid solution was found to be much more vulnerable to removal disturbances compared with that of stainless steel [Meh18]. This confirms also the experimental observation in [Meh16b], in which records of the interaction zone in both materials revealed higher gas bubble activity in titanium than in stainless steel. This can be traced back in part to the smaller size of the gas bubbles formed in stainless steel due to the higher atomic number of iron ($z_{Fe} < z_{Ti}$) [Qia14]. In addition, the adhesive Van-der-Waals force considering equal bubble size is lower in stainless steel than in titanium due to the lower related atom radius ($r_{Fe} < r_{Ti}$) [Bob08]. Both the lower gas bubble sizes and Van-der-Waals force explain the reduced shielding effect in stainless steel in comparison with titanium.

The machining of tool steels without a self-passivation layer was investigated in [Mes18a]. There, the background etching rates in high-speed steels (HSS) were determined within phosphoric and sulfuric acid solutions in dependence on the cobalt contents (8–12%), interaction time and electrolyte temperature. As depicted in Fig. 4.23, the highest background etching rates amount to 0.135 $\mu\text{m/s}$ at an electrolyte temperature of 60 °C after an interaction time of 1 h. Their continuous

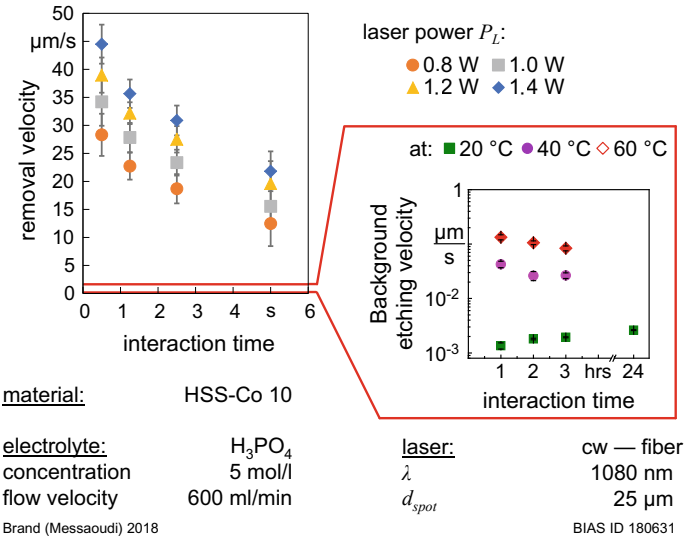


Fig. 4.23 Comparison between the LCM removal velocities and the background etching velocity of high-speed tool HS10-4-3-10 in 5 molar H_3PO_4 solution in dependence on the interaction time

increase at room temperature can be explained by an enhanced electrochemical potential due to the increased amount of metallic salts in the electrolyte solution and the availability of enough reactants. However, the background etching tends to get saturated at higher temperatures due to the fast consumption of reactants. In contrast, the laser-induced chemical machining results in a dependence on the parameters used in removal rates up to 50 $\mu\text{m/s}$. This provides evidence of the possible machinability of non-self-passivating metals without an external voltage supply and under consideration of the limited machining. Examples of laser chemically fabricated micro tools from HS10-4-3-10 are shown in Sect. 4.3.5.2.

4.3.3.3 Influence of the Laser Parameters

In previous works, the LCM of thin metallic foils was performed with an Ar⁺-laser (wavelength of 514 nm) [Now96] and a Nd:YAG-laser (wavelength of 1064 nm) [Ste11] in several metallic materials. Although different absorption coefficients, laser spot sizes and laser powers, the removal results show a strong dependence on the effective absorbed laser power P_{abs} as well as a negligible influence of the laser wavelength. The material removal is found to be scalable with the laser power P_L and the spot size d_{spot} following the quotient P_L/d_{spot} [Mes17a]. Thereby, the disturbance-free removal in different materials such as titanium, stainless steel or cobalt-chromium alloys within a 5 molar phosphoric acid environment was ensured at P_L/d_{spot} between 20 and 50 mW/ μm . The laser chemical machining of self-passivating metals takes place when a certain threshold laser power is applied. This was determined to be between 0.6 W and 0.7 W for LCM of titanium and stainless steel in a 5 molar phosphoric acid solution with a laser spot size of 30 μm [Mes17a]. Once the material dissolution is initiated, the material removal increases linearly in width and depth with the laser power. This is characteristic of a disturbance-free removal, which is labeled by a bell-like profile. A further increase of the laser power (over the electrolyte boiling point) results in removal disturbances [Meh13]. These are characterized by cross-sectional W-like or curved zig-zag 2D removal profiles, which are related first to the electrolyte boiling and second to the insufficient transport of reaction products, as well as the exchange of new reactants. Although reducing the processing quality, the removal rates in general continue to increase with the laser power [Ste11].

In addition, the feed velocity is also a key parameter in LCM process. Without consideration of the removal quality, it was shown that the removal depth decreases exponentially with the feed velocity [Ste09a]. Based on this, only feed velocities of <40 $\mu\text{m/s}$ are used during the JLCM process [Ste09a]. In contrast, a single scan with feed velocities >100 $\mu\text{m/s}$ leads, at suitable laser powers, to a non-visible material modification at the workpiece surface. However, the roughness peaks at the surface are chemically attacked and slightly removed. This is shown in [Eck17b], where a reduction of the surface roughness in titanium was achieved after some 10 scan repetitions with a feed velocity $v_{feed} = 2 \text{ mm/s}$. Thus, surface finishing can be realized with the combination of higher feed velocities and

multi-scans. It has to be mentioned that an areal mean roughness Sa of about $0.1\text{ }\mu\text{m}$ could be achieved when first the roughness peaks were removed and subsequently the remaining isolated surface valleys were leveled. This usually necessitates a removal depth of some $10\text{ }\mu\text{m}$, depending on the initial surface roughness [Eck18].

Furthermore, the influence of lateral overlapping should be considered for large-area LCM. Hauser et al. [Hau15] have shown that constant absorption conditions can be presumed only for the first removal path. Due to the changed surface topography, the removal in the following path is different. Enhanced absorption due to multi-reflections on the inner walls of the first path as well as higher electrolyte dynamics result in deeper removal in the subsequent path. Moreover, the suitable lateral overlapping is found to be dependent on the removal width of a single path and on the material used [Mes18a]. Due to the Gaussian laser beam profile, the roughness Sa at the cavity ground is usually $>2\text{ }\mu\text{m}$ [Mes17b]. This makes a subsequent finishing step necessary. Therefore, a two-step strategy with a roughing step based on single scans with velocities $<40\text{ }\mu\text{m/s}$ and a finishing step based on multi-scans with feed velocities $>50\text{ }\mu\text{m/s}$ is assumed to be the expedient approach [Mes18]. The results hereof are discussed in Sect. 4.3.5.

4.3.4 Strategies Towards a Controllable Laser Chemical Machining

4.3.4.1 Modeling of Laser-Induced Temperature Fields

Model Assumptions

As shown in Fig. 4.19, the laser-induced temperature field is dependent on different influence factors and is the subject of a complex interaction (chemically, physically and flow dynamics). To better understand the interrelations occurring, it is essential to precisely determine the induced surface temperature distribution. Therefore, the following assumptions were made in [Mes17a]:

- The laser beam is a TEM_{00} -mode with a Gaussian intensity distribution.
- The workpiece is moving with a constant speed v_{feed} in the x -direction.
- The material is assumed to be isotropic with temperature-independent properties. Moreover, phase changes, such as melting, are excluded.
- The effectively absorbed laser power $P_{\text{abs}} = P_L \cdot \tau_E \cdot \alpha_{\text{abs}}$, where P_L is the incident laser power, τ_E the electrolyte transmission coefficient and α_{abs} the absorption coefficient of the metallic material.
- Heat transfer into the etchant solution is considered through constant heat transfer coefficients H of the electrolyte.

Model Description

The thermal model developed is described in detail in [Mes17a]. It is based on the solution of the dimensionless heat equation $\Psi(X, Y, \theta, \tau)$ using a Green-function approach and provides the following description of surface temperature rise $T(x, y, \theta, t)$:

$$\begin{aligned}
 T = & \frac{P_L \cdot \alpha_{abs} \cdot \tau_E}{4\pi \cdot \kappa \cdot l} \cdot \int_0^\tau \frac{1}{1+4\phi} \cdot \frac{a}{(a-1)\sqrt{\pi\alpha^2\phi} + \sqrt{\pi\alpha^2\phi + a^2}} \cdot e^{-\left[\frac{(X-\mu\phi)^2 + Y^2}{1+4\phi}\right]} d\phi \\
 & - \frac{P_L \cdot \alpha_{abs} \cdot \tau_E}{4\pi \cdot \kappa \cdot l} \cdot \theta \int_0^\tau \frac{1}{1+4\phi} \cdot e^{-\left[\frac{(X-\mu\phi)^2 + Y^2}{1+4\phi}\right]} \\
 & \cdot \int_0^\infty \frac{a}{(a-1)\sqrt{\pi\left(\frac{Z'}{4\phi} + \Theta^2\phi + \Theta Z'\right)} + \sqrt{\pi\left(\frac{Z'}{4\phi} + \Theta^2\phi + \Theta Z'\right) + a^2}} \\
 & \cdot e^{-\frac{Z'^2}{4\phi}} \cdot e^{-\alpha Z'} dZ' d\phi
 \end{aligned} \tag{4.2}$$

Thereby, the first term in Eq. 4.2 represents the lossless heat equation, whereas the second one includes the heat losses when considering heat transfer into the electrolyte (i.e. $H > 0$). The list of the symbols used is illustrated in Table 4.4.

Modeling Results

On the example of machining titanium (3.7024) and stainless steel (AISI304) in a 5 molar phosphoric acid environment, the surface temperatures were calculated depending on laser power P_L and feed velocity v_{feed} . The main process parameters and the properties of the materials and electrolyte used are listed in Table 4.2.

Influence of Laser Parameters:

As described in Eq. 4.2, the induced surface temperature is proportional to the applied laser power. Thus, the surface temperatures increase linearly with the laser power. Moreover, it is found that the temperature rise becomes faster when the laser spot diameter is increased. At a power density of 50 kW/cm², the peak temperatures achieved in titanium amount to 51 °C, 88 °C and 130 °C with spot diameters of 30.5 μm, 68 μm and 109 μm, respectively [Mes17a]. This indicates that the laser intensity ($P_L/(0.25\pi \cdot d_{spot}^2)$) cannot be taken as a reference parameter. Instead, laser chemical machining is governed by a two-dimensional heating process that follows the quotient P_L/d_{spot} . This indicates that the surface temperature is one determinant factor in the LCM process. Regardless of the laser spot diameter, the thermal evolution of the LCM removal is unique for a defined electrolyte-metal combination [Mes17a].

Influence of Feed Velocity:

The thermal modeling reveals that the induced temperature fields with feed velocities up to some cm/s can be treated as quasi-static and quasi-symmetric.

Table 4.2 List of process parameters used for both modeling and experimental investigation

	Properties	Unit	Value
Titanium (3.7024)	Thermal diffusivity D	m ² /s	$6.8 \cdot 10^{-6}$
	Thermal conductivity κ	W/(m·K)	21
	Absorption coeff. at NIR α_{abs}	–	0.4
Stainless steel (AISI304)	Thermal diffusivity D	m ² /s	$4 \cdot 10^{-6}$
	Thermal conductivity κ	W/(m·K)	15
	Absorption coeff. at NIR α_{abs}	–	0.35
Laser beam	Wavelength λ	nm	1080
	Focus spot diameter d_{spot}	μm	30.5
	Feed velocity v_{feed}	μm/s	10 ... 200
	Laser power P_L	W	0.5 ... 2.5
Phosphoric acid (H ₃ PO ₄)	Concentration C	mol/l	2.5, 5, 7.5
	Boiling temperature $T_{Boiling}$	°C	104
	Flow speed v_{flow}	m/s	2
	Transmission coefficient τ_E	–	0.96
	Heat transfer coefficient H	W/(m ² ·K)	$3 \cdot 10^3$ (T < 90 °C) $5 \cdot 10^4$ (T > 90 °C)

In this velocity range, no significant influence either on the temperature rise or on the shape could be observed. Starting at velocities >10 cm/s, the temperature distribution becomes asymmetric. Here, it is observed that the temperature rise (for $x > 0$) is faster than the temperature decay (for $x < 0$). Moreover, the peak temperature decreases with the feed velocity and is located farther and farther behind the center of the passing laser beam at $x < 0$.

Influence of Material:

The comparison of material-related energy conversion indicates that, despite similar absorption coefficients, the heat impact in titanium is lower than in stainless steel due to the higher thermal conductivity ($\kappa_{titanium} > \kappa_{steel}$). Moreover, the difference in the peak temperatures achieved augments with either increasing the laser power or reducing the feed velocity.

Influence of Electrolyte:

In the thermal modeling the influence of the electrolyte is considered through the transmission coefficient τ_E and the heat transfer coefficient H . For the definition of the heat transfer coefficients, the water flow in a micro pipe was chosen as a reference case due to the micro range of the interaction area ($d_{spot} < 110 \mu\text{m}$). Depending on the electrolyte temperature, two different heat transfer coefficients H were defined [Whi11]:

- $H = 50,000 \text{ W}/(\text{m}^2 \cdot \text{K})$ for the case of water boiling. It was applied for temperature distributions with $T_{model,peak} > 90 \text{ °C}$. De Silva et al. [Sil11b] have shown that the risk of electrolyte boiling is extremely enhanced starting at 90 °C.

- $H = 3,000 \text{ W/(m}^2\cdot\text{K)}$ representing an enforced convection within a moderate water flow. This value was applied for temperature distributions with $T_{\text{model,peak}} < 90 \text{ }^\circ\text{C}$.

The modeling results in [Mes17a] show that the heat transfer into the electrolyte during the LCM can be neglected for surface temperatures between 20 and 200 $^\circ\text{C}$. The calculated thermal losses in titanium were between 1.5 and 3 K with $d_{\text{spot}} = 30.5 \text{ }\mu\text{m}$ and between 4 and 10 K with $d_{\text{spot}} = 109 \text{ }\mu\text{m}$.

Experimental Validation

Limit Temperatures for a Disturbance-Free Removal:

A spatial correlation of the temperature distribution with the removal profiles of the machined cavities, as depicted in Fig. 4.24, can be used to define the process characteristics. Thereby, the temperature at the distance $w_{\text{rem}}/2$ (half of the removal width) corresponds to the lower limit temperature $T_{R,\text{min}}$, at which the laser chemical machining is initiated. Moreover, the temperature at the maximum obtained depth ($T_{(x=\text{depth,max})}$) represents the upper limit temperature $T_{R,\text{max}}$. In comparison with the temperature at the center position ($T_{(x=0)}$), it can be stated that the removal is disturbance-free as long as $T_{R,\text{max}} = T_{(x=0)}$. In contrast, a removal disturbance can be presumed if $T_{R,\text{max}} < T_{(x=0)}$, because the maximum removal depth is shifted from the center position $x = 0$ to the periphery [Mes17a].

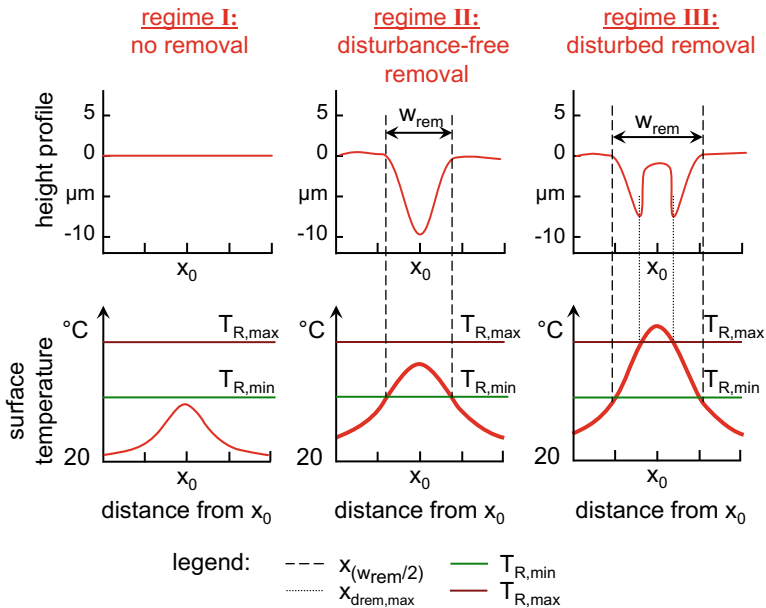


Fig. 4.24 Schematic illustration of the spatial correlation between removal profile and temperature distribution at the workpiece surface

Figure 4.25 shows the LCM limit temperatures $T_{R,min}$ and $T_{R,max}$ determined for titanium and stainless steel in a 5 molar H_3PO_4 -environment. Within the identified disturbance-free regimes it is found that the lower limit temperature $T_{R,min}$ amounts on average to $65\text{ }^{\circ}\text{C} \pm 5\text{ }^{\circ}\text{C}$ in titanium and $59\text{ }^{\circ}\text{C} \pm 4\text{ }^{\circ}\text{C}$ in stainless steel. Further, it is observed that the removal width within the disturbed removal regime becomes broader and correlates with lower temperatures down to $47\text{ }^{\circ}\text{C}$, especially in titanium, which can be explained by light deflection occurring on adhering gas bubbles in titanium (see Fig. 4.20). This additional heat impact, which is not included in the thermal modeling, leads to a broadening of the removal cavity and to a shift of the limit temperature $T_{R,min}$.

The upper limit temperature $T_{R,max}$ that is defined to be located at the maximum depth is compared with the temperature $T_{(x=0)}$. There, it is observed that $T_{R,max}$ is equal to $T_{(x=0)}$ within the disturbance-free removal (between 0.75 W and 1 W for

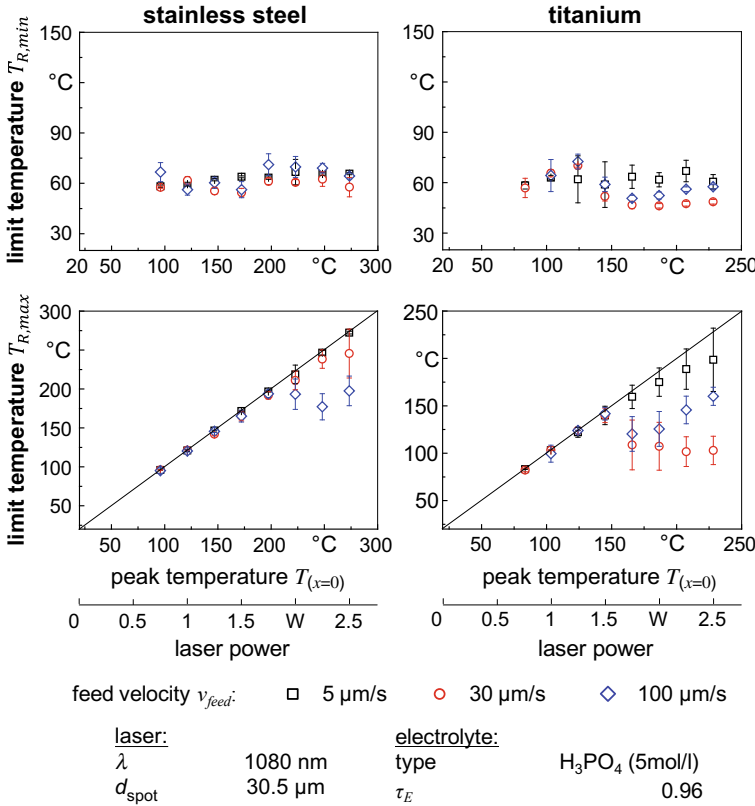


Fig. 4.25 Correlated limit temperatures $T_{R,min}$ and $T_{R,max}$ the laser chemical removal of titanium and stainless steel in a 5 molar phosphoric acid solution; for temperatures $>150\text{ }^{\circ}\text{C}$ the influence of adhering gas bubbles is not considered

stainless steel and 0.75 W and 1.25 W for titanium), which means that the maximum depth is located at the center of the incident laser beam. In contrast, the two materials reveal different behaviors when removal disturbances occur. In titanium it is observed that $T_{R,max} < T_{(x=0)}$ at induced temperatures $T_{(x=0)} > 145$ °C, which corresponds to the transition boiling regime and indicates a W-like removal profile with a shift of the maximum removal away from the center.

In contrast, the first deviations from $T_{(x=0)}$ are observed in stainless steel starting with temperatures >150 °C. However, $T_{R,max}$ remains located close to the center position $x = 0$ up to higher laser powers of 2 W. Thereby, $T_{R,max}$ decreases with the increased feed velocity. At a laser power of 2.5 W $T_{R,max}$ -values of 272.5, 245.5 and 197.5 °C were determined at feed velocities of 5 $\mu\text{m/s}$, 30 $\mu\text{m/s}$ and 100 $\mu\text{m/s}$, respectively. These high temperatures are assumed to be related to a lower influence of electrolyte boiling at the surface of stainless steel, as described in Sect. 4.3.3.2.

In general, it can be summarized that the induced temperature distribution determines the interaction area and thereby the removal zone, as seen from the fact that the removal widths remain constant. In contrast, the removal evolution into the material, represented by the removal depth, is mainly determined by the interaction time, which is inversely proportional to the feed velocity and can be described as:

$$\text{interaction time } t_{inter} [s] = \frac{\text{spot size } d_{spot} [\mu\text{m}]}{\text{feed velocity } v_{feed} [\mu\text{m/s}]} \quad (4.3)$$

As demonstrated in [Meh18], the removal depth increases following a nearly exponential function with the rising interaction time (i.e. it decreases exponentially with the feed velocity). However, the removal velocity shows a different behavior. For self-passivating materials, the highest removal velocities are obtained at interaction times around 1 s. This will be discussed in more detail in Sect. 4.3.6. Furthermore, it has to be noticed that the increase in removal depth slows down and tends to be saturated independent of the interaction time at induced surface temperatures >140 °C, which is characteristic of the beginning of film boiling e.g. gas bubbles adhering on the metal surface.

4.3.4.2 Quality Control System for Laser Chemical Machining

Factors such as laser-energy absorption dynamics, heat accumulation, chemical reactions, and hydrodynamic transport phenomena cause various disturbances during the material removal process of laser chemical machining (LCM) [Zha15]. In order to achieve competitive shape and surface quality in applications such as rectangular micro-forming dies, where the produced bottom surface requires a certain flatness and roughness, control of the workpiece manufacturing is imperative. The design and application of a high quality control scheme for the LCM application are presented in this section.

Control Specifications

The aim of LCM quality control is to govern the geometry of a single removal path as well as the workpiece geometry produced by multiple removals. Thus, a cross-path control is required for the entire process chain. Considering the geometry G of the workpiece as the superposition of multiple removal paths, it is difficult to achieve direct control of the workpiece quality features by adjusting all the process input parameters from every removal path, because of the many degrees of freedom and the non-linear process behavior.

In order to reduce the degrees of freedom, only the shape parameters A of every path $j = 1, \dots, N_{path}$ are varied in the control loops. The shape parameters of N_{path} paths are gathered as the control variables $A = (a_1, \dots, a_{N_{path}})$ and the process input parameters of multiple paths as the actuating variables $U = (u_1, \dots, u_{N_{path}})$.

The general cross-process quality control concept shown in Fig. 4.26 has already been successfully applied in different process chains, such as a bearing ring production process chain [Zha12]. An inverse process model and a process chain prediction present the basis of the feed-forward control. For this purpose, the shape parameters of the single removal and the geometry of the workpiece are characterized and a mathematical model is derived to describe the relationship between the shape and the process input parameters. Both are combined with optimization algorithms to realize an inverse model and a process chain prediction based on artificial neural networks (ANN).

The feedback loop consists of a post-production measurement, an observer for rebuilding the control variables from the measurements, and an adaptive P-controller to achieve stability over the entire operating range of the LCM process. It should be noted that the quality control for LCM was implemented production-discrete, because the development of an in situ measurement technique is still the focus of

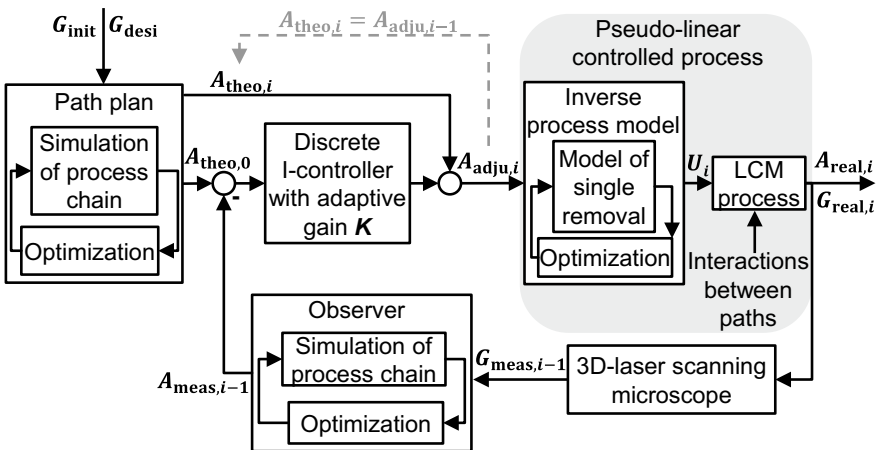


Fig. 4.26 LCM quality control concept with path plan, controller, inverse process model and observer

ongoing research [Mik17]. Production-discrete in this context means that the control loop is closed by post-production measurements with a confocal microscope after each production iteration $i = 1, \dots, N_{prod}$. With this control loop, the process parameters are continuously optimized for the subsequent productions.

The challenges to be faced by this control concept are as follows:

- The LCM process is a multi-inputs-multi-outputs (MIMO) system.
- The interactions between overlapping removal paths are complex and partly unknown.
- The relationship between the process input parameters (actuating variables U) and the shape parameters of one removal (control variables A) are non-linear and can cover a broad range.

Cross-Path Interactions:

Due to the effective thermal energy distribution, the removal cross-section of the processed geometry is assumed as a superposition of single Gaussian curves. However, the angle-dependent laser energy absorption as well as the thermal and hydrodynamic condition can lead to a reduced removal rate at a sloped surface (flank), compared to a flat surface. Hence, a cavity produced by a simple overlapping of single paths does not necessarily meet the predicted geometry. Figure 4.27 shows a measured cavity cross-section (black curve) of two overlapping removal paths produced by identical process parameters with a center position distance x_d of 50 μm [Zha15]. The cavity cross-sections produced are measured by a confocal scanning microscope and show a distinctive deviation from the removal cross-section predicted by a process chain simulation with overlapping removal paths.

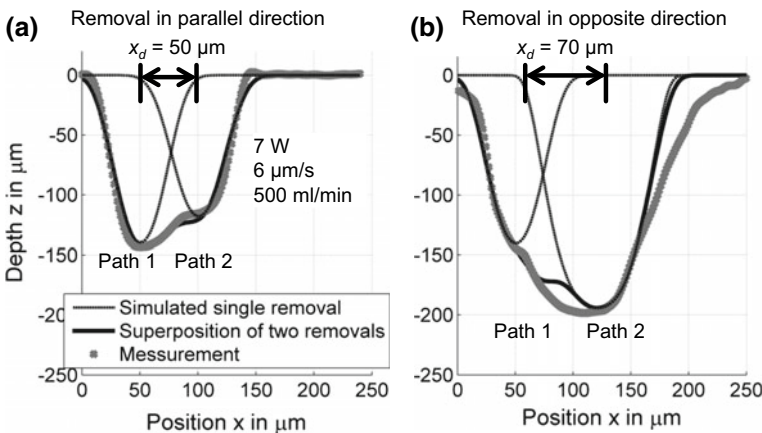


Fig. 4.27 Angle-dependent flank effect: Measured cross-section (black) and superposition (gray) of the Gaussian approximated removal paths with a distance x_d of 50 and 70 μm as well as the simulated prediction without consideration of the flank angle (dashed)

To produce a flexible geometry, an optimal combination of overlapping removal paths is calculated by minimizing the deviation in the z direction between the cross-section of the desired geometry G_T and the superposition G_S of the approximated individual Gaussian curves, considering the influence of the flank angle or the center position distance by a functional dependence. In this way, the path planning acts as a cross-process quality controller. Within the path planning, the flank effect is compensated by adjusting the quality features, the Gaussian form variables, in the removal depth and width.

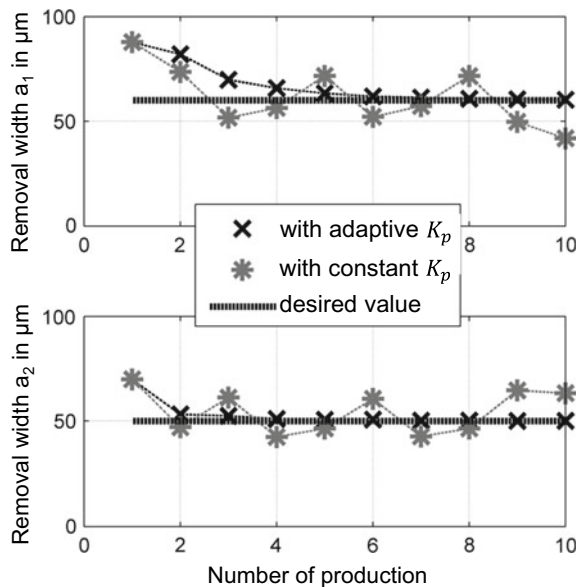
Adaptive Gain Controller:

According to the calculated shape deviations of every path in the previous production, the process parameters for the subsequent production are adapted by the quality controller. A P-controller with proportional gain K_p is the simplest solution for this MIMO control system that is able to cope with the non-linear behavior of the LCM process. Thereby, an appropriate gain is based on a compromise between control speed and stability, as a low value of K_p normally results in a stable system, but a slow control speed. The use of a controller with a constant gain factor K_p for the LCM process has revealed that the stability and a satisfactory control speed could not be ensured simultaneously in the whole operating area. For this reason, an adaptive controller with the gain $K_p(i)$, was designed considering the previous set value of the shape parameters $A_{theo}(i-1)$ and the measured shape parameters $A_{meas}(i-1)$. This adaptive controller was verified by a simulated production shown in Fig. 4.28 and reveals a stable and fast control.

Experimental Validation

The quality control concept developed was validated by producing a micro forming tool having a rectangular shape $(500 \times 200 \times 100) \mu\text{m}^3$ that needs a processing

Fig. 4.28 Verification of the controller with a single path production. The set values of the shape parameters are $a_1 = 60 \mu\text{m}$ and $a_2 = 50 \mu\text{m}$. The process chain simulation is applied



time of about 5 min. The quality features characterized were the removal depth d_{rem} (based on the arithmetic mean of the measured depths z_m at the positions x_m) as well as the cross-sectional straightness S of the produced bottom surface (with heuristically defined boundaries). The straightness is determined using a Chebyshev approximation [Goc08]:

$$S = \min_{c_1, c_2} \left\{ \lim_{n \rightarrow \infty} \sqrt[n]{\sum_{m=1}^M e_m^n} \right\} \quad (4.4)$$

where e_m describes the orthogonal distance of the points (x_m, z_m) from a linear function $z(x) = c_1 x + c_2$. The manufacturing tolerances of these quality features were defined to be $\Delta d_{rem} = \pm 5 \mu\text{m}$ and $S = \pm 2 \mu\text{m}$. The path plan and the mean cross-sections of the first three control iterations are shown in Fig. 4.29. The resulting mean depth $d_{rem} = 101.1 \mu\text{m}$ and the straightness $= 1.2 \mu\text{m}$ are determined as the average values obtained from different cross-sections. After two optimization iterations (i.e. two discrete productions), a workpiece with shape deviations that satisfy the manufacturing tolerances was produced. The maximum deviation of the mean depth, for instance, could be reduced from the initial $33.1 \mu\text{m}$ (without closed-loop control) to $2.4 \mu\text{m}$ (with closed-loop control) [Zha17]. The shape deviations of the produced micro dies from the desired geometry are thus shown to be distinctly reduced with the quality control developed.

This result demonstrates that the process-discrete control system, which is based on inverse models and a P-controller with adaptive gain, is able to cope with the non-linearity of the LCM process. It ensures a stable processing quality and exhibits satisfactory control speed and shape deviations. However, due to the reduced degrees of freedom, the control of single paths for complex geometries such as edge rounding is no longer possible. In addition, the post-process control system cannot

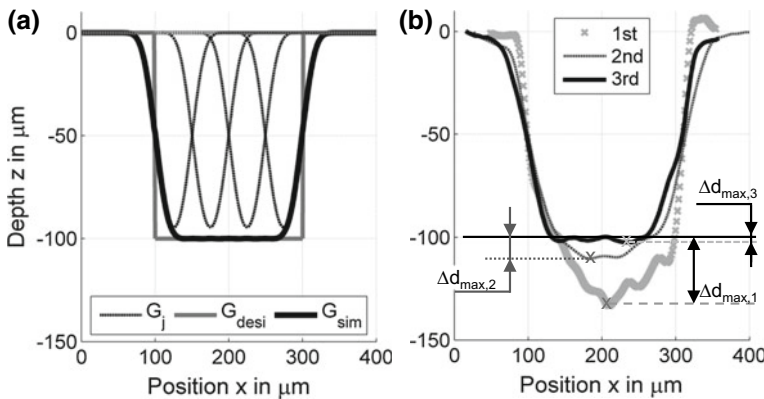


Fig. 4.29 Productions of a rectangular die using 4 paths: **a** path plan; **b** mean cross-sections of the produced workpieces for the first 3 optimization loops of the quality control [Zha17]. The maximum depth deviations for the 3 produced profiles are $\Delta d_{max,1} = 33.1 \mu\text{m}$, $\Delta d_{max,2} = 10.3 \mu\text{m}$ and $\Delta d_{max,3} = 2.4 \mu\text{m}$

compensate random deviations along the material feed direction within one removal path. Therefore, a real-time quality control including in situ metrology techniques should be targeted in the future.

4.3.5 Tool Fabrication

4.3.5.1 Manufacturing of Stellite 21 Micro Forming Dies

Manufacturing Task

As demonstrated in the previous section, laser chemical machining can be controlled and its quality can be predicted precisely. The developed and validated temperature and control models represent two key aspects towards the high-quality manufacturing of metallic micro parts. Another important aspect is the experimental characterization of the quality achieved. Next, the tool material Stellite 21 (a cast cobalt-chrome alloy) is used to show the dimensional accuracy and the surface quality of laser chemically machined forming cavities, which are of interest for micro cold forging. Here, square micro cavities with side lengths of 150 and 300 μm and depths of 60 μm were targeted [Mes18].

To examine the manufacturing quality, the geometrical properties (side length L_K , removal depth d_{rem}) and the shape accuracy were recorded and characterized using a laser scanning confocal microscope (Keyence VHX970) and a scanning electron microscope (SEM, EVO M10-Zeiss). For the determination of the edge radius r_e , which describes the edge between the non-machined workpiece surface and the cavity wall, a 2D holistic approximation was used [Lue12], while the areal surface roughness Sa on the cavity ground was measured in accordance with ISO 25178.

Manufacturing Strategy

A detailed investigation was performed based on the results described in Sect. 4.3.4 in order to identify the influence of the relevant process parameters on the removal quality. With respect to the targeted dimensions, suitable laser and scan parameters were selected (see Table 4.3). Thereby, the cavity manufacture consists of two steps. As the first step, a roughing is applied to achieve the required removal depth.

Table 4.3 Summary of the selected parameters for the laser chemical manufacture of the micro cavities [Mes18]

	$P_L \times \tau_E$ [W]	v_{feed} [$\mu\text{m/s}$]	$d_{overlap}$ [μm]	n_{scan} [–]	$t_{process}$ [min]
LCM roughing	0.6	10	6	2	12.5/50
LCM finishing	0.3	50	6	30	37.5/150

$P_L \times \tau_E$: laser power (after the propagation through the electrolyte), v_{feed} : feed velocity
 $d_{overlap}$: lateral overlapping, n_{scan} : scan repetitions, $t_{process}$: processing time

Table 4.4 List of the symbols used

Symbol	Description	Unit
a	Approximation constant ($a = \pi/(\pi-2)$)	–
A	Control variable	–
A_{theo}	Target shape parameter	–
A_{meas}	Measured shape parameter	–
C_p	Specific heat capacity	kJ/(kg K)
$d_{overlap}$	Lateral overlapping	μm
D	Thermal diffusivity	m^2/s
d_{rem}	Removal depth	μm
d_{spot}	Laser spot diameter	μm
$G(X, Y, Z)$	Green function	–
G	Geometry parameter	–
H	Heat transfer coefficient	$\text{W}/(\text{m}^2 \text{ K})$
i	Production iteration	–
I	Laser power density	W/cm^2
K_p	Gain factor	–
l	Absorption depth	nm
l_{feed}	Feed length	μm
n_{scan}	Number of scan repetitions	–
P_L	Laser power	W
P_{abs}	Absorbed laser power	W
r	Laser beam radius	μm
r_i	Atom radius	10^{-12} m
r_e	Edge radius	μm
R_{rem}	Removal rate	mm^3/min
S_a	Areal arithmetic surface roughness	μm
S	Cross-sectional straightness	–
T	Temperature rise	$^{\circ}\text{C}$
$T_{Boiling}$	Electrolyte boiling temperature	$^{\circ}\text{C}$
$T_{model,peak}$	Peak surface temperature (model)	$^{\circ}\text{C}$
$T_{R,max}$	Upper limit temperature for material removal	$^{\circ}\text{C}$
$T_{R,min}$	Bottom limit temperature for material removal	$^{\circ}\text{C}$
t	Time	s
t_L, t_{inter}	Irradiation time (interaction time)	s
$t_{process}$	Processing time	s
U	Actuating variable	–
v_{feed}	Feed velocity	$\mu\text{m}/\text{s}$
v_{flow}	Electrolyte flow velocity	m/s
v_{rem}	Removal velocity	$\mu\text{m}/\text{s}$
w_{rem}	Removal width	μm
$X \ Y \ Z$	Dimensionless coordinates	–

(continued)

Table 4.4 (continued)

Symbol	Description	Unit
$x\ y\ z$	Dimensional coordinates	m
z_i	Atomic number	–
α	Dimensionless quantity (r/l)	–
α_{abs}	Wavelength-related absorption coefficient of Ti	–
θ	Dimensionless quantity ($H \cdot r/\kappa$)	–
κ	Thermal conductivity	W/(m K)
λ	Laser wavelength	nm
ϕ	Integration variable/ substitution quantity ($\tau \cdot \tau'$)	–
ρ	Density	Kg/m ³
τ	Dimensionless time coordinate	–
τ_E	Transmission coefficient of the electrolyte	–
Ψ	Dimensionless temperature rise	–
Δd_{rem}	Removal difference/tolerance	μm

In the following step, laser chemical finishing is applied to improve the surface quality (Table 4.4).

Manufacturing Results

Figure 4.30 shows examples of the captured SEM images of laser chemically roughened and finished micro cavities with the targeted dimensions of $(300 \times 300 \times 60)\ \mu\text{m}^3$. The measured removal geometries have shown that the

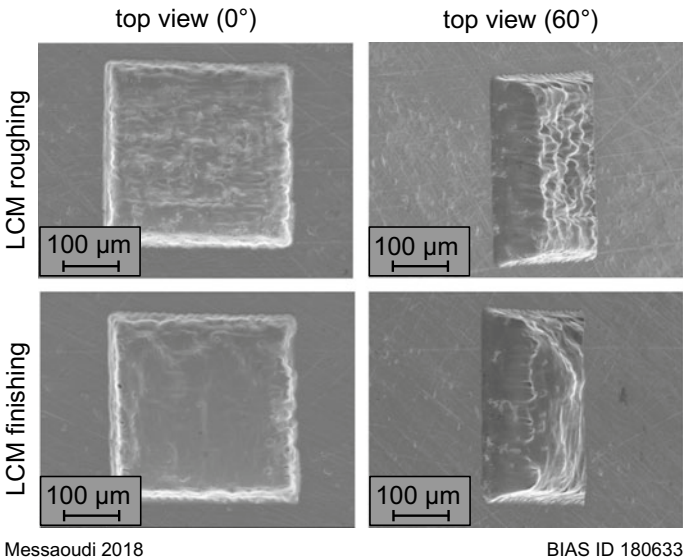


Fig. 4.30 SEM images of the laser chemically manufactured cavities (side length 300 μm), including the two steps roughing and finishing (top views under 0° and 60°)

LCM roughing results in mainly achieving the cavity dimensions, while the LCM finishing provides the final contouring and smoothing of the cavity surface. Indeed, sharp and accurate contours were successfully realized.

The quantitative characterization of the defined quality parameters revealed that the applied LCM strategy ensured the required depth of 60 μm , whereby the removal depth was increased by the LCM finishing step by an additional 10 μm . Moreover, the mean edge radii of the cavities amount to $(10.5 \pm 1.6) \mu\text{m}$ and $(11.2 \pm 1.3) \mu\text{m}$ for roughing and finishing, respectively. Depending on the machining task, an enhanced material removal, which is characterized by a poor surface quality, can be assured with slow scan velocities [Mes18]. Besides, controllable and low removal rates can be realized with increased scan velocities and reduced laser powers [Eck17b]. This combination was applied during the ensuing finishing step and led to an improved surface quality.

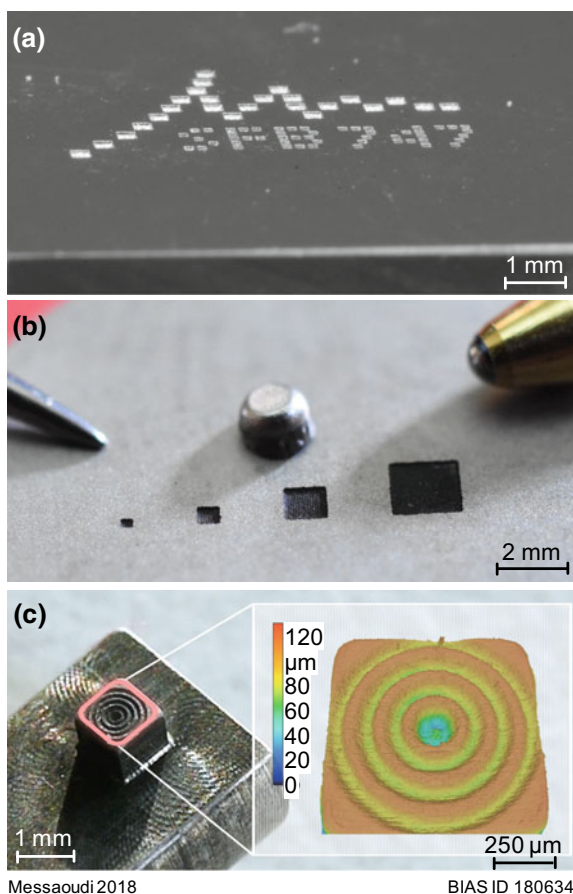
The mean roughness S_a was reduced from $>2 \mu\text{m}$ down to 0.7 μm , while the peak roughness S_z was improved from 45 μm down to 8 μm . Moreover, the analysis of the chemical composition at different regions by energy dispersive X-ray spectroscopy indicates that the roughing step results in a noticeable deposition of metallic salts and oxides, whereas the finishing step results not only in a surface smoothing but also in removing the residues of oxygen and phosphor and thereby in resetting the conditions of the base material [Mes18].

4.3.5.2 Other Examples of Laser Chemically Machined Micro Tools

The square cavities shown in the previous section can be varied in size and replicated with high reproducibility. Figure 4.31a shows the logo of the CRC 747 patterned with the different square cavities in Stellite 21. Besides, hexagonal cavities with side lengths of 250 μm were also manufactured in Stellite 21, as reported in [Mes17b]. Following the aim of high removal rates and cavity depths of $>200 \mu\text{m}$, multiple scans with feed velocities $<20 \mu\text{m/s}$ and relatively high quotient P_L/d_{spot} between 60 and 100 $\text{mW}/\mu\text{m}$ were used. There, the occurrence of electrolyte boiling and related removal disturbances were not considered. The results show that cavity depths up to 450 μm can be achieved, while the edge radius increases with the removal depth up to 30 μm . Moreover, high shape accuracy at the surface is demonstrated with form deviations $<3\%$.

In addition, as demonstrated in Sect. 4.3.4, the machining of non-self-passivating materials such as high-speed steel is possible considering the limited processing time (of some hrs). Based on this, micro cavities were machined in HS10-4-3-10, following the same strategy used to manufacture Stellite 21 [Mes18a]. Figure 4.31b shows square cavities with different side lengths from 150

Fig. 4.31 Examples of LCM fabricated micro forming tools: **a** CRC logo written with square micro dies in Stellite 21, **b** square micro dies in high-speed steel HS10-4-3-10 with different side lengths from 150 μm to 2 mm and **c** micro textured friction tool (stainless steel 1.4310)



to 2 mm. Due to the immediately induced reaction at the metal-electrolyte interface, higher removal rates up to 50 $\mu\text{m/s}$ were achieved. Moreover, similar edge radii of 15 μm on average were measured. However, due to the unequal chemical dissolution rates of the different alloy elements/phases with respect to the electrolyte solution used, an intensified grain boundary attack was observed during the finishing step, which led to an increase of the mean areal roughness S_a from 1.5 μm (after the roughing step) to 2.3 μm .

Among others, LCM was also used to fabricate molding micro tools (1 mm 1 mm) from stainless steel 1.4310, as shown in Fig. 4.31c. As reported in [Rob17], these tools were used for the structuring of monocrystalline diamond by ultrasonic-assisted friction polishing (see Sect. 4.7). Therefore, periodic circular and linear free-standing bridges <100 μm in width and >30 μm in height were realized. Thereby, it was found that the removal with a circular movement increases with a smaller radius and is more intense than with the linear one.

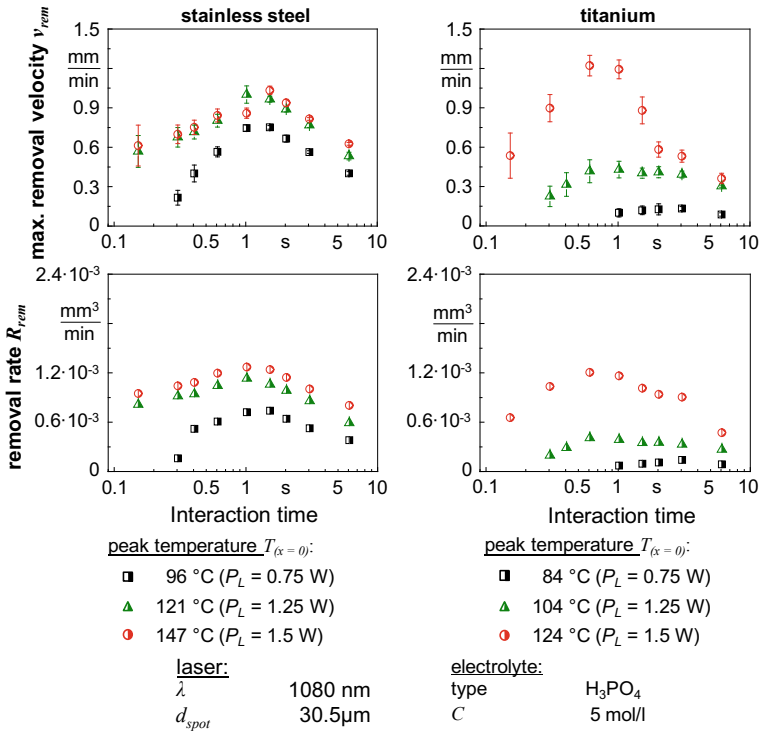
4.3.6 Comparison with Other Micro Machining Processes

Taking electrochemical machining (ECM), electrical discharge machining (EDM) and micro milling as competing methods, the maximum removal velocity and rates were defined as follows:

$$\text{removal velocity } v_{rem,max} = \text{removal depth } d_{rem,max} \cdot \frac{\text{feed velocity } v_{feed}}{\text{spot size } d_{spot}} \quad (4.5)$$

$$\text{removal rate } R_{rem} = \text{removal volume } V_{rem} \cdot \frac{\text{feed velocity } v_{feed}}{\text{feed length } l_{feed}} \quad (4.6)$$

Figure 4.32 shows examples of the maximum removal velocities $v_{rem,max}$ and rates R_{rem} determined within the disturbance-free regime ($T_{(x=0)} < 150^\circ\text{C}$) in titanium and stainless steel (AISI 304) in a 5 molar H_3PO_4 environment. In both



Messaoudi 2018

BIAS ID 181091

Fig. 4.32 Determined maximum removal velocities v_{rem} and removal rates R_{rem} during LCM of stainless steel (AISI 304) and titanium in a 5 molar phosphoric acid solution in dependence on the interaction time under different thermal loads

materials it is observed that the removal velocity/rate increases first with the thermal input and the interaction time and achieve a maximum at interaction times between 0.6 s and 1.5 s. In general, the highest removal is observed around $t_{inter} \approx 1$ s. In combination with a suitable thermal input, which is defined to be achieved with a temperature field having $T_{(x=0)} = 125$ °C, removal velocities up to 1.25 mm/min in titanium and 1 mm/min in stainless steel can be realized. The related removal rates R_{rem} amount to about $1.25 \cdot 10^{-3}$ mm/min in both materials. Similar behavior is observed also in LCM of Stellite 21 [Mes18a], where maximum removal velocities of 0.75 mm/min were obtained at an interaction time $t_{inter} \approx 1.2$ s. In contrast, the LCM of the non-self-passivating alloy HS10-4-3-10 in a 5 mol/l H_3PO_4 electrolyte solution is characterized by a continuous decrease of v_{rem} with increasing interaction time [Mes18a]. In comparison with the self-passivating materials, the removal velocities obtained in HS10-4-3-10 including the background etching amount to 2 mm/min at $t_{inter} \approx 1$ s.

Moreover, these determined LCM removal velocities of some mm/min within the disturbance-free removal regime are comparable to the feed speeds usually applied in the ECM process. Despite the much higher removal rates (some mm³/min), which are related to the size of the electrodes used, the ECM of titanium- and nickel-base for aero engine components is ensured with feed velocities between 0.5 mm/s and 1.5 mm/min, as reported by Klocke et al. [Klo13]. Taking similar interaction zones (some 10^4 μm²), as is the case in micro-ECM, it can be stated that LCM shows higher removal efficiency. Han et al. [Han16] have determined feed velocities of 0.4 to 1 μm/s in micro-ECM of micro rods made of stainless steel (AISI304).

With the same target dimensions, as described in Sect. 4.3.5.1, micro square cavities in Stellite 21 were also manufactured by micro milling using hard coated tungsten carbide ball-end mills with diameters of 0.2 and 0.1 mm. A detailed description of the machining procedure comprising roughing and finishing steps can be found in [Mes18]. The cavities resulting here have undergone the same characterization as the laser chemically machined ones. Comparison of the two processes reveals that laser chemical machining (consisting of roughing and finishing steps) is more suitable for manufacturing cavities with dimensions <200 μm due to the higher shape accuracy with stable mean edge radii of (11.2 ± 1.3) μm, as can be seen in Fig. 4.33. However, the finish quality of micro milling with mean surface roughness Sa of 0.2 μm could not be achieved with laser chemical machining. Due to in-process induced waviness (at spatial wavelengths between 20 μm and 100 μm), the surface quality could only be improved from >2 μm down to 0.7 μm. Further, the metallographic analysis of the near-surface layers reveals that both manufacturing processes ensure gentle machining without any noticeable microstructural impact [Mes18].

In view of the machining time, micro milling appears much more efficient than laser chemical machining, e.g., 5 and 200 min are needed for the machining of one cavity of $(300 \times 300 \times 60)$ μm³ using micro milling and LCM, respectively. However, when considering the tool interaction area ($31.5 \cdot 10^3$ μm² for the 100 μm ball-end mill and $2 \cdot 10^3$ μm² for the laser beam), which is about 16 times larger for

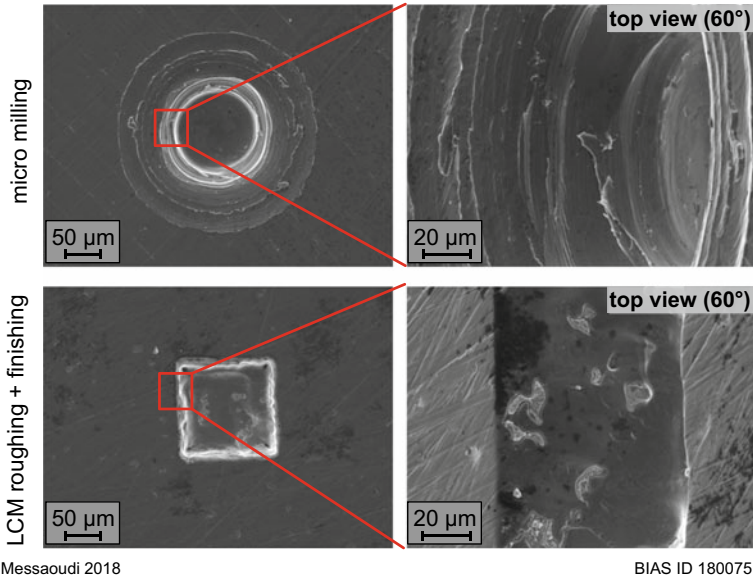


Fig. 4.33 Top view SEM images of a micro milled (above) and laser chemically machined (below) cavity with targeted dimensions of $(150 \times 150 \times 60) \mu\text{m}^3$ as well as under 60° magnified sections showing the cavity wall

micro milling, the LCM removal rates are close to those of micro milling. With regard to the tool area, the average removal rates within the applied machining conditions amount to $2.7 \cdot 10^{-5} \text{ mm}^3/\text{min}$ for LCM and $6.75 \cdot 10^{-5} \text{ mm}^3/\text{min}$ for micro milling.

In general, the presented examples show the diversity and flexibility of laser chemical machining as well as its efficiency, which is comparable to that of well-established processes such as micro milling and ECM.

4.4 Process Behavior in Laser Chemical Machining and Strategies for Industrial Use

Salat Mehrafsun, Hamza Messaoudi* and Frank Vollertsen

Abstract Laser chemical machining (LCM) is a competitive processing method in comparison with electrochemical machining (ECM) and micro milling for the manufacture of micro tools especially with structure dimensions $<200\text{ }\mu\text{m}$. However, the processing window for a disturbance-free removal is limited to only some 100 mW due to the process sensitivity to electrolyte boiling and related hydrodynamic effects. In this section, we focus on the environmental friendliness and the machine handling as two additional key aspects towards a transfer to near-production use. Therefore, alternative sustainable electrolytes, usually used in ECM, such as sodium-based solutions are applied. The resulting removal behavior and rates are compared and discussed with respect to the use of acidic etchants. Furthermore, monitoring concepts that ensure an automatic workpiece alignment and in-process removal control as well as the development of a fast and safe workpiece exchange are presented. Moreover, it is shown that fluid dynamic simulations can be used to improve the design of the chemical cells and to ensure a homogeneous electrolyte flow. The strategies presented enable an automated, user-friendly and safe operation.

Keywords Laser micro machining • Laser chemical machining • Concurrent engineering

4.4.1 Introduction

Electrochemical machining (ECM) processes are gaining in importance in the manufacturing of micro components because they avoid heat-affected zones and thermal stresses compared with conventional machining [Geo03]. To further increase the removal rates as well as the processing quality, the trend toward hybridized ECM is expected to increase [Gup16]. This includes the combination of ECM with other processes such as electro discharge machining (EDM) or laser machining (LM). In the case of laser-assisted ECM, a laser beam of 100 to 300 μm in diameter is coupled in a coaxial arrangement to the electrolyte stream through a nozzle electrode with a diameter of 1 mm [Paj06]. Due to the laser-assistance the removal rates of different metallic materials, such as stainless steel, aluminum, nickel and titanium alloys, have been increased up to 50% in comparison to those obtained with ECM [Sil11a]. Furthermore, Bäuerle has proved that an electrodeless ECM especially of metals within an electrolyte environment can be initiated by laser irradiation [Bae11]. Thereby, the laser-induced temperature field can be generated by a localized thermobattery that allows a current flow within the metallic

surface and can thereby change the electrochemical potential to the range of an anodic material dissolution. Based on this knowledge, laser chemical machining (LCM) was developed especially for the micro machining of metallic surfaces. A similar concept is used by the Fraunhofer Institute for Solar Energy Systems (Fraunhofer ISE) to machine silicon-based photovoltaic elements. There, the laser beam is guided via total refraction onto a liquid jet with a diameter of 30 to 80 μm generated in a nozzle with pressures up to 500 bar. Depending on the electrolyte solution, the laser heating or ablation can be combined with physical-chemical reactions such as etching, doping or deposition [Kra08]. A different method uses wet-chemical-assisted laser ablation, in which semiconductors such as gallium nitride (GaN) are irradiated with a fs-laser in hydrochloric acid (HCl) solution in order to realize micro channels. Nakashima et al. have demonstrated that the processing in a liquid environment results in smooth structures with sizes of some 100 nm [Nak09].

LCM and ECM have quite similar mechanisms of dissolution and surface modification. These processes have the common feature that material removal is based on the chemical dissolution on an atomic scale [Meh16a]. In LCM the material removal is accomplished by the laser-induced chemical reaction between an electrolyte and the metallic surface of the workpiece [Now94] and is mainly dependent on the laser-induced temperature distribution over the workpiece surface [Mes17a]. Besides, the thermophysical properties of the metallic material, the electrolyte characteristics (light absorption, concentration, flow direction and velocity, etc.) as well as the chemical reactivity of both are additional factors that influence the removal quality and rate. The influence of these factors is described in detail in Sect. 4.3. In general, laser chemical machining enables non-contact material processing using low laser power densities compared to the laser ablation process [Meh12]. Depending on the material-electrolyte combination, the material removal can be realized on the one hand by self-passivation or by means of an applied potential, resulting in a thin passivation layer. According to Nernst, the electrochemical potential is proportional to the temperature, and therefore to the laser power applied [Ste10].

In Sect. 4.3 the competitiveness of laser chemical machining (LCM) in comparison with electrochemical machining and micro milling for the manufacture of micro tools was demonstrated, especially for structures with dimensions $<200\text{ }\mu\text{m}$ [Mes18]. Using thermal and closed-loop models, a profound understanding of the LCM removal mechanisms with the aim of avoiding removal disturbances has been developed. This opens up the opportunity for a predictable and controllable removal quality. However, the environmental aspects as well as the machine handling are still key aspects to consider prior to widespread industrial acceptance of the LCM process. For this reason, the use of alternative sustainable electrolytes frequently used in ECM, such as sodium-based solutions, is investigated and compared to the acidic etchants regarding the removal characteristics (width and depth) and quality. Furthermore, automation concepts for workpiece alignment, in-process removal

control as well as fast and safe workpiece exchange are presented. In addition, fluid dynamic simulations are performed with the aim of improving the design of the chemical cells and to ensure a homogeneous electrolyte flow.

4.4.2 Materials and Methods

For the experimental investigations, self-passivating and technologically relevant (in the aerospace industry and medical technology) metallic materials, e.g. titanium (3.7024), stainless steel (1.4310), cobalt-chrome alloy Stellite 21 and the tool steel X100CrMoV8-2 (in hardened and tempered condition) were machined in different electrolyte solutions. Thereby, the passivation layers prevent corrosion or chemical dissolution of the material in direct contact with the electrolyte and enable the investigation of the laser-induced chemical reaction behavior without additional external currents. For greater environmental friendliness, the LCM process was performed in aqueous solutions usually used in electrochemical machining, such as sodium nitrate, sodium chloride and citric acid. For comparison, removal investigations were also done in phosphoric and sulfuric acid solutions. Table 4.5 provides an overview of the applied electrolytes and their concentrations.

The laser chemical machining was carried out in electrolyte-jet based (JLCM) and scanner-based (SLCM) LCM machines, which are described in detail in Sect. 4.3. To analyze the removal geometry, including width, depth and volume, laser scanning confocal microscopy (Keyence VK-9710) as well as a light microscopy (Keyence VHX-1000) were used. In addition, scanning electron microscopy (SEM) and energy dispersive X-ray spectroscopy (EDX) were used to analyze the chemical composition of the machined cavities.

4.4.3 Sustainable Electrolytes for LCM

The JLCM system (see Sect. 4.3.2) was used in machining titanium and Stellite 21 in different electrolytes [Hau15]. Thereby, it was found that titanium exhibits up to 30% deeper cavities and up to 40% higher removal rates than Stellite 21 when machining both in a 5 molar phosphoric acid solution. In addition, citric acid

Table 4.5 Overview of the materials and electrolytes used for the experimental work

Electrolyte	Concentration [mol/l]
Phosphoric acid (H_3PO_4)	2.5/5/7.5
Sulfuric acid (H_2SO_4)	1.9
Citric acid ($\text{C}_6\text{H}_8\text{O}_7$)	5
Sodium chloride (NaCl)	2/5
Sodium nitrate (NaNO_3)	2/5

(1 M $C_6H_8O_7$) was identified as a suitable environmentally friendly electrolyte, especially for the machining of the tool steel X110CrMoV8-2. However, the resulting etching reaction is significantly limited, which can be explained by the limited dissociation of citric acid within water and thereby by the lower number of reactants that can be provided for the chemical reaction. Compared to the LCM removal in phosphoric acid [Ste09b], the resulting cavity depths were about 80% lower [Hau15].

Using the SLCM setup (see Sect. 4.3.2), the threshold power required for laser-induced material removal was determined for different electrolyte-workpiece combinations. Phosphoric acid and sodium nitrate solution with concentrations of 5 mol/l as well as sodium chloride solution having a concentration of 2 mol/l were used as electrolyte environments during the machining of titanium (3.7024). Thereby, the resulting cavities were analyzed with respect to their removal volume V_{rem} after a constant irradiation time of 1 s and a gradual increase of laser power P_L . Depending on the electrolyte, the material removal starts at different laser powers, as can be seen in Fig. 4.34.

Using phosphoric acid, material removal is observed at threshold laser powers of 0.7 W. In contrast, material removal in sodium nitrate and sodium chloride solutions takes place at higher laser powers of 1 W and 1.7 W, respectively. To differentiate between the chemically driven and the thermally driven effects, the interaction between the titanium surface and laser irradiation was investigated additionally under an argon atmosphere. As mentioned in Sect. 4.3, the cooling effect of the liquid in LCM is rather low and can be neglected, making this comparison valid. In Fig. 4.34 it is shown that the first material removal, which is

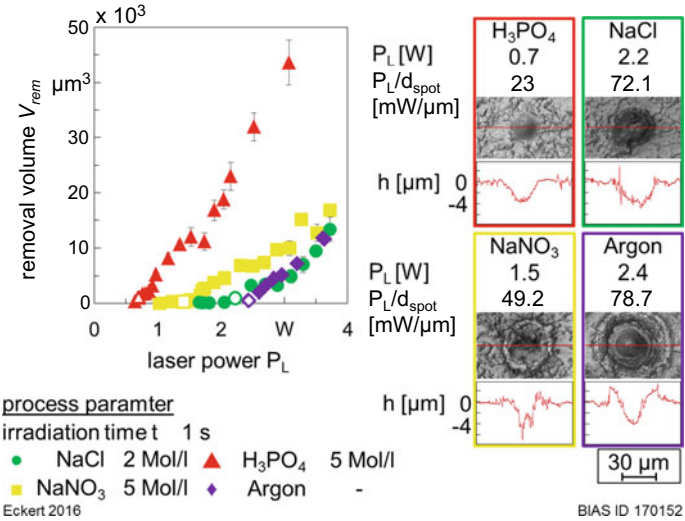


Fig. 4.34 Removal volume V_{rem} in titanium in dependence on the laser power and electrolyte processed with SLCM

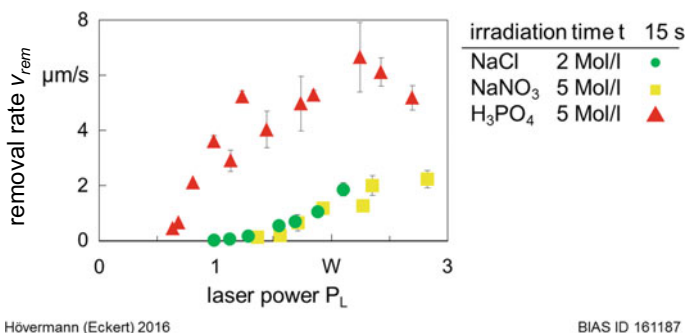


Fig. 4.35 Removal velocity v_{rem} in titanium in dependence to the laser power and electrolyte processed with SLCM

related to molten titanium, starts at laser powers of about 2.4 W. This removal is mainly the result of melt pool dynamics that throw out molten material from the center to the outer sides and is governed by temperatures that exceed the melting point of titanium ($>1668\text{ }^{\circ}\text{C}$). This can be explained by a sudden jump in the absorption coefficient by temperatures $>800\text{ }^{\circ}\text{C}$ from 40% to $>70\%$ [Kwo12].

Figure 4.35 shows the resulting removal velocities v_{rem} in titanium in dependence on the electrolyte used. In the phosphoric acid environment, the removal velocity v_{rem} increases linearly between laser powers of 0.7 W and 1 W up to values of $4\text{ }\mu\text{m/s}$. For $P_L > 1\text{ W}$, the removal rate decreases first before it continues to increase again with the laser power, with rising standard deviations showing a non-homogeneous removal. This is in accordance with the correlated surface temperatures (see Sect. 4.3.4) showing the first disturbances within the transition boiling regime (T between 104 and $140\text{ }^{\circ}\text{C}$) [Mes17a]. For the case of sodium nitrate and sodium chloride solutions, the removal rates indicate a similar behavior. At $P_L = 1\text{ W}$, etching rates $<0.1\text{ }\mu\text{m/s}$ have been determined. These reach their maximum at P_L of 2.1 W , showing values of about $2\text{ }\mu\text{m/s}$. These removal rates are significantly lower in comparison to those obtained in phosphoric acid. Thus, a higher irradiation time is required for an equally deep removal. With respect to the surface temperature, it becomes clear that the removal occurs first after the electrolyte boiling, which indicates the involvement of gas bubbles in the etching process.

A closer look at the SEM records of the resulting cavities in titanium (compare Figs. 4.36 and 4.37) shows the differences of the removal quality depending on the electrolyte used.

The removal of titanium in sodium nitrate NaNO_3 (Fig. 4.36, left) and sodium chloride NaCl (Fig. 4.36, right) is labeled by a pronounced intergranular corrosion, as already described by Wendler et al. [Wen12]. In accordance to [Uen08], the removal is assumed to comprise intergranular penetration and grain dropping occurring by turns. In contrast, the laser-induced chemical removal using acidic aqueous solution, e.g. phosphoric acid (H_3PO_4), results in much smoother surfaces

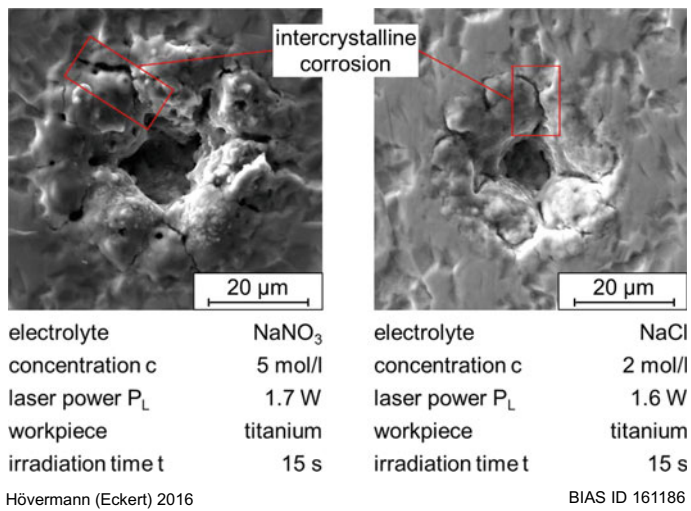


Fig. 4.36 Removal cavities in titanium processed with SLCM and (left) NaNO₃ and (right) NaCl as electrolyte

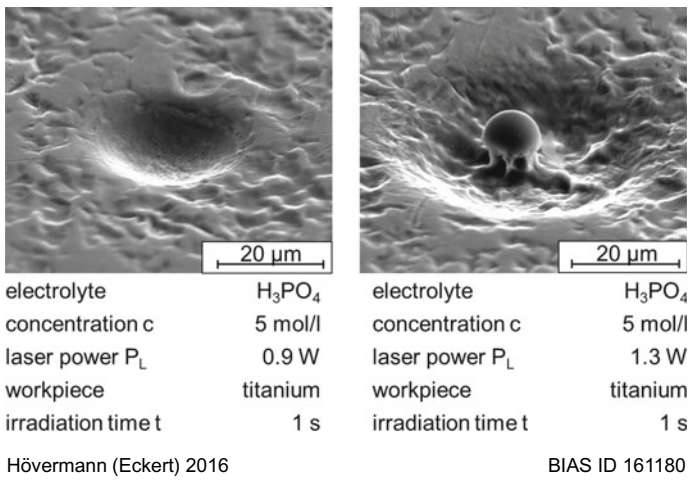


Fig. 4.37 Removal cavities in titanium processed with SLCM and H₃PO₄ as electrolyte

without any significant intergranular corrosion effects (Fig. 4.37, left). However, the resulting cavity geometry depends on the processing parameters used. At higher laser powers, removal disturbances can take place in the cavity center (Fig. 4.37, right). The analysis of their chemical composition using energy dispersive X-ray spectroscopy revealed that within the disturbance-free removal only K_α and K_β titanium peaks can be detected, while the mushroom-like pile that fills the center of

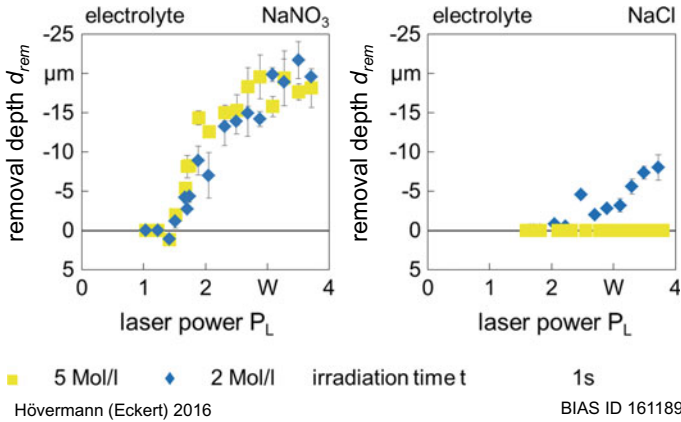


Fig. 4.38 Removal depth d_{rem} in titanium in dependence on the electrolyte and its concentration processed with SLCM

the disturbed cavities (Fig. 4.37, right) is additionally characterized by significant phosphor and oxygen peaks [Eck17a]. As reported by Gutfeld et al. [Gut86] and Nowak et al. [Now96], an etching in the periphery while plating in the laser beam center and vice versa can take place in dependence on the metal-electrolyte combination as well as on the laser and electrolyte parameters. Which process is dominant depends on the temperature gradient as well as on the type and concentration of the dissolved reaction products.

Figure 4.38 shows the influence of the electrolyte concentration on the resulting removal depth in titanium using NaCl and NaNO₃ solutions. Thereby, it can be clearly determined that material removal using NaCl is only possible with a concentration of 2 mol/l. This can be traced back to the enhanced salt crystallization due to local solution boiling at high concentration. Hence, this salt film formed on the surface can slow down or prevent the material dissolution at the workpiece surface [Dat87]. In comparison, similar removal depths are measured in NaNO₃ for the concentrations of 2 mol/l and 5 mol/l, which reveal no significant influence of the concentration for this etchant.

4.4.4 Strategies for Industrial Use of LCM

4.4.4.1 Automatic Workpiece Alignment for JLCM

For a further increase in the process stability and reproducibility of the LCM processing different strategies are pursued. One of these strategies is to increase the degree of automation with the aim of enabling more flexible and faster processing. Investigations have shown that the quality of laser chemical machined micro tools

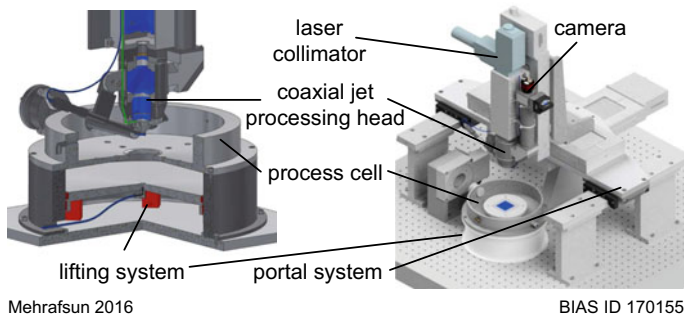


Fig. 4.39 JLCM system with integrated image processing for automatic workpiece alignment

is highly dependent on the positioning and alignment of the semi-finished products in the processing room (chemical cell). A first approach to improve the reproducibility is to implement automatic workpiece positioning using image processing. Therefore, the position of the workpiece within the processing cell is detected by means of reference points and compared with the predetermined position of the CAD data and the path planning algorithm. The system determines the positioning error by using image processing techniques and permits automatic alignment of the ideal starting and workpiece position with an accuracy of $<1 \mu\text{m}$ with respect to the laser focal position. Thus, reproducible starting conditions for laser chemical machining can be ensured. This results in fewer parameter adjustments during processing and contributes to a reduced processing time. Figure 4.39 shows the design of the JLCM system with automatic workpiece alignment.

4.4.4.2 In-Process Monitoring and Fast Workpiece Exchange for SLCM

To provide a constant manufacturing quality, it is necessary to monitor and control all relevant process parameters, such as the pressure, workpiece potential, laser power and electrolyte flow rate. Otherwise, changes of these parameters over time could affect the machining behavior and result in losses in quality (see Fig. 4.40). Several factors limit the economic efficiency of the process. The conventional removal rates enable the use of only low process speeds (some $\mu\text{m/s}$), which means long processing times. Furthermore, as sample changing is performed manually, both the machining precision and speed are affected. To avoid this related downtime and to ensure user-friendly and safe operation, the system design must be trouble-free and low-maintenance. The development of an industry-compatible process cell was carried out in accordance with VDI 2221.

This cell, as depicted in Fig. 4.41, is based on a pneumatic locking system in combination with a modular workpiece holder that allows safe workpiece exchange with minimum contact with the electrolyte within a maximum of 30 s. Using a

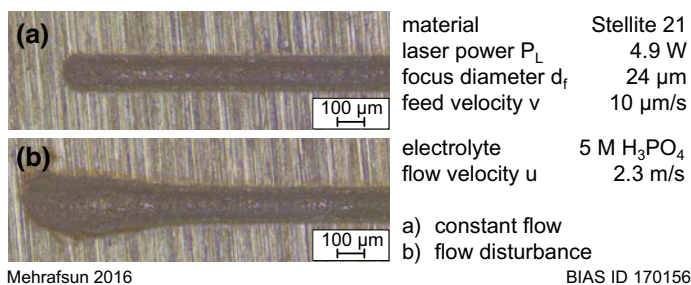


Fig. 4.40 Example of LCM removal path in Stellite 21 processed with phosphoric acid (5 mol/l) **a** without and **b** with disturbance in electrolyte flow velocity

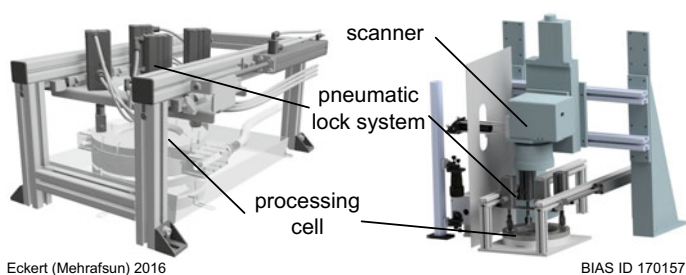


Fig. 4.41 SLCM system with pneumatic lock system for fast workpiece exchange

safety valve in the fluid circuit and locking units in the closure system, the process cell is protected from over-pressure and leakage of electrolyte during processing.

4.4.4.3 Demand-Oriented Multi-channel Flow in SLCM

As mentioned before, trouble-free and high-quality processing as well as reduced process times are essential for industrial implementation of LCM. Moreover, the removal rates must be enhanced to ensure that the machining is competitive. However, the increase of reaction rates is mainly accompanied by an increased formation of hydrogen [Meh13]. In addition, it necessitates the use of higher laser powers that can induce high surface temperatures and result in electrolyte boiling [Sil11a]. As a result, undesirable gas bubble formation and thereby removal disturbances can occur [Meh13].

Another source of disturbance could be the high saturation of the electrolyte during the LCM procedure. For industrial use of LCM, these factors should be taken into account, as well as the electrolyte flow behavior. Investigations have shown that the geometry of the process cell could affect the flow behavior, induces turbulence and gas bubbles, and results in a reduced processing quality (see

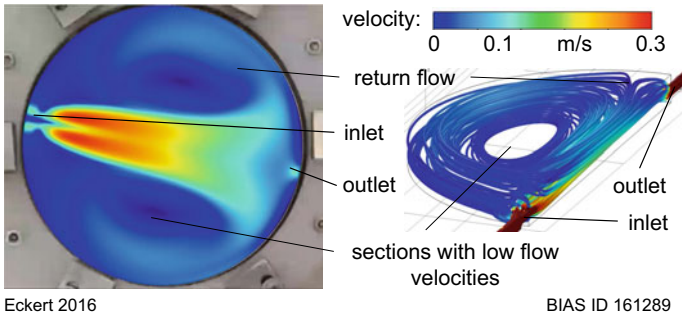


Fig. 4.42 Numerical fluid dynamic simulation of electrolyte flow within the process cell (half of the cell) before optimization

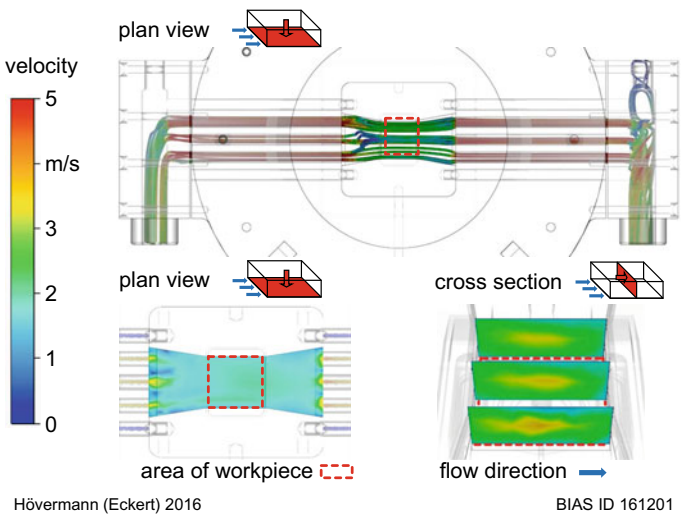


Fig. 4.43 Numerical fluid dynamic simulation of electrolyte flow within the process cell, (plan view above) electrolyte flow from inlet to outlet, (plan view below) flow distribution on workpiece surface, (cross-section) three cross-sections of flow distribution on workpiece surface

Fig. 4.42). Considering these factors, numerical fluid dynamic simulations (CFD) were performed to define a suitable cell geometry and electrolyte flow behavior.

The CFD simulation results are shown in Fig. 4.43. As can be clearly seen, the newly developed fluid system is able to ensure a constant and homogeneous stream profile at a flow velocity of 2.5 m/s. These flow conditions can guarantee a constant electrolyte exchange and continuous transportation of the gas bubbles that emerge,

and thereby a stable machining operation. Further, it is possible to reduce or expand the interior of the process cell depending on the workpiece size using inserts, as well as to set the electrolyte flow velocity by switching on or off the inlet and outlet channels with respect to the pump setting parameters.

4.5 Flexible Manufacture of Tribologically Optimized Forming Tools

Oltmann Riemer*, **Peter Maaß**, **Florian Böhmermann**, **Iwona Piotrowska-Kurczewski** and **Phil Gralla**

Abstract In this work, mathematical and engineering methods are applied in union for the manufacture of efficient micro-forming dies exhibiting tribologically active, textured surfaces by micro-milling. This comprises the extension of analytical process models to wear characteristics of milling tool for die making and micro-tribological investigations. These models allow us to derive optimized process parameters for the manufacturing process of tribologically optimized micro-forming dies by using the non-linear inverse problems method. These optimized forming dies exhibit micro-textured surfaces and have a distinct impact on the micro-contact conditions between the die and the work piece, and thus leads to a reduction in dry friction during the actual forming process.

Keywords Surface • Cutting • Optimization

4.5.1 Introduction

Metal cutting is one of the most widely used methods to produce the final shape of manufactured products in macro dimensions [Alt00]. Therefore, its application for micro-parts is a logical step. However, due to size effects in the micro-regime, new challenges arise and need to be addressed for a successful application [Vol10]. Serendipitously, size effects in metal cutting can also offer new opportunities. The inconsistencies in material removal when undershooting the minimum uncut chip thickness in micro-milling leads to the generation of regular micro-textures. These micro-textured surfaces have been shown to reduce friction in dry tribological contact, which can be explained by changes in the micro-contact conditions determining the predominant friction mechanisms. The transfer of micro-textured surfaces generated by micro-milling is seen to be one key steps towards the development of robust dry deep drawing processes. The concept of micro-forming dies exhibiting textured surfaces (e.g. generated by micro-milling) can be seen in Fig. 4.44. However, identifying the most suitable textures offering minimum dry friction and finding the associated process parameter for their generation in micro-milling is not trivial.

Process modeling can help to overcome these issues. In this work, a process model based on sweep volumes incorporating the continuous change from chipping to plowing is presented. This addresses the unique mixture of material removal mechanisms that allow for the manufacture of regular surface textures in hardened tool steel where the texture's design is first of all determined by the process

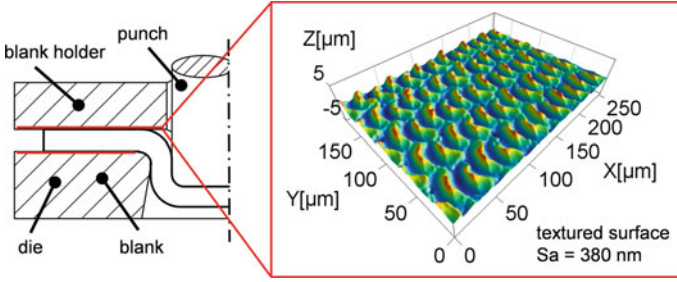


Fig. 4.44 Dry friction in a mold used for micro-cold forming

parameters feed per tooth and line pitch. Suitable process parameters for the manufacture of desired textured surfaces are identified by means of inverse simulation, while taking into concern inverse problems. Classic inverse problems identify the source of observed data. For example, in a computed tomography scan an image is reconstructed from a sinogram, which is the measured density via x-rays over multiple angles. One way to solve such an inverse problem is to use Phillips-Tikhonov-Regularization by minimizing a Tikhonov functional:

$$T_{\alpha,\delta}^{p,q}(u) := \frac{1}{p} \|F(u) - v^\delta\|_Y^p + \alpha \frac{1}{q} \mathcal{R}_q(u) \quad (4.7)$$

where F represents a forward model, u the parameter, v^δ a perturbed data, α the regularization parameter and \mathcal{R}_q the regularization. Most current research deals with numerical implementation [Mor11] and aims to find suitable regularization [Jin12]. In the presented work, the discrepancy term is altered to account for tolerances in the data. The necessary forward model is a combination of analytical and statistical methods. In addition, special attention is paid to the wear of the cutting tool and its influence on the cutting process and machining results. The challenge in this work was to incorporate the size effects in micro-milling, namely the continuous change in material removal mechanism from chip removal towards micro-plowing in dependence on the cutting depth.

The second part of the presented method deals with analytical contact and friction modeling, taking into concern meaningful parameters derived from ISO 25178 are seen to be the key to more precise derivation of input values for inverse process simulation. This represents the basis for the predictive machining of functionalized forming dies with locally adapted tribological characteristics by process parameter manipulation utilizing the previously presented process model. The work flow of the presented methodology is depicted in Fig. 4.45.

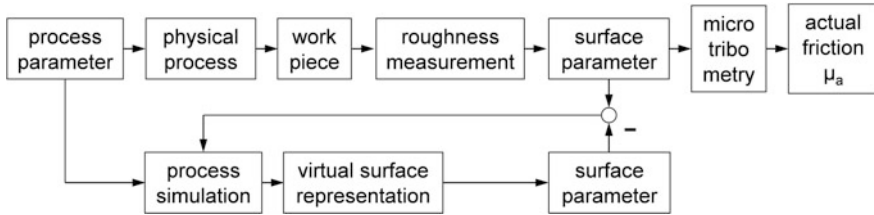


Fig. 4.45 Work flow of computational engineering for micro-milling

4.5.2 Variation, Dispersion, and Tolerance in Inverse Problems

Classical Tikhonov functionals (4.7) consist of two terms, a discrepancy and a regularization term. By minimizing both terms, weighted with a coefficient α on the regularization term, a suitable approximation of the true parameter is found; that is, the parameter that causes the given or observed data. Let V be the space in which the process model F maps onto and all data resides. The discrepancy term then describes the distance of given or observed noised data v^δ to the predicted data $F(u)$ for the parameter $u \in U$. The regularization term $\mathcal{R}_q(u)$ uses some a priori information and maps the parameter u onto the positive real numbers. A common choice for \mathcal{R}_q is (4.8) based on an L^q distance, where u_0 is often set to 0. For prediction models, this is changed to $u_0 \neq 0$ and instead a density point of known data is used to avoid extrapolation in prediction.

$$\mathcal{R}_q(u) := \|u - u_0\|_q^q, \quad 1 \leq q \leq 2 \quad (4.8)$$

In this work, process models are not only restricted to value estimation of the outcome but can also provide a variance or dispersion, as was applied in Sect. 1.4.2. Furthermore, the given data can include a variance, such as through multiple measurements. Both cases are addressed by allowing the provided data to not be a single measurements but instead be a closed set of feasible data points. This set will be denoted as the tolerance area of the point v^δ . To compare two sets while maintaining good numerical properties, the distance measurement given in (4.9) is used. This distance is continuous and measures the overlapping area; that is, it is only equal to zero if S_1 is a subset of S_2 . This is important to ensure that the determined parameter is within the tolerance area if this parameter exists.

$$d(S_1, S_2) = \int_{S_1} \min_{y \in S_2} \|x - y\| dx \quad (4.9)$$

In the following, $S_{F(u)}$ denotes the tolerance set of $F(u)$. The tolerance set of v^δ will be denoted by S_{v^δ} .

For quality management, the three sigma area is a common choice to define a process quality if an additive normal error is assumed [Whe92, Cas12]. To perform the parameter identification, the functional (4.10) is minimized. The minimizer of (4.10) is then the identified parameter.

$$T_{\alpha,\delta}^{p,q}(u) = d_p(S_{F(u)}, S_\delta) + \alpha \mathcal{R}_q(u) \quad (4.10)$$

The minimization of (4.10) is done numerically using a standard non-linear solver, such as gradient descent with adaptive step size, inner point algorithm or sequentially quadratic problem solver. Depending on the properties of F , the solver may need to be adapted to be able to minimize the functional [Boy04, Ber99]. In all cases, only a local minimum is identified, which may not be global minimum because all algorithms are of iterative nature and depend on the starting value. Different strategies, such as hill climbing and trust region, can be used to soften the dependency on the starting value but they have a higher numerical cost.

4.5.3 Computational Engineering

Computational engineering is applied to further comprehend and adjust the micro-milling process. Computational engineering deals with the development and application of computational models and simulations to solve complex physical problems arising in engineering analysis. An example of computational engineering for turning processes can be found in [Bra12].

In this present work, a mathematical model of the cutting process was designed and analyzed. This model is based on physical properties and observed measurements. It combines analytical and data based approaches to ensure that it is accurate and manageable at the same time. The obtained model allows us to simulate the cutting process and predict the outcome of the process for different process parameters and setups. In addition to prediction, it can also be used to find ideal process parameters for a predefined output via parameter identification using methods from inverse problems. This parameter identification can be used to find the cause for an observed data, such as the current wear on the cutting tool.

4.5.3.1 Process Model with Wear on Cutting Tool

The process model in this work is based on sweep volumes to map process parameters, including tool path, feed velocity v_f and cutting tool geometry, onto a finished surface. It is not a finite element or volume method and it differs from these approaches. Its main components are models of the work piece, tool and the tool path. The tool moves along its tool path and a sweep volume is generated. This sweep volume and a model of the workpiece are used to calculate the material

removal process and change of the workpiece itself. While this method can be applied in the macro scale (see the Chapter *Predictive compensation measures for the prevention of shape deviations of micro-milled dental products* for one example), it is extended to reproduce size effects in micro-scale. These size effects are the occurrence of plowing when undershooting the minimum uncut chip thickness, as well as a considerably increased cutting tool deflection. More detail into the model generation [Pio11], validation, and simulation process is given in [Veh15b, Veh17a]. The process model focuses on the finishing step of micro-milling where the last layer of material is removed. This can be applied to all stages of micro-milling. Since size effects are most influential in the last finishing step, a macro model can be used for earlier stages to reduce computational effort and reduce computation times.

The cutting tools used in milling process are also affected by the process. The wear of the tools alters the characteristics of produced surfaces. For micro-milling the shape of the cutter highly influences the surface quality. Progressive tool wear ultimately leads to a decrease in the quality of the work result. Once product specifications (which are the geometrical accuracy and the roughnesses of work pieces) can no longer be obtained, the milling tool will be replaced to provide the desired work result.

In this section, a process model for micro-milling is outlined and the modeling of wear on the tool is explained. Further detail on how to find parameters with respect to wear are given, including how it can be integrated into the theory of inverse problems.

Process Model

The micro-milling process is modeled in three consecutive steps. The first step is the implementation of the process kinematics. The kinematic of a milling cutter is described by a composition of the rotational and translational motion of the tool. This composition describes how the tool is rotating around itself and moving along a given tool path. To account for dynamical changes occurring during the process, a dynamical force model is applied. This is accomplished with a system of ordinary differential equations. The model is presented in details in [Pio11]. Moreover, it is assumed, that the reader is familiar with kinematics of the micro-milling process. If otherwise, refer for example to [Alt06].

To obtain the surface, additional information is needed, such as the shape of the cutting tool, material and size of the workpiece and the material to be machined. Additionally, the material removal mechanism has to be included. For ball-end micro-scale machined surfaces, the minimum chip thickness has to be considered. This means that the chip formation is divided into three parts, see [Veh15b]. Below a certain minimum cutting depth, material is elastically deformed and thus no material is removed; that is, no chip is formed. Above a certain cutting depth, material is completely removed and the chip thickness is equal to the cutting depth. The third stage describes the transition between the former two stages. A visualization of the three different stages and its model are given in Fig. 4.46 according to [Veh15b]. Because the cutting depth is different at all points of the

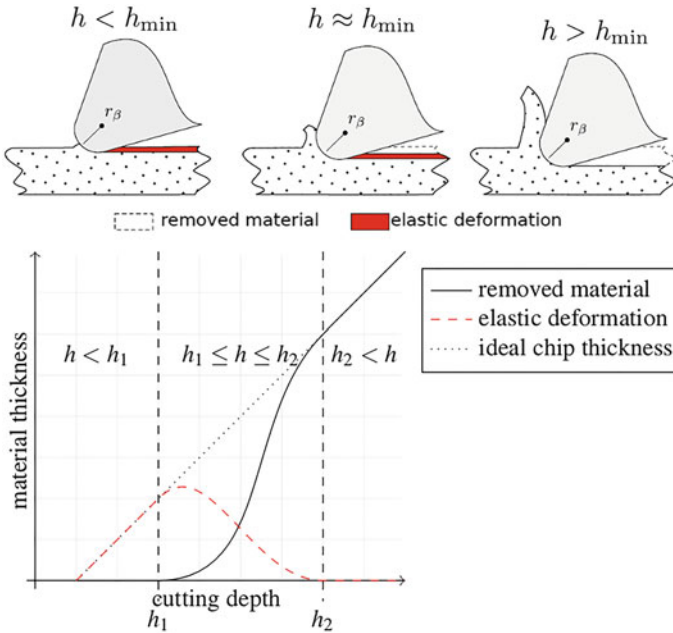


Fig. 4.46 Three stages of the micro-cutting process according to [Ara09], and visualization of the function for the implementation of the chip removal in dependence on the cutting depth into the process model

milling tool and only cutting depth smaller than the tool radius are used for the last milling step, all three stages are constantly present. This results in micro-structures on the produced surface, depending on the process parameters.

The forward model generates a detailed map of the generated surface. Thus, it can be used to compare characteristics of surfaces from different input parameters. To allow a comparison of different surfaces and their tribological characteristics a characterization of the surface is needed.

One way to compare surfaces is to divide deviations into six categories, as defined by DIN: 760:1982-06 from the Deutsche Institut für Normierung (DIN Standards). Deviations of the third and fourth categories describing the roughness of a surface are of special interest. This is further specified in DIN EN ISO 4287, where the so-called one-dimensional characteristics are defined. These include peak-to-valley value, median roughness, average roughness and more. These values are only statistical height parameters, whose calculation is based on every data point. Those parameters that do not include any information about the number of peaks, distribution of peaks and so on, are not sufficient for the application in this work.

For a more precise classification, the Abbott-Firestone-Curve or bearing area curve can be used; some alternative procedures are introduced later in this chapter. The Abbott-Firestone-Curve describes the ratio of the surface at a given height and allows to compare surfaces and their properties. From a mathematical perspective, it

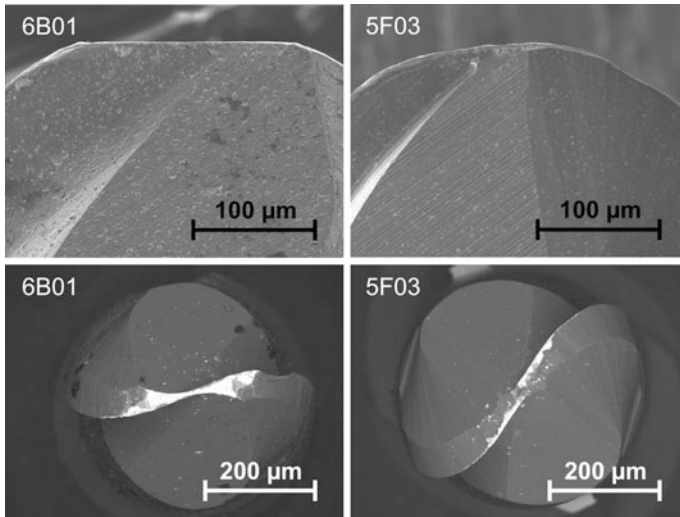


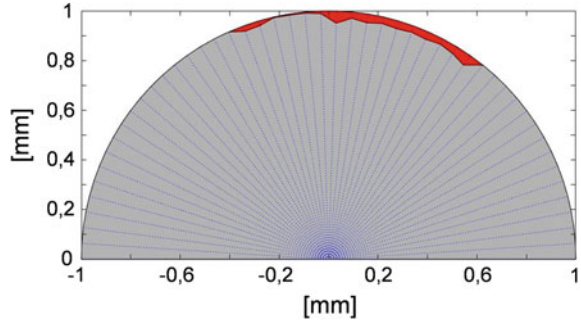
Fig. 4.47 SEM images of a cutting tool as an example of the wear on a ball-end tool

is a cumulative probability density function of the surface's profile height. For the rest of this chapter, it is assumed that all of the data are provided as bearing area curves.

During the manufacturing process, the cutting tool wears out. This results in a change of the cutting tool shape, as depicted in Fig. 4.47. The figure shows a ball-end cutting tool after use. Without wear, the front view would show a circle segment. In the top view (bottom two pictures) the white spots mark the wear. Due to the forces acting on the cutting tool during the manufacturing process, it starts to flatten out. A simple way to model this behavior is to flatten the tool shape over the time. A more accurate way is to consider the actual forces in each point and then model the material removal and deformation of the cutting tool. Two models for the wear over time are included. The first model uses a predefined wear depending on the time. The second model simulates the wear depending on the force applied on the cutting edges. The programming of the first model is less elaborate and it substantially reduces simulation time, whereas the second model is more accurate. To understand how wear of the cutting tool influences the process itself, use of the second model is advised. For ideal parameter identification and adjustment of process parameters during manufacturing, use of the first model is advised.

To identify the wear and exact shape of a cutting tool from a surface measurement, a parameter identification can be performed. This parameter-identification does not depend on the chosen model for wear on the cutting tool because no change in the wear is assumed. For measurements over a long time interval, separate parameter identifications for different points in time are done. The cutting tool in the model is described in polar coordinates and discretized over the radius to allow a

Fig. 4.48 Profile of a simulation of nonuniform wear on a ball-end tool



equidistant discretization on the cutting edge (see Fig. 4.48 for a nonuniform wear on a ball-end tool).

The mathematical operator is extended with the model of wear on the cutting tool and takes an additional input t . This additional input defines how long the cutting tool has been used prior and thus provides the wear on the tool at the beginning of the simulated process. The exact shape of the tool at the time t can also be mapped. In the following two sections, a simple wear model is applied incorporating the flattening of the cutting tool over time.

Minimize Deviation Over a Fixed Time Interval

For a fixed time-interval, $t \in [0, c]$, the overall deviation from the desired tolerance ε can be calculated via

$$\int_0^c \|F(p, t) - g^\delta\|_{L_2(\Omega), \varepsilon} dt,$$

where F is the process model, p process parameters, t the time the cutting tool is used; that is, the degree of wear on the tool, and g^δ the desired or measured surface as Abbott-Firestone-curve. This term measures how much the output will deviate over the whole time interval but does not hold any information at which point in time the output will not lie within the given tolerance. Therefore, a soft boundary is considered in the sense that a local minimum unequal to zero might have no point in time for the condition

$$\|F(p, t) - g^\delta\|_{L_2(\Omega), \varepsilon} = 0$$

The benefits of minimizing deviation over a fixed time interval is that it can be directly applied as a discrepancy term in the Tikhonov functional (4.7) and that the integral can be approximated via known rules, such as the Simpson rule.

Maximizing Machining Time Within Tolerance

To actually maximize the timespan in which a cutting tool can be used with the same parameter set before it needs to be replaced or new process parameters need to

be determined, the ending time of the time-interval has to be flexible. The ending time c is then calculated through

$$c = \arg \max \left\{ c \mid \int_0^c \|F(p, t) - g^\delta\|_{L_2(\Omega), \varepsilon} dt = 0 \right\}.$$

In the case that there is no $c \geq 0$ that fulfills the condition, $c = 0$ will be set. This provides the maximum time before the simulated output is outside the desired tolerance for the first time. As long as the parameter does have a discrepancy greater than zero in the initial case without wear (i.e. $t = 0$), the maximum stays zero. Thus, the argmax cannot be used to replace the discrepancy term in (4.7), as was the case for fixed time-interval, because parameter sets that minimize only the penalty term might be favored over terms that minimize discrepancy and penalty term.

This results in a min-max problem where the discrepancy and penalty have to be minimized while the time interval has to be maximized. While being more accurate for the application, this approach also yields higher computational effort due to finding the argmax for each functional evaluation.

4.5.3.2 Numerical Implementation

The necessary minimization and maximization are done numerically. Numerical methods are often used for parameter identification, especially for complex models. Various methods exist and can be used depending on the properties of the mathematical operator representing the model. An overview on existing methods can be found in [Boy14].

The operator F in this work is non-linear and thus iterative methods have to be applied. In each iteration, the Tikhonov functional and the maximum time-interval length has to be evaluated. In addition, the evaluation of the operator F is computationally expensive.

One solution for these problems is to apply a two term strategy to solve the min-max problem. First, the Tikhonov functional with incorporated tolerances is minimized to find a starting point for the min-max problem within the given tolerance. Using this starting point, the min-max problem is solved by maximizing the time interval and minimizing the penalty term to keep regularization. The former discrepancy term is now used as a non-linear boundary condition on the feasible set. This ensures that all requirements of the inverse problem are still fulfilled while optimizing the process parameter further. It also reduces the number of evaluation of the maximum time-interval length and thus reduces computational effort.

For each of the two steps, a different solver can be applied. To solve the initial inverse problem, the REGINN algorithm with a conjugate gradient method is used [Lech09]. This algorithm linearizes the operator and uses the conjugate gradient algorithm to solve the linear problem. A new iteration is then started with the found solution as the point where the operator is linearized.

If the algorithm is able to find a parameter set that produces a simulated surface with the given tolerance to the provided data, then the non-linear optimization for maximizing the end-time as described in Sect. 4.5.3.1 is performed. However, this step cannot be solved by using the REGINN algorithm because the full min-max problem does not fulfill all requirements and a gradient method is used instead. This method is slower but has fewer conditions on the mathematical operator, which allows the application.

Overall, the two step approach reduces the amount of performed operator evaluation by utilizing a fast converging algorithm to solve the non-linear inverse problems without wear on the tool, which then provides a good start estimation for the more complex min-max problem at hand.

4.5.4 Tribologically Active Textured Surfaces

Metal forming processes are generally subject to friction. Friction (e.g., in micro-deep drawing) predetermines process feasibility, work piece quality, or the achievable drawing ratio β_0 [Nie18]. In the micro-regime, friction becomes even more crucial to forming processes because of the size effects associated with a relative increase of adhesive forces [Vol10]. Friction in forming processes is a result to the effectiveness of lubrication, surface chemistry, velocity of relative motion between die and work piece, temperature, the dies' macro geometry, and fundamental friction mechanisms. These friction mechanisms are the adhesion, the plastic deformation [Bhu04], plowing (two- and three-body) [Suh87], and elastic hysteresis [Czi10]. The predominance of each of the mechanisms is directly determined by the contact state of the interfacing surfaces on microscopic level. The contact conditions are a function of the applied forces, the material properties, and the microscopic surface geometry. Friction control in forming processes usually involves lubrication, surface chemistry manipulation, and the adaption of the die's macro and micro-geometry. With regard to the development of dry forming processes, texturing of forming die's surfaces has become a major topic in research.

The following sections deal with the generation of textured surfaces using micro-milling, methodologies for function orientated surface characterization, and approaches for the selection of most suitable surface textures to achieve minimum friction in dry micro-deep drawing processes.

4.5.4.1 Micro-Milling to Generate Textured Surfaces

Micro-milling is subject to plowing because the uncut chip thickness becomes the same order of magnitude as the cutting edge radius r_β , resulting in a larger proportion work piece material to be elastically and plastically deformed rather than to be removed in the form of chips; see Fig. 4.46 [Ara09]. Even though plowing is

associated with an increase of cutting tool wear and losses in dimensional accuracy, this particular effect can be utilized to generate a regular micro-textured surface, associated with friction reducing properties [Twa14]. This allows us to apply micro-milling for both the manufacture the forming die's geometry and the tribological active micro-structured surfaces carried out in a single process step.

The prerequisite for the textured surface generation through micro-milling is the application of micro-ball-endmills with diameters in the range of 0.5 to 2.0 mm and a cutting tool alignment normal to the machined surface. The actual design of the regular texture is determined by the properties of the machined material; that is, the material hardness, the cutting strategy (up- or down-milling), and the machining parameters width of cut a_e and feed per tooth f_z [Twa14].

4.5.4.2 Micro-Tribological Investigation

Reliable and significant tribological investigations are the premise for the selection of suitable tribological active surface textures and thus the successful development of, for example, dry micro-deep drawing processes applying micro-textured forming dies. The aims of this investigation are the assessment of short-term and long-term frictional behavior and wear. However, tribological assessment in the micro-regime is challenging due to size effects, such as the dominance of adhesion, and also the application of delicate samples and experimental setups. This led to the development and application of specialized equipment for micro-tribological investigations. With regard to design and complexity of these experiments, the DIN 50322 defines six categories of setups linked to sheet metal forming processes. These categories range from I, representative for the actual forming process in industrial environment, to VI for model like experiments with simple sample geometries and equipment. The accessibility to the surfaces under test and the simplicity of the setup is improved for higher category numbers, although the comparability and transferability of the investigation's results to the real forming process is limited. Precise micro-forming presses have been developed for category I tribological experiments [Sch08a, Beh15]. Equipped with additional linear encoders and piezo-electric force measurement systems, these machines allow for the determination of punch- and blank holder forces with a resolution of 0.01 N and the punch stroke detection with a resolution of 1 μm when micro-deep drawing. Work carried out in the Collaborative Research Center 747 comprised the first deep drawing experiments using rectangular micro-deep drawing dies with textured surfaces made by micro-milling, see Fig. 4.49. The aim of this work was to increase the achievable drawing ratio β_0 by providing favorable tribological conditions [Böh14]. However, a clear increase in forming die performance due to surface texturing was not observed. This was drawn back to inaccuracies in die machining and punch-die-alignment, and also manual positioning of the blanks over the drawing cavity [Böh16].

Furthermore, geometrically scaled down strip drawing tests were carried out in the Collaborative Research Center 747 (tribological experiment category V)

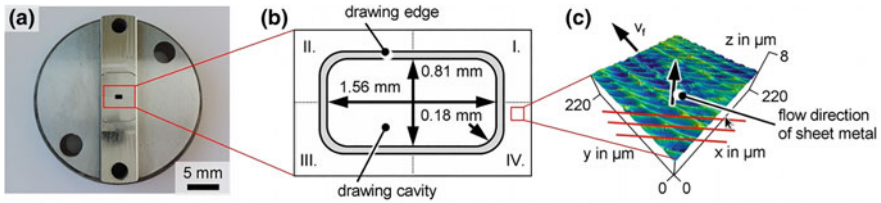


Fig. 4.49 Micro structured micro-deep drawing die **a**, design of drawing cavity **b**, and topography of micro-structured area **c** (in accordance with [Böh16])

[Bri10]. Various textured samples made from hardened tool steel that was machined by micro-milling, which were applied against strips of austenitic stainless steel. The texture design was determined by the tool diameter d and the line pitch a_e . A clear dependence of the confection of friction on the arithmetical mean height S_a of the textured samples was found. Compared to a polished reference sample, the coefficient of friction was reduced by about 20% when applying micro-textured samples with arithmetical mean heights of about $S_a = 200$ nm [Bri10].

Micro-tribometers, due to their simplicity in setup and the capability to reduce testing time compared to strip drawing experiments, are well suited for the tribological investigation of micro-textured surfaces, especially under dry conditions. A methodology for the reliable tribological investigation using a micro-tribometer in ball-on-plate configuration (tribological experiment category VI) was presented by the researchers of the Collaborative Research Center 747 [Böh18]. The spheres used as tribological counterparts were undergoing run-in procedures in preparation for tribological investigations. Here, equilibrium facet areas on the spheres are formed due to initial wear. The final size of the facet areas is determined by the sphere material and the applied normal force F_N . Once a steady state of the facet area is reached, reliable tribological investigations can be carried out without the impact of crucial changing wear and friction mechanism to the experimental result.

Tribological investigations using a micro-tribometer in ball-on-plate configuration with spheres from aluminum alloy Al99.9 exhibiting equilibrium facet areas were conducted under dry conditions. A polished reference sample and various textured samples made by micro-milling made from hardened tool steel were used in the experiments. The surface plots of four exemplary samples are shown in Fig. 4.50. The experimental setup and determined coefficients for each of the four surfaces are shown in Fig. 4.51.

The results of the micro-tribological investigations displayed in Fig. 4.51b, which clearly indicate that the surface roughness of the samples (i.e., the contact conditions at the sample-sphere-interface on microscopic level) has a distinct influence on the dry frictional properties. For the presented material combination, hardened tool steel and Aluminum Al99.9, the tribological active sample surface should ideally exhibit an arithmetical mean height S_a of about 150 nm to achieve minimum friction. A lower sample roughness leads to an increase in friction, which

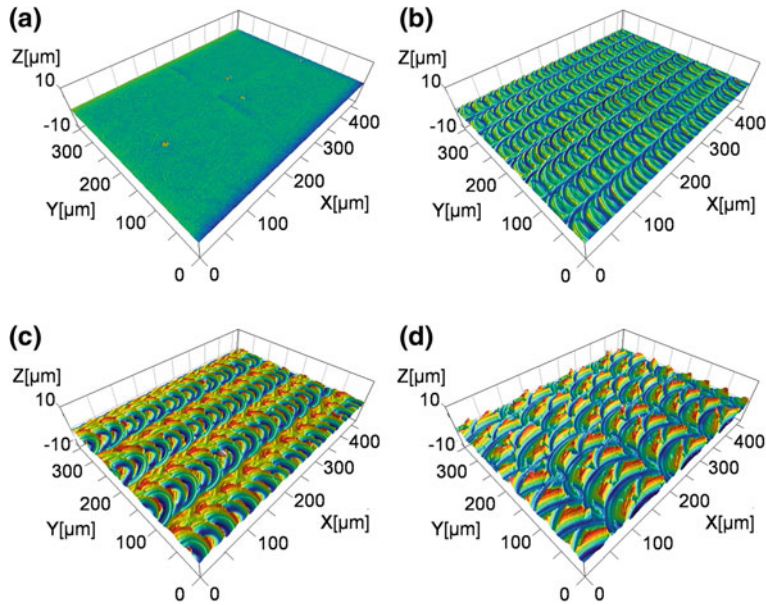


Fig. 4.50 Surface plots of samples applied in tribological testing: **a** polished reference sample R ($S_a = 24$ nm), **b** sample #1 ($S_a = 148$ nm), **c** sample #2 ($S_a = 470$ nm), and **d** sample #3 ($S_a = 741$ nm) (in accordance with [Böh16])

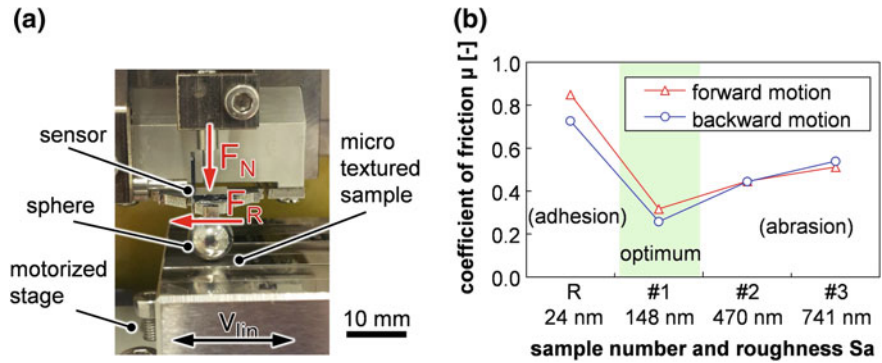


Fig. 4.51 **a** Ball-on-plate setup for frictional testing on a micro-tribometer and **b** average coefficients of friction for forward and backward motion as a function of the sample number and the associated arithmetical mean height S_a (in accordance with [Böh16, Böh18])

can be traced back to an increased impact of adhesion. Roughness greater than 150 nm is expected to promote interlocking of surface's asperities also associated with an increase of friction. However, a deeper understanding of the correlation of the surface topography and dry friction, and their mathematical description inevitably requires function orientated surface characterization ahead of common statistical roughness parameters, including suitable contact modeling.

4.5.4.3 Function Orientated Surface Characterization

The precise description of the interrelationship of the topography of a surface and their functional properties, such as the friction provoked in dry tribological contact, requires for sufficient roughness measurement and analysis techniques. The well-established, two-dimensional profilometry is not sufficient, especially when taking into concern tribological problems of micro-cold forming processes [Gei97, Ver01]. For example, profilometry does not allow to reliably distinguishing a dent from a scratch on a technical surface [Gei97]. Rather, areal measurement and characterization of surfaces is necessary. The first appropriate areal roughness measurement systems such as confocal microscopes or white light interferometers (WLI) were introduced in the ninetieths of the last century. Together with the ISO 25178 standard *Geometrical product specification (GPS)—surface texture: areal* for areal roughness analysis, released in 2012, there is today a powerful toolbox for sufficient and function orientated surface characterization.

The ISO 25178 standard distinguishes between two categories of parameters for surface characterization: areal field parameters and areal feature parameters [Lea13]. Areal field parameters comprise first of all of the statistical surface parameters (or height parameters) such as the arithmetical mean height S_a . Those parameters originate from two-dimensional profilometry and were transferred to areal surface characterization. All areal field parameters have in common, that their calculation is based on the use of every data point measured and filtered over the surface evaluation area. With regard to function orientated surface characterization the function related parameters (a sub-category of areal field parameters) are of greater relevance [Veh15b]. Function related parameters mainly comprise those parameters derived from the Abbott-Firestone curve or material ratio curve such as the material ratio corresponding to a section height $S_{mr}(c)$ or the S_k parameters determined by graphical construction. For surface characterization using areal feature parameters (these are e.g. the peak density S_{pd} or the arithmetical mean of peak curvature S_{pc}) only beforehand determined features on the surfaces are taken into account [Lea13]. These features are categorized by the areal features hills (H) and dales (D), line features such as ridge lines (R), and the punctual features peak (P) and valley (V). The determination of feature parameters from a filtered surface is carried out using watershed segmentation [Blu03]. To avoid over segmentation additional Wolf-pruning is applied [Wol84, Wol93]. Wolf-pruning removes all fractions of the surface of interest below a predetermined threshold height value. The threshold value is defined as percentage of the maximum height difference of the filtered surface S_z and is 5% by default. With regard to micro-contact and friction modeling the determination of the hills (H) and related parameters of surfaces are of greatest relevance, as they directly determine the contact state on microscopic level when interfacing with another surface and thus as

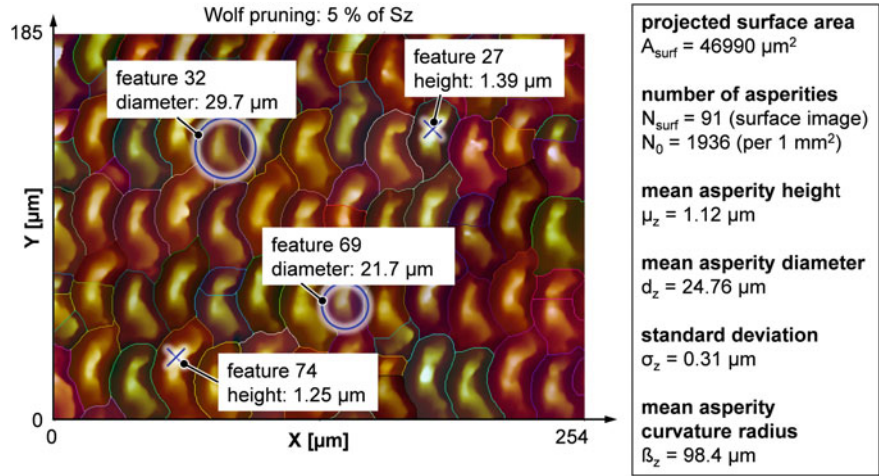


Fig. 4.52 Surface plot of an exemplary micro-textured surface generated by micro-milling and associated areal feature parameters

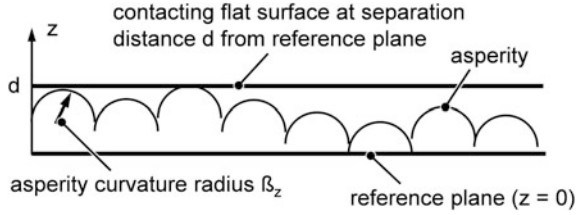
expected the dry frictional conditions. Figure 4.52 shows the exemplary segmentation of a textured surface generated by micro-milling to derive the feature parameters hill (H) and the associated surface characteristics.

4.5.4.4 Surface Micro-Contact Modeling

The rough nature of a surface provokes the formation of discrete, microscopic contact areas, when interfacing with another surface. Therefore, the fine finish of a technical surface has a considerable impact on its functional characteristics, such as friction and wear. The predetermination of these particular characteristic requires the precise description of the micro-contact state of two interfacing surfaces. This demand led to the development of various statistical micro-contact models throughout the past decades. Even though there are more sophisticated models, the contact model of Greenwood and Williamson remains the most famous and most cited model.

Greenwood and Williamson’s model describes the solely elastic contact of a rough surface with an ideally flat surface [Gre66]. The micro-geometry of the rough surface is described by some idealized properties. It is assumed that the topography consists of a large number of spherical hills or asperities, which are all of the same curvature radius β_z (coinciding with the parameter Spc) and that their heights are distributed normally. Together with mean asperity height μ_z and standard deviation of the asperity height σ_z , the height distribution can be expressed by the specific probability density function Eq. (4.11).

Fig. 4.53 Contact of a rough with an ideally flat surface



$$\Phi(z) = \frac{1}{\sqrt{2\pi\sigma_z^2}} e^{-\frac{(z-\mu_z)^2}{2\sigma_z^2}} \quad (4.11)$$

If the surfaces are pressed together until the ground level of the rough surface and the ideally flat surface are separated by a distance d , then every asperity of the rough surface will make contact with the ideally flat surface whose height was originally greater than d , see Fig. 4.53.

The probability of any asperity of the height z making contact with the flat surface can be calculated by Eq. (4.12).

$$P(z > d) = \int_d^{\infty} \Phi(z) dz \quad (4.12)$$

If the rough surface comprises of N_0 (coinciding with the parameter Spd) asperities in total, then the number of contacts will be:

$$N = \int_d^{\infty} N_0 \Phi(z) dz. \quad (4.13)$$

The real area of contact can be derived from Eq. (4.14).

$$A = \int_d^{\infty} N_0 \pi \beta_z (z - d) \Phi(z) dz \quad (4.14)$$

Taking into concern Hertzian theory of non-adhesive elastic contact and the elastic material properties of both the surfaces in contact expressed by the effective elastic modulus E^* , the total load F_N is:

$$F_N = \int_d^{\infty} N_0 \frac{4}{3} E^* \sqrt{\beta_z} (z - d)^{\frac{3}{2}} \Phi(z) dz \quad (4.15)$$

The applicability of the Greenwood and Williamson model to the micro-contact modeling of actual technical surfaces is limited due to the over-simplified assumptions regarding the micro-geometry of the rough surface. In addition, the implementation of actual technical surfaces into the Greenwood and Williamson model based on well-established parameters from two-dimensional profilometry or from the more recently introduced areal field parameter is not feasible. Serendipitously, the particular surfaces of interest (that is, micro-textured surfaces generated by micro-milling) exhibit a regular arrangement of asperity-like surface features. The assessment of these surfaces using areal feature parameters allows their implementation into the Greenwood and Williamson model, and thus micro-contact modeling for moderate loads and predominantly elastic contact behavior.

Let us consider the four surfaces (#R, #1, #2, and #3) introduced in Sect. 4.5.3.2 for micro-tribological investigation. The parameters total number of asperities N_0 , mean of curvature radius β_z , mean asperity height μ_z , and standard deviation of the asperity height σ_z were evaluated for all four surfaces using areal feature parameter analysis according to ISO 25178. The parameters were transferred to the Greenwood and Williamson model and, subsequently, the number of asperities in contact N and the real area of contact A were calculated for normal forces in a range from 1 N to 5 N assuming a projected interface area of 1 mm² and a material combination of hardened tool steel and aluminum Al99.5 ($E^* = 57,079 \text{ N/mm}^2$), see Fig. 4.54a and b. Additionally, the average force acting on an asperity F_i was calculated in dependence on the applied normal force and is shown in Fig. 4.54c).

A distinctive correlation of the friction coefficients of the surfaces measured in the micro-tribological experiments and the three evaluated parameters N , A and F_i can be derived from the diagrams in Fig. 4.54. An increase of the asperities in contact generally coincides with a decrease in friction, an increase in the real area of contact A generally coincides with an increase in friction. The same correlation was found for the average force acting on a single asperity F_i and the coefficient of friction μ . From the impressive consistency of the results shown, it can be concluded that the even though simple model of Greenwood and Williamson is

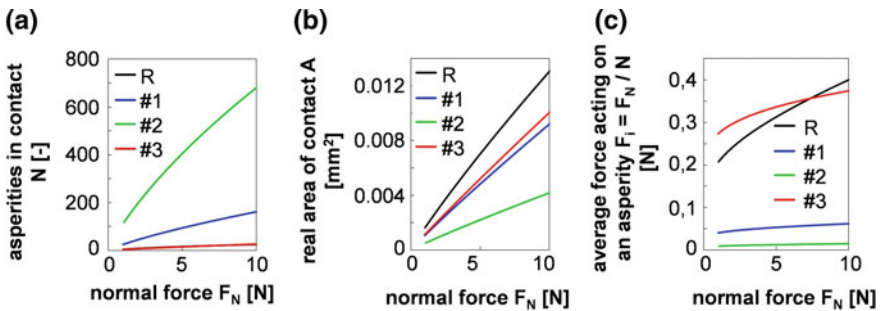


Fig. 4.54 Contact of a rough with an ideally flat surface according to [Gre66]

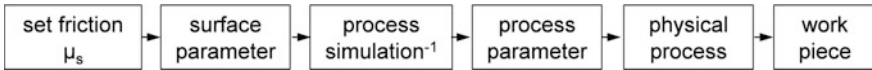


Fig. 4.55 Work flow of inverse modeling for optimized forming die manufacture

well-suited for the micro-contact modeling of textured surfaces generated by micro-milling in tribological contact. This approach builds a sound foundation for the development of scale dependent friction models, for example, based on the work of Bhushan and Nosonovsky helping to determine best suited textured surfaces for friction reduction in dry micro-sheet metal forming [Bhu04]. The application of the friction model of Bhushan and Nosonovsky with regard to micro-sheet metal forming was shown previously by and Shimizu et al. before [Shi15].

4.5.4.5 Inverse Modeling for Optimized Forming Die Manufacture

All of the introduced concepts and models are combined to find ideal process parameters for optimized forming dies. A desired friction μ_s is set and surface parameters derived from set friction. The process model is used as the forward operator in an inverse problem to find a suitable set of process parameters. These process parameters are then used in the real physical process to produce a work piece with the desired friction. The work flow is visualized in Fig. 4.55.

Overall this approach allows us to optimize manufactured forming dies by using process parameters that result in a desired friction.

4.6 Predictive Compensation Measures for the Prevention of Shape Deviations of Micromilled Dental Products

O. Riemer*, P. Maaß, F. Elsner-Dörge, P. Gralla, J. Vehmeyer, M. Willert, A. Meier and I. Zahn

Abstract Micro-milling is widely applied for the manufacture of dental prostheses because only this process guarantees geometrical accuracy and adequate surface topographies compared to novel methods such as selective laser melting. Dental prostheses require hard and tough materials like cobalt-chrome alloys or ceramics due to the demands of the application. When machining, static and dynamic interactions between the milling tool and the workpiece govern the cutting process and may worsen the work result, especially the geometrical accuracy. The deflection of the tool has a significant influence. However, deflections can be compensated through adapted manufacturing strategies by adjusting the process parameters or by optimizing the tool path, therefore increasing the quality of the final product. In the work presented, the deflection of the milling tool is compensated by readjusting tool positioning before the actual process to ensure the nominal tool position and eliminate form deviations of the workpiece. The interaction between tool and workpiece is investigated with help of micro- and macroscopic surface simulations, supported by experimental data and parameter identification. The optimization is performed through mathematical methods from the area of inverse problems, applying regularization with sparsity constraints.

Keywords Milling • Simulation • Optimization

4.6.1 Introduction

Micro-milling as part of micro-machining offers high efficiency and adaptability regarding machinable geometries and materials, while maintaining relatively high material removal rates [Veh15a]. Deploying these advantages, micro-milling is an established process for the manufacture of mold inserts and also dental prostheses (see Fig. 4.56), which require hard and tough materials, such as cobalt-chrome (CoCr) alloys, ceramics or titanium alloys.

Because mating surfaces of dental prostheses are often seated in narrow cavities with steep inclines, milling tools with large length-to-diameter ratios (up to $l/d = 18$) are necessary to machine these functional surfaces. However, these fine tools are prone to deflection as a direct outcome of the acting process forces. Shape deviations up to several tens of micrometers can be caused by the deflections and can eventually lead to a rejection of the prosthesis. Thus, applicants of micro-milling processes are obliged to enhance their technology if they wish to stay competitive.

Fig. 4.56 Dental bridge from CoCr alloy (Courtesy of Bego Medical GmbH)



A promising and universal method to meet these production challenges is to prepare an adjusted tool path via Computer Aided Manufacturing (CAM), which can help to reduce shape deviations. However, these preparations are difficult to reproduce because they always depend on the individual capabilities of the programmer and do not necessarily consider all factors responsible for shape deviations. To this day, apart from the workpiece geometry given by a CAD model, only the tool geometry and the machining strategy are considered within CAM systems, whereas material properties and the interaction of tool and workpiece leading to variable process forces and, therefore, hard to predict tool deflections are not yet considered in these systems.

Here, aiming for a better comprehension of the process itself and to investigate possible correlations between process forces, tool deflection and shape deviations, defined abstracted geometries are machined, which inhibit most the critical conditions in the manufacture of dental prostheses. The forces and the resulting shape are measured and compared for a variety of machining conditions. The obtained insights were then employed for a predictive optimization method using modeling and simulations elaborated in preliminary works [Pio15, Pio11].

The simulation based approach requires a calibration of the existing model. Subsequently, a validation and the application of the model for the process optimization are carried out. The implementation follows the diagram shown in Fig. 4.57.

First, a sufficiently precise forward model is required. Based on the work in the SFB 747-subproject *Flexible Manufacture of Tribologically Optimized Forming Tools* (Sect. 4.5), the data based model was expanded for the dental material CoCr and appropriate tools. The acquisition of the empirical data base was realized by means of a model geometry, which was developed together with the industrial partner BEGO Bremer Goldschlägerei Wilh. Herbst GmbH & Co. KG (BEGO). The calibration was carried out as an iteration, as can be seen in Fig. 4.57a; the actual optimization follows Fig. 4.57b. The calibrated model is applied for the calculation of the optimal machine control by minimizing

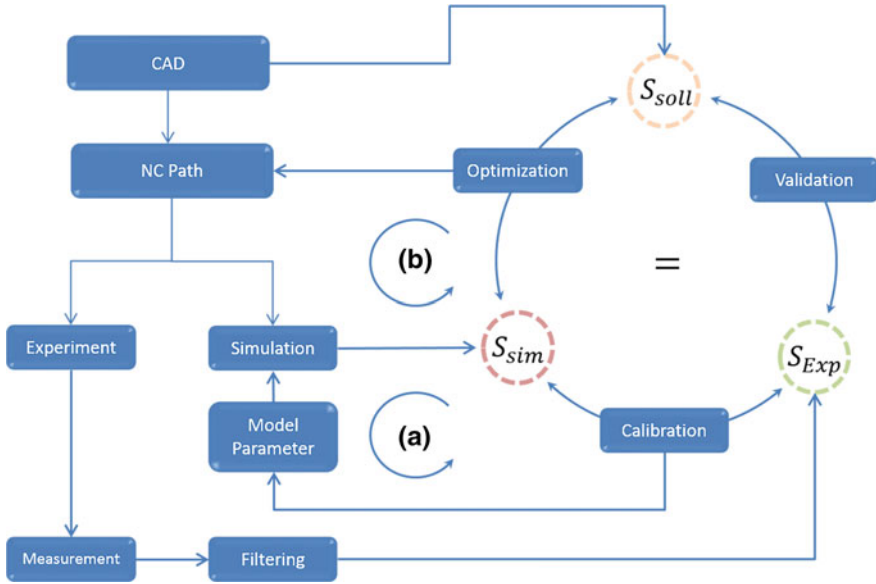


Fig. 4.57 Overview of the working steps and participation

$$\|A(u + d) - y_0\|. \quad (4.16)$$

A comparison between CAD geometry and actual measured geometry serves to evaluate the results and the model validation.

4.6.2 State of the Art and Aim

CAD/CAM-process chains for the manufacture of dental prostheses have been made possible through the expansion of cutting processes towards a miniaturization of tools and through an enhancement of machine tool precision. The main difference between micro-milling and conventional milling is the size of the applied tools and the associated structures that can be manufactured. Generally, tool or structure size range in dimensions smaller than a millimeter [Cam12].

Regarding machine tools, the manufacture of micro-components or workpieces inhibiting micro-features requires adapted machine behavior and process control. Because of the diameters of these small tools, high spindle speeds of several ten thousand up to a few hundred thousand rpm are essential to achieve adequate cutting velocities. Aside from high-frequency main spindles, means for higher position accuracy, higher stiffness and improved thermal stability of the machine system are decisive. Consequently, machine tools for micro-milling rely on technologies such as hydrostatic bearings, linear direct drives, precision scales, active cooling and controlled compensation of thermal expansion [Che10].

In contrast to conventional cutting, which employs a variety of cutting materials, micro-cutting and particularly micro-milling are almost solely performed with cemented carbide tools. For the machining of hard and tough materials, a physical vapor deposited (PVD) coating (e.g. TiAlN) is applied to reduce tool wear [Ara08]. Tool suppliers have to meet the demands for the provision of defined cutting edges because powder metallurgic tools are limited in their achievable cutting edge sharpness. In conjunction with the small chip thickness in micro-milling, effects can occur that may result in a plastic deformation (ploughing) in addition to mere cutting, in case the chip thickness falls below a critical minimum. Consequently, process forces can increase and often be the cause of unpredictable tool damage [Uhl14].

Tool deflection during micro-milling was examined by Dow et al. by machining slots with a linearly varying depth and circular grooves with a radius of 80 μm and a depth of 0.50 mm in hardened tool steel. In the first case, a non-linear relationship between the machining force and the tool's deflection was discovered. In the second case, the sweep angle in combination with the tool feed direction was determined as a significant factor for the tool's deflection. The eligibility of their developed model regarding compensation of the deflection was proven [Dow04].

In a study conducted by Kim et al., similar results were obtained. Here, a half-cylinder was machined by ball end milling with 10–16 mm diameter tools and, therefore, cannot be ranked among micro-milling processes [Kim03].

4.6.3 Applied Materials and Methods

Workpiece Materials

To parameterize the surface model established in Sect. 4.5 [Pio11, Veh12, Veh15a, Veh17b], the model inherent cold work steel was machined with a milling tool inhibiting a large length-to-diameter ratio of $l/d = 12$, cf. Tables 4.6 and 4.7. Subsequently, the adapted model was transferred to the machining of SLM-generated CoCr dental material.

Machine Tool, Force Measurement and Position Measurement

The machining experiments were for the most part carried out on a DMG Sauer Ultrasonic 20 linear micro-milling center, as depicted in Fig. 4.58. The tool path was programmed with the commercially available CAM software CimatronE. For a comparison of the achievable accuracy (cf. Fig. 4.64), experiments were also conducted on a Rödgers RXP500 using DentMILL as CAM software.

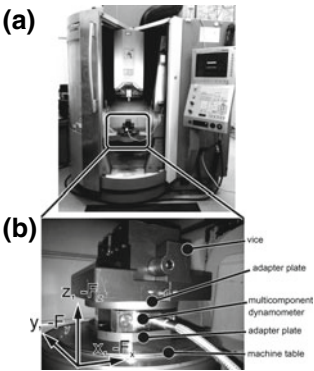
Forces were measured with a Kistler multicomponent dynamometer with a sampling rate of 10,000 Hz. A method for the synchronized recording of force and position was developed to enable a subsequent correlation of geometry, forces and the resulting shape deviations. Therefore, the force signals of the multicomponent dynamometer were recorded simultaneously with the analogue position signals of the x-, y- and z-axes and plotted synchronously to allow for an allocation of forces to distinguish the geometric features of the machined elements.

Table 4.6 Material data of the applied workpiece materials

Material	Cold-work steel	CoCr
Specification	1.2379 (X 155CrVMo-12-1)	Wirobond [®] MI+
Alloy elements	C (1.55)	Co (63.8)
	Si (0.4)	Cr (24.8)
	Mn (0.3)	W (5.3)
	Cr (11.8)	Mo (5.1)
	Mo (0.75)	Si (<1)
	V (0.82)	
Hardness	Max. 64 HRC	36.6 HRC
Density	7.7 g/cm ³	8.5 g/cm ³
Tensile strength	>2,000 N/mm ² (hardened)	970 N/mm ²

Table 4.7 Milling tool specification for machining of hardened steel and CoCr

	Hardened steel	CoCr
Type	Cemented carbide ball end	Cemented carbide ball end
Tool radius r	0.25 mm	0.5 mm
Length l	6	12 mm
Number of flutes z	2	2
Coating	(Al, Ti, Si)N	TiAlN
Spindle speed n	36,000 min ⁻¹	38,000 min ⁻¹



machine tool	DMG Sauer ULTRASONIC 20 linear
structure	5-axes-portal
max. rpm	60,000 min ⁻¹
max. feed rate	40,000 mm/min
travel X / Y / Z	200 / 220 / 280 mm

Fig. 4.58 a Machine tool; b machining setup

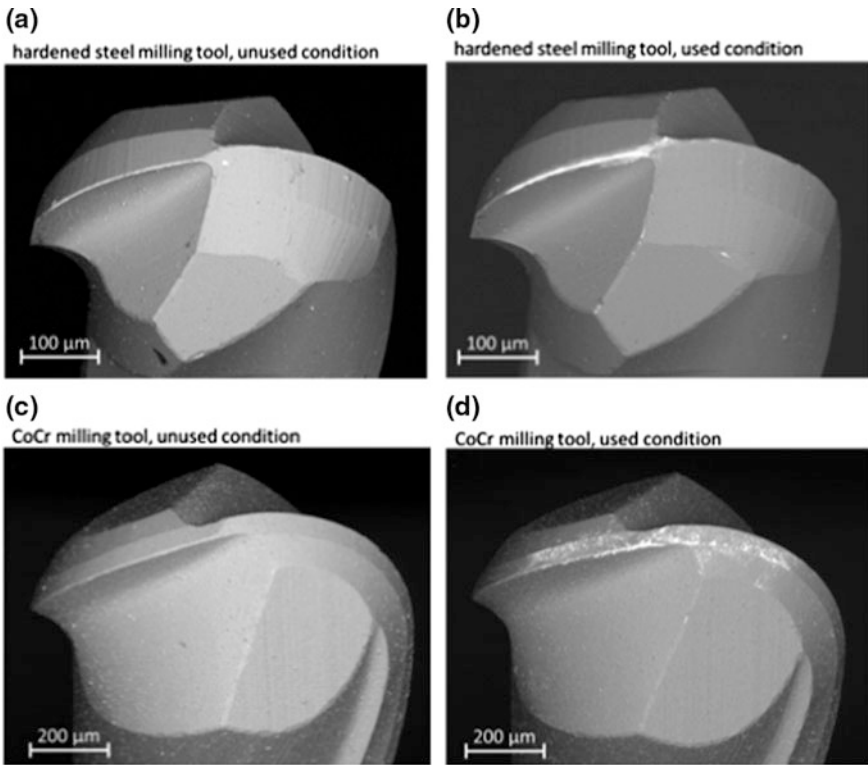


Fig. 4.59 SEM images of applied ball end mills in fresh and used condition

Applied Milling Tools

Cemented carbide two edged ball end mills with a TiAlN coating were applied for the experimental procedures, both for the hardened steel and CoCr workpiece materials. Because the different manufacturers could not provide corresponding tool geometries, a compromise was made by maintaining a matching length-to-diameter ratio of $l/d = 12$ for both materials, whereas the radius r and length l are larger by a factor of 2 for the CoCr milling tools, as given in Table 4.7 and shown in Fig. 4.59.

Tool wear was investigated by scanning electron microscopy after an approximate cutting distance of 3000 mm, as shown in Fig. 4.59. While the milling tools for hardened steel showed slight coating flaws in the delivered condition, which indicated by the brighter areas on the cutting edge, the tools for CoCr were in a faultless condition. Both tool types showed a similar wear characteristic after machining. On the cutting edge, the coating has worn off and the highest tool wear can be located in proximity to the tool center, as expected due to the contact conditions during machining. Additionally, the CoCr showed signs of wear on the rake face and flank but no critical thresholds were exceeded for any of the applied tools.

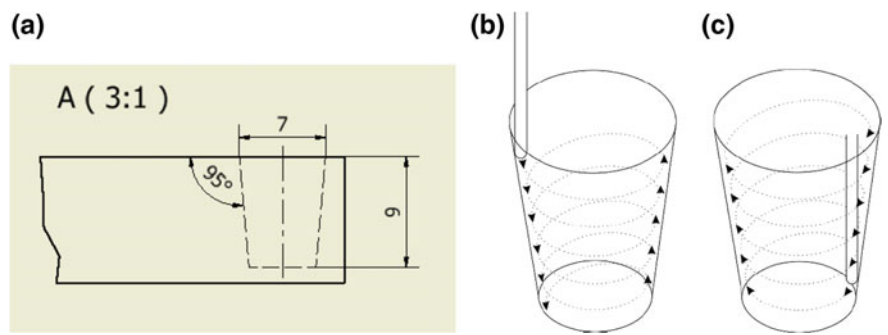


Fig. 4.60 a Geometry of cone; different machining strategies: b spiral pressing cut, c spiral pulling cut

Test Geometries, Machining Parameter/Strategy and Metrology

To make a comparison between the different CAM-programs (CimatronE and DentMILL) and machine tools (DMG Sauer and Rödgers) regarding the achievable accuracy, application oriented geometries in the form of concave cones dimensionally in the range of connective elements of dental implants were machined, cf. Fig. 4.60. Two different strategies were applied (spiral pressing cut and spiral pulling cut).

The workpiece geometry for the subsequent experimental investigations (parameterization etc.) was a linear arc ridge consisting of two plane faces and three segments of a circle with the same radius merging into each other, as shown in Fig. 4.61. These defined abstracted geometries represent the critical conditions in the manufacture of dental prostheses, while at the same time an easy metrological assessment is possible. These geometries were machined into the cobalt-chrome alloy manufactured by selective laser melting (SLM).

The arc ridges were machined according to different strategies. As described in [Rie16, Rie17b], the tool was moved alongside the ridge (longitudinal) and across

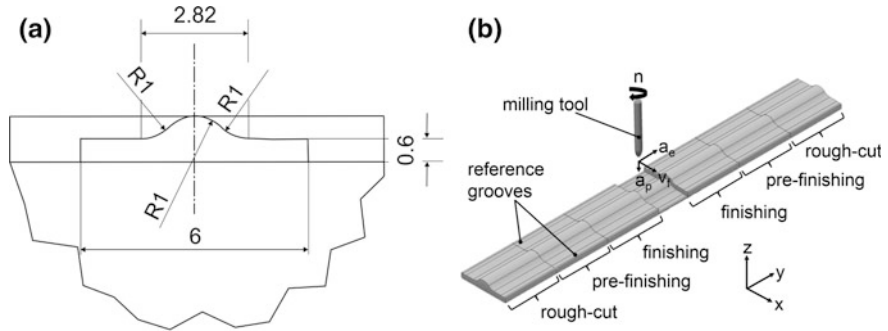


Fig. 4.61 a Geometry of the arc ridge for CoCr (geometry for steel was half the dimensions); b machining strategy

Table 4.8 Machining parameters

Material	Cold-work steel				CoCr			
a_e (mm)	0.010	0.015	0.020	0.025	0.04	0.08	0.12	–
v_f (mm/min)	500	500	500	500	1,000	1,300	1,600	1,900

(transverse) to reveal influence of deflections for pulling and pressing cut, and to analyze different contact conditions of the tools’ cutting edge and the workpiece. Additionally, a series of experiments were carried out where only the transverse strategy with pulling cut was applied.

The finishing cut was the final cut after a rough cut and a pre-finishing cut. Rough cuts and pre-finishing cut were the same for each arc ridge and only the finishing cut was conducted with different parameters. According to Fig. 4.61, the symmetric arc ridge was divided into six segments. The outer segments were kept in the state after the rough cut, the segment next to it in the state after pre-finishing and only the inner segments were finished. This was done to guarantee a comparison of the shape before and after finishing.

For the test series with hardened steel as workpiece material, the spindle speed was kept constant at $n = 36,000 \text{ min}^{-1}$. The same applied for the axial infeed and feed rate, which were kept constant at $a_p = 4 \text{ }\mu\text{m}$, $v_f = 500 \text{ mm/min}$ respectively. Radial infeed a_e was varied according to Table 4.8.

For the test series with CoCr as workpiece material, the spindle speed was kept constant at $n = 38,000 \text{ min}^{-1}$. The same applied for the axial infeed, which was kept constant at $a_p = 20 \text{ }\mu\text{m}$. Radial infeed a_e and feed rate v_f were varied according to Table 4.8. For all materials and parameter variations, up milling was chosen to incite significant force signals. The inclination angle of the tool was kept constant at $\beta = 0^\circ$.

The tool path was programmed with CimatronE CAM software. In total, 24 arc ridges were micro-milled. The resulting shape was measured with a KLA Tencor profilometer P-15 and compared to the target geometry. The resulting shape after machining—that is, the measured surface profile (dotted orange line Fig. 4.62b)—was measured tactilely with the profilometer. Reference geometries in the form of two radial grooves, as depicted in Fig. 4.62, were machined in advance into the plane surfaces of the arc ridge to align the measured surface profile with the target geometry in x- and y-direction by removing the offset and thus guaranteeing an exact fit of target geometry and measured geometry.

The results for the steel experiments regarding force measurements show that surface roughness will be recapitulated briefly ahead because their relevance to the subsequent simulations and optimization is subordinate. Generally, the results show a qualitative resemblance to the results obtained with the CoCr material, which will be discussed in detail in the following chapters. The progression of the vertical force across the arc ridge geometry was almost symmetric, with the highest values registered on the plane surfaces and the peak. The force increased with radial infeed a_e from $F_z = 1.5 \text{ N}$ up to $F_z = 3 \text{ N}$. The same applies to the surface roughness,

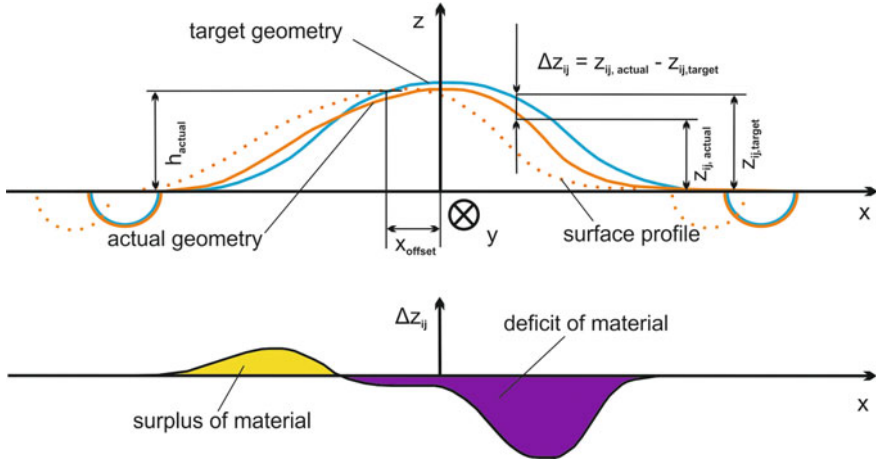


Fig. 4.62 Schematic principle of shape deviation evaluation

where a dependency between radial infeed and roughness value R_a can be confirmed. R_a increases from $R_a = 225$ nm up to $R_a = 400$ nm with increasing a_e according to Table 4.8. The obtained insights were applied for the parameterization of the model established in the SFB 747-subproject C2.

Simulation and Modeling

The simulation-based method consists of a geometric surface model and a kinematic process model. Therefore, geometric data processing for workpiece and tool volumes, and for concepts for offsetting path manipulators are applied [Veh17b]. The estimation of cutting forces is based on regression [Den14]. The surface model mainly provides the interface surface between the workpiece volume and the swept volume of the moving tool. The interface can be calculated for both microscopic and macroscopic scale. The differences are not primarily the sampling accuracy of the underlying computation grids but are more closely related to simplifications in modeling; that is, size effects like the minimum chip thickness, accuracy of cutting edge approximation and simplification in kinematics [Veh12]. From a mathematical point of view, both scales differ in the regularity and, therefore, in numerical treatment of the optimization.

The surface model is also applied to determine the geometry of the contact zone between tool and workpiece to estimate the load F . The interaction is modeled by a one mass oscillator, equation

$$m\ddot{\delta} + d\dot{\delta} + k\delta = F \quad (4.17)$$

with tool deflection δ and cutting force F . The physical constants m , d , k depend on the process dynamics and are treated as scalar model constants, identified with help of parameter identification methods.

Mathematical Optimization and Parameter Identification

The obtained mathematical model is used to find process parameters that will reduce the deviation of the surface. For parameter identification in calibration and to reduce deviation in the manufacturing process, mathematical optimization and inverse problem methods are used. The forward model is noted with A and takes the parameter $u \in U$ as input, which is mapped onto the measurement $v \in V$ by the model A . In parameter identification, F and v are known and a suitable u has to be found. This can be done by minimizing

$$\|A(u) - v\|, \quad (4.18)$$

which in the ideal case has a minimum of 0. If only the right-hand side of the equation

$$A(u) = v \quad (4.19)$$

is of interest, then the resulting problem is a optimization problem. If the parameter u itself is of interest, for example for indirect measurements or to find true model parameters, then the problem at hand is an inverse problem [Rie03, Lou01]. The boundaries between these two cases are not strict and some methods are used for both aspects of parameter identification. In the subproject C2 of the SFB 747 inverse methods were used to identify model parameters from experiments through indirect measurements. This still holds true for the model parameter selection in this subproject T4 because it is based on the same model. In addition, the field of inverse problems addresses the issue of noised data and ill-posed problems. Noised data means that instead of ideal data v or measurements, a small perturbed version v^δ is known. An ill-posed problem refers to characteristics of the model A , which will result in large deviations of the reconstructed u if v^δ has small perturbations. In combination, this leads to small error in measurements to large error in the parameter identification. To solve this issue, several different types of regularizations are used to handle the ill-posed nature of the model. In Fig. 4.63, the forward model and inverse problem are visualized.

The micro and macro models used in this work are both ill-posed and need regularization for parameter identification. Tikhonov's method with classic and

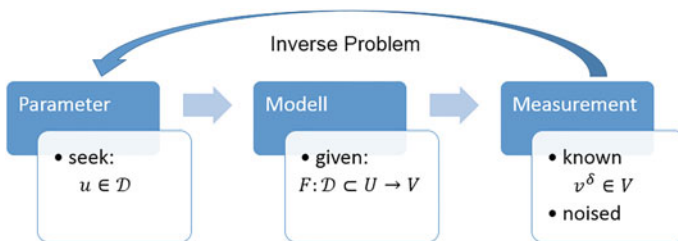


Fig. 4.63 Visualization of inverse problems

sparsity penalty terms are used to handle the ill-posed nature of the model at hand. For Tikhonov Regularization a functional

$$J_{\alpha,\delta}^{p,q}(u) = \frac{1}{p} \|A(u) - v^\delta\|_p^p + \alpha \frac{1}{q} \mathfrak{R}_q(u) \quad (4.20)$$

is minimized. This functional consists of two terms: a discrepancy term that minimizes the distance between simulated and given data and a penalty term on the parameter u that stabilizes the parameter identification. A classical choice for \mathfrak{R}_q is $\mathfrak{R}_q(u) = \|u\|_q^q$ with $q = 2$ or sparsity regularization a certain structure of few active basis elements for the parameter in a defined basis of the space U is assumed. While a l_0 -norm on the basis coefficient would best represent this idea, it is not very practical for numerical computation. Instead, a l_1 -norm on the basis coefficients of is used as penalty term (for more information on sparsity see [Jin12]).

Since the model A is non-linear, iterative methods are used to find the desired minimizer. Depending on the parameter type different methods are used. For small dimension vector parameters, a sequential quadratic programming (SQP) and gradient descent solver are used [Boy14]. To compensate the deviation of surface, the cutting tool path needs to be adjusted. This leads to a high dimensional parameter and, therefore, too many cost intensive iterations for a SQP or gradient descent method. To reduce the dimension, a greedy approach is used by dividing the tool path into i intervals of equal length. Therefore, the parameter u is a composition of parameters u_k on the defined intervals. Instead to finding u at once each u_k is found in succession of the prior U_{k-1} . This leads to multiple minimization problems which are based on solutions found on the first intervals. This way the dimension of each minimization problem is reduced; however, the resulting composition of all u_k might not be a local minimum on the whole tool path.

Processing the row data is essential for comparison and application in optimization. Because simulation and measurement need to be aligned, a shift on the x, y, z -axis and rotation of the measurement is determined by comparing simulated, v_s , and measured, v_m , data by minimizing

$$\int_{\Omega} (v_s(s) - S(x, y, z; \text{rot}_z(\varphi; v_m(s))))^2 ds \quad (4.21)$$

over x, y, z, φ , where S is the shifting operator on the x, y, z -axis and $\text{rot}_z(\varphi; \cdot)$ a rotation around the z -axis by φ in radian. This minimization is done once for a measurement. The noised data for parameter identification is then

$$v^\delta = S(x, y, z; \text{rot}_z(\varphi; v_m)). \quad (4.22)$$

Through this adjustment, the shape of simulated and measured surface can be compared directly. While this is enough in practical applications, it hides symmetrical under and overcuts in the process. For the arc ridge, this means that under and overcut can be partly compensated by a single shift in y -axis. To understand an underlying cause of deviation in surface profile, this compensation is unwanted.

Therefore, two parallel cuts on the left and right of the arc ridge were made and used to find the shift and rotation of the measurement. Consequently, process deviations are being looked at rather than shape deviations. The actual shape deviations will be less or equal to the process deviations.

4.6.4 Results

Comparison of Machined Cones

The machined cones were measured with a coordinate measuring machine, a Ferranti Merlin MK 2 Twin Star. The diameter was measured at three different heights with each 36 measurement points and compared among each other and to the nominal value, cf. Fig. 4.64. The deviation from the ideal circular form was also determined and subjected to comparison.

While in no case the nominal value of the diameter could be attained, it is apparent that the spiral pressing cut provides better results than the spiral pulling cut, both regarding the diameter and regarding the shape deviation. Comparing the facilities at BEGO and LFM, both can approximately deliver the same results, which is crucial for a possible transition of optimization methods between the two partners.

Force/Position Measurements for CoCr

On the basis of priority, the results for the longitudinal strategy will not be discussed here but are described in detail in [Rie16, Rie17a]. While in x- and y-direction signals were for the most part overlaid by noise, the most explicit signals were obtained in z-direction for the vertical force F_z . Here, every milling line can be recognized (s. Fig. 4.65a) and detailed progression of F_z for a single line can be achieved by zooming in, see Fig. 4.65.

A simultaneous plot of the z-position together with F_z over time provides comprehension about the coherence of acting forces depending on the position of the tool, as depicted in Fig. 4.65b. Obviously, the force changed depending on the geometry of the arc ridge, and thus the contact conditions of the tool. To allow for a position specific evaluation of the force, the arc ridge was divided into five sections in the x-direction, compare Fig. 4.65b. Observing the process from the middle of the arc ridge in Sect. 3, the forces showed an almost symmetric progression. A comparison of the average vertical force F_z in all five sections is given in Fig. 4.65. High forces were recorded on the plane surfaces in arc ridge sects. 1 and 5 as well as on the convex arc in Sect. 3 but it decreased in the circle segments (concave arcs in Sects. 2 and 4). The forces for Sect. 4 are slightly higher than those for Sect. 2, which can be traced back to the downward movement of the tool in Sect. 4.

Regarding the influence of the machining parameters, the maximum vertical force reaches up to $F_{z, \max} = 3 \text{ N}$ for a radial infeed of $a_e = 0.04 \text{ mm}$. For the higher radial infeed of $a_e = 0.08 \text{ mm}$ the maximum vertical force reaches up to $F_{z, \max} = 9.5 \text{ N}$. Comparing the minimal and maximal values for the different feed rates, two circumstances are remarkable. In general, higher feed rates result in

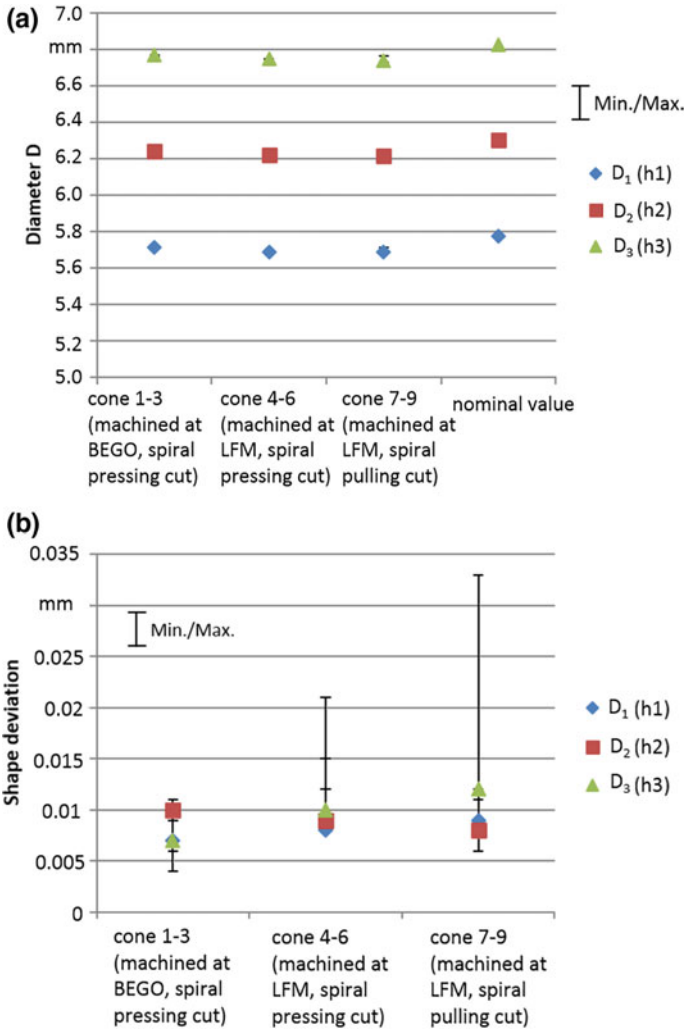
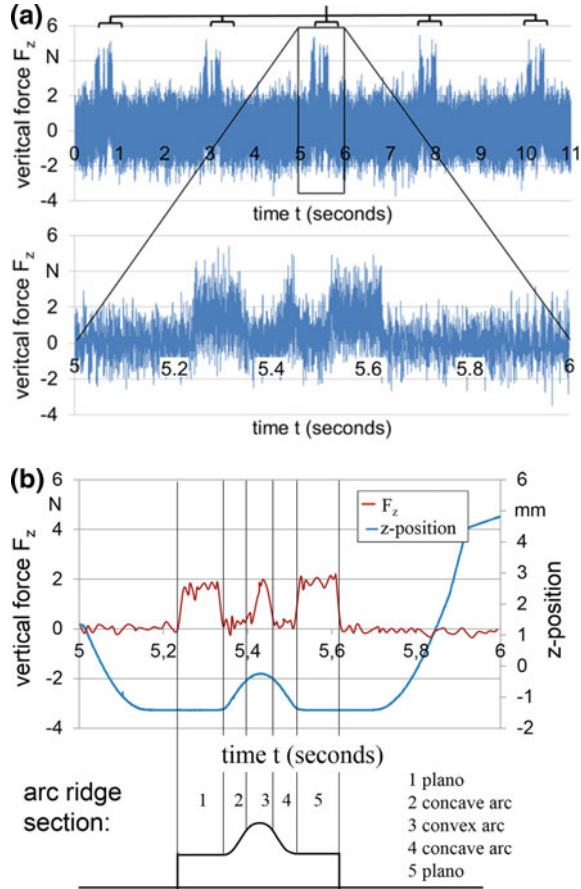


Fig. 4.64 **a** Measured diameter and comparison to target diameter; **b** measured deviation from an ideal circle

higher forces although the force values for feed rates $v_f = 1,300$ mm/min and $v_f = 1,600$ mm/min are very similar for both radial infeeds ($F_{z, \min} = -0.5$ N; $F_{z, \max} = 4.5$ N). For $v_f = 1,900$ mm/min. Meanwhile, the force for $a_e = 0.08$ mm is particularly high with a maximum of $F_{z, \max} = 9.5$ N (Fig. 4.66).

The influence of the radial infeed a_e is more distinct. The difference between $a_e = 0.04$ mm and $a_e = 0.08$ mm is at least $\Delta F_z = 3$ N in-between the plane and convex arc section. In the concave arc sections, the forces are lowest and also differ only marginally for all parameter combinations.

Fig. 4.65 **a** Force measurement plot of five milled lines and zoomed single milling line; **b** correlation of average vertical force F_z (blue) and z-position (red) and sections of actual arc ridge geometry shown below (not true to scale)



For all progression of forces, $F_{z, \max}$ is registered in Sect. 3 of the arc ridge but not on the peak of the arc ridge. In all cases, the highest force has a displacement to the right (i.e. in the direction of Sect. 4), which is most likely caused by a bending of the milling tool.

Surface Roughness

The surface roughness was investigated by white light interferometry and the parameters S_a and S_q were derived (Gaussian filter ISO 11562; 80 μm cut-off) to evaluate the influence of the machining parameters on the surface quality. The average roughness ranges from $S_a = 130 \text{ nm}$ to $S_a = 390 \text{ nm}$ and, respectively, from $S_q = 170 \text{ nm}$ to $S_q = 480 \text{ nm}$, as shown in Fig. 4.67. Except for the lowest feed rate $v_f = 1,000 \text{ mm/min}$, the surface roughness increases with a higher radial infeed a_e . The influence of the feed rate itself does not become as apparent but a tendency for higher roughness when applying higher feed rates is visible. Correlating the surface roughness to the forces in the preceding chapter, it becomes obvious that higher forces indicate a higher surface roughness.

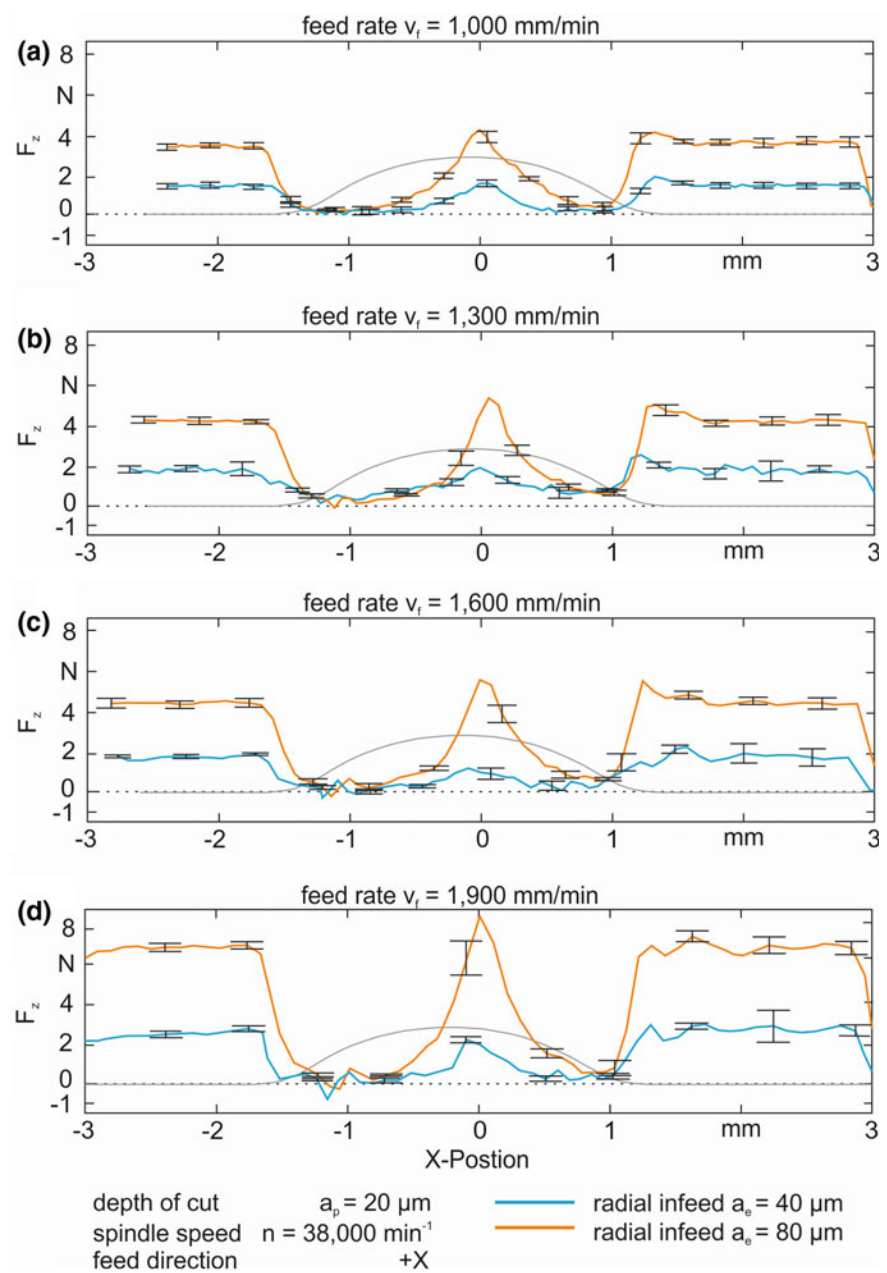


Fig. 4.66 Average vertical force F_z for different sets of v_f and a_e in the five sections of the arc ridge (transverse machining strategy)

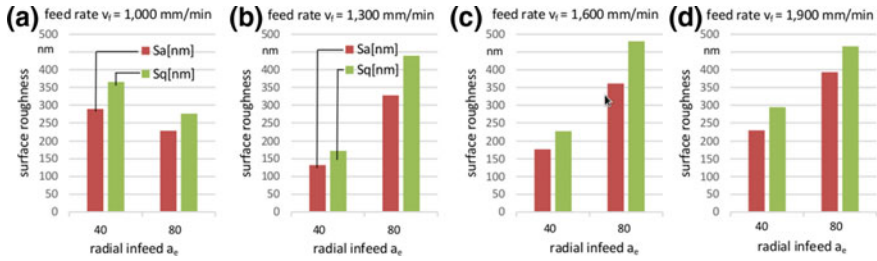
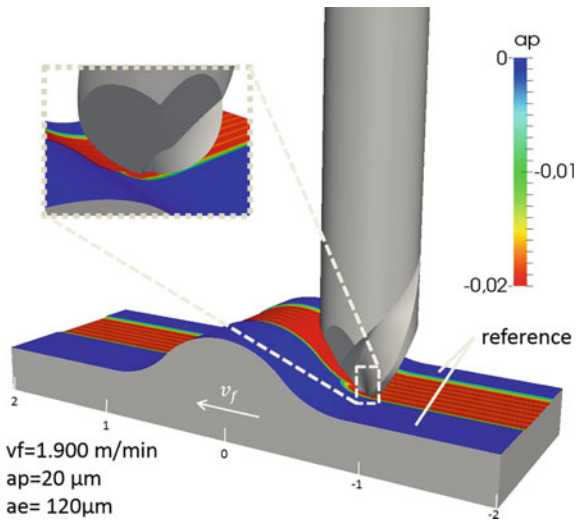


Fig. 4.67 Surface roughness S_a and S_q depending on the feed rate v_f and the radial infeed a_e (transverse machining strategy)

Fig. 4.68 Simulation setup for the transversal machining campaign



Simulation Results

In the first step, process dynamics were analyzed and, therefore, the transversal tool path was chosen. The simulation setup is illustrated in Fig. 4.68.

In Fig. 4.69a the simulated function of uncut chip thickness is shown and the removed volume along the ridge is visualized in Fig. 4.69b. Due to the cavity in the order of the tool diameter, the plotted function indicates peak forces at the transition from flat to sloped shape, which can be explained by the sudden engagement of the outer parts of the cutting edges. Furthermore, a slight difference between pulling and pressing cut can be stated from Fig. 4.69.

The simulated and the reference surface profiles are shown in Fig. 4.70a, the distance of both is plotted together with measurement results in Fig. 4.70b. The measurement is represented by a tolerance area, which is determined through three experiments. Measurements and simulation show a good agreement with neglected dynamics of the cutting tool; that is, $m = d = 0$ in the dynamic behavior of the

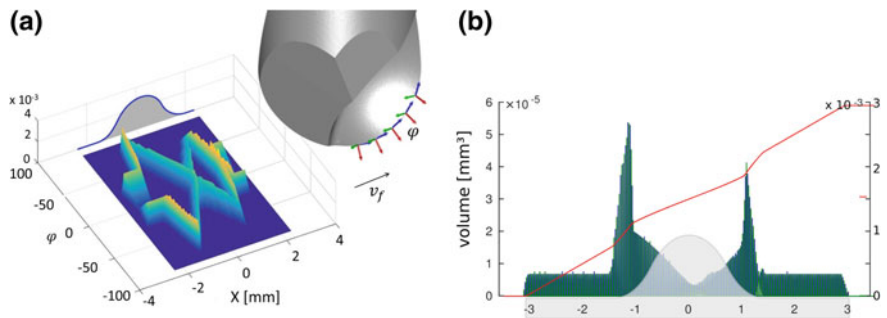


Fig. 4.69 **a** Simulated function of uncut chip thickness; **b** removed material volume along the ridge

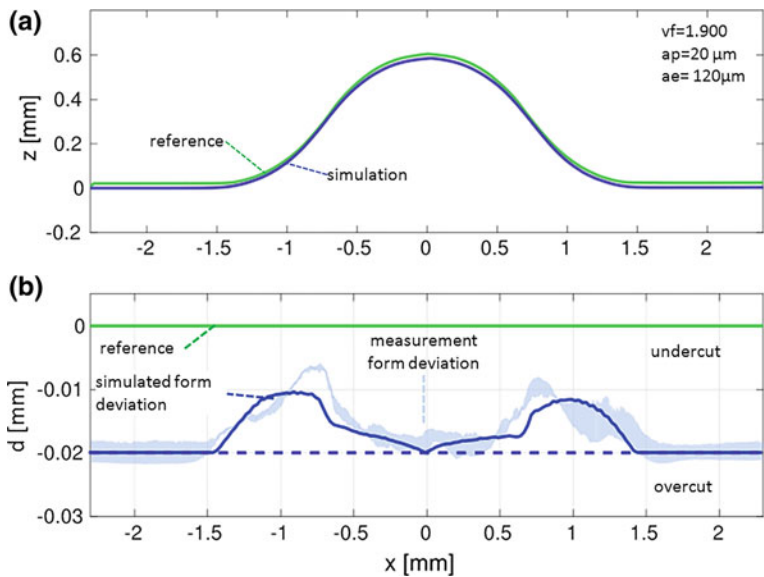


Fig. 4.70 **a** Simulated surface profile and reference; **b** form deviation (distance) of the reference and the final surface (simulation and measurement)

cutting tool. However, this does not mean that there is no deflection of the tool in the model. The dynamic behavior has a delay effect on the deflection with small effects on the surface and does not improve the conformity in the range of the chosen cutting parameters. The longitudinal milling strategy is generally insensitive to oscillations of the cutting tool. The static method is used for further simulations.

4.7 Thermo-Chemical-Mechanical Shaping of Diamond for Micro Forming Dies

Ekkard Brinksmeier, Oltmann Riemer* and Christian Robert

Abstract Diamond reveals outstanding properties such as high hardness, low wear against mechanical load, high chemical inertness against most aggressive chemical liquids and a very low friction coefficient against metals. Therefore, diamond appears as a suitable material for micro forming tools, especially when provided with micro-structured surfaces; thus, the results of forming processes will be improved compared to tools with smooth surfaces. For machining single crystal diamond, the thermo-chemical effect between diamond and selected carbon-affine metals like iron or nickel at high temperatures was exploited. Major findings of this investigation reveal that, besides graphitization, the diamond removal is governed by oxidation, while diffusion was not detected. This thermo-chemical-mechanical shaping process was successfully applied for micro-structuring of single crystal diamond.

Keywords Diamond • Thermo-chemical machining • Material removal • Micro structure

4.7.1 Principles of Diamond Machining by Using Thermo-Chemical Effect

Although diamond is mostly chemically inert, there are materials which react with diamond, causing excessive wear of the diamond. This effect is based on the reaction kinetics of diamond, which is metastable under normal conditions. Figure 4.71a shows the pressure–temperature phase and the transformation diagram for carbon [Che13]. The solid line (Berman–Simon line) which starts at 1.7 GPa and 0 K (point 1) represents the equilibrium phase boundary between stable diamond plus metastable graphite (region A) and stable graphite plus metastable diamond (region E). Region C shows the liquid phase of carbon. The dashed line above triple point 2 marks the temperature/pressure threshold of the very fast and complete solid–solid transformation of graphite to diamond [Bun96]. Above this dashed line, marked as region B, transformation yields cubic-type diamond. Region D represents a full graphite transformation. Furthermore, Fig. 4.71a shows the typical high-pressure–high-temperature regime (region f) for commercial synthesis of single crystal diamond by catalysis [Bun96] and the typical chemical vapor deposition (CVD) regime (region h) for the synthesis of diamond [Ass02]. Region g represents the fast temperature–pressure regime of diamond–graphite transformation.

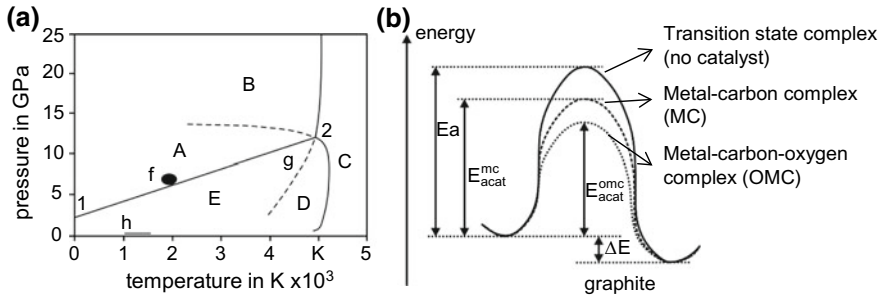


Fig. 4.71 Pressure–temperature phase and transformation diagram of carbon according to [Ass02, Bun96] (a); and energy reaction diagram of diamond to graphite [Pau96] (b)

At normal conditions (room temperature and normal pressure), diamond is thermodynamically metastable. Nevertheless, a transformation of diamond to graphite under normal conditions is not detectable, due to the required high activation energy (Fig. 4.71b; transition state complex). Even so, there are some catalytic metals like iron, nickel, molybdenum or vanadium that can decrease the required activation energy to graphitize diamond (Fig. 4.71b; metal–carbon complex). Paul et al. [Pau96] proposed that transition metals with unpaired d-shell electrons decrease the required activation energy. Furthermore, they suggested that the number of unpaired d-shell electrons is proportional to the transformation rate obtained during diamond machining experiments. Thus, for example, iron with four unpaired d-shell electrons should produce a higher transformation rate than cerium with one unpaired d-shell electron. Measurable quantities of diamond–graphite transformation start under normal pressure at around 700 °C. Once the diamond comes into contact with the transition metal at elevated temperature, the C–C bonds are stretched and afterwards destroyed. Unbound carbon atoms can subsequently diffuse into the transition metal, graphitize, react with ambient oxygen to form CO or CO₂ (Fig. 4.71b; metal–carbon–oxygen complex), or react with the metal to form carbides [Pau96].

This effect of increased diamond transformation in contact with transition metals has been used by different researchers to polish single [Tat16] and polycrystalline diamond [Wei01] by the technique of dynamic friction polishing. The principal setup of this technique is a fast rotating metal plate made of carbon-affine metals like iron, nickel, manganese or molybdenum, which is pressed against the diamond. To increase the contact temperature between the metal plate and the diamond, the contact force is increased or external heating is used to heat the metal plate or the diamond, respectively. A typical setup for dynamic friction polishing is shown in Fig. 4.72 to polish single crystal diamond [Suz03].

Chen et al. [Che09] utilized the thermo-chemical polishing technique to machine polycrystalline diamond composites with a diameter of 12.7 mm. The specimens contained about 75% diamond particles with a grain size of about 25 μm and an initial surface roughness of $R_a = 1.7 \mu m$. The remainder of the specimens consisted

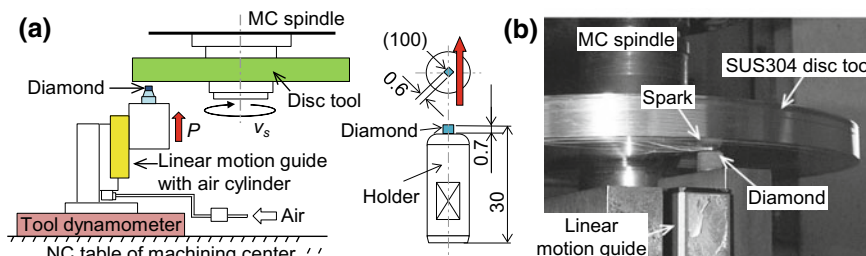


Fig. 4.72 Schematic illustration of dynamic friction polishing method (a) and polishing experiment on a machining center (b) [Suz03]

of SiC and Si and were pressed against a metal plate made from 1.4301 steel. The contact pressure between the diamond and metal plate was chosen between 2.2 MPa and 5.5 MPa, and the sliding speed of the rotating metal plate between 8 and 31 m/s. To characterize the technique of friction polishing without external heating for polycrystalline diamond composites, Chen et al. were able to develop a material removal map and determined three different working regimes, which are divided into zones with low material removal rates, safe removal and a cracking zone, depending on the contact pressure and sliding speed. By using experimental parameters (e.g. 25 m/s and 2.7 MPa), the diamond removal rate amounts to 0.084 $\mu\text{m}/\text{min}$ and the achieved surface roughness of the diamond reaches down to $R_a = 50$ nm after 18 min polishing time.

To understand the influence of the ambient gas during dynamic friction polishing, Suzuki and co-workers [Suz03] investigated the diamond removal mechanism in various atmospheres. Non-heated polishing experiments were carried out on single crystal diamonds (0.6 mm \times 0.6 mm \times 5 mm) which were pressed with 100 MPa against a rotating metal plate (sliding speed $v_s = 2500$ m/min) made from 1.4301 steel. As the ambient gas, air, oxygen, argon and nitrogen were applied. Suzuki et al. could show that polishing in air and under argon atmosphere led to similar diamond removal rates of 900 $\mu\text{m}/\text{min}$ and 920 $\mu\text{m}/\text{min}$ respectively. Polishing under oxygen atmosphere enhanced the diamond removal rate to 1480 $\mu\text{m}/\text{min}$, whereas a nitrogen atmosphere reduced the diamond removal rate to 820 $\mu\text{m}/\text{min}$. These high diamond removal rates are attributable to the high contact pressure, which generates a high contact temperature. With respect to the experiments performed and the subsequently executed investigations, the authors concluded that there is no effect of oxidation under argon and nitrogen atmospheres. The basic mechanism in this experiment is a rapid diffusion of carbon into the stainless metal plate, while oxygen increases the diamond removal strongly.

To exploit the higher diamond wear affected by ambient oxygen, Wang et al. [Wan06] investigated thermo-chemical polishing assisted by a mixture of oxidizing agents, which are KNO_3 , NaOH , $\text{KNO}_3 + \text{NaOH}$ and $\text{KNO}_3 + \text{LiNO}_3$. The chemical vapor deposited diamond films exhibited a surface roughness of 8 and 17 μm before polishing. Aluminum was chosen as the material for the metal plate,

which has no thermo-chemical effect on the diamond. Therefore, the diamond wear potential of the oxidizing agents can be identified separately. As the second plate material, iron was used to investigate the interaction between iron and the oxidizing agent. For all experiments the metal plate was preheated to 350 °C. Wang et al. could show that all oxidizing agents have a diamond removal effect after 3 h of polishing at a pressure of 0.1 MPa and a rotating speed of 81 rpm. The highest diamond wear was achieved with the mixture of $\text{LiNO}_3 + \text{KNO}_3$ with 1.2 mg/cm²/h. When using the iron plate and the $\text{LiNO}_3 + \text{KNO}_3$ mixture, the diamond wear increased to 1.7 mg/cm²/h with a final surface roughness of $R_a = 0.4 \text{ } \mu\text{m}$. A similar approach to improve the diamond surface was pursued by Kubota et al. [Kub16]. They investigated the potential of various tool materials in an H_2O_2 solution to smooth single crystal diamond. It was shown that, by adding H_2O_2 solution, nickel generates the highest material removal rate of 33.35 nm/h at room temperature, followed by iron with 4.29 nm/h, copper with 1.33 nm/h and 1.4301 steel with 1.28 nm/h. The best surface roughness (R_a) for all tool materials was very similar, in the range between 0.157 nm (copper) and 0.165 nm (steel).

All the studies described confirm that diamond wear with diamond polishing of flat surfaces is possible. The achievable removal rates of diamond and the surface qualities depend on the applied experimental parameters. Due to the experimental setup of the dynamic friction polishing, a micro-structuring of single and polycrystalline diamond is not possible. To overcome this restriction, Imoto et al. [Imo17] proposed a non-moving technique of thermo-chemical patterning, which used graphitization and diffusion of carbon atoms into the tool material. Therefore, they pressed a micro-structured nickel mold (1 mm × 1 mm) for 15 min at approximately 30 MPa and 60 MPa, respectively, against a single crystal diamond at a temperature of 800 °C. To avoid oxidation of the nickel mold, argon gas was pumped into the experimental chamber. The machined diamond surface showed a rough, rugged and tessellated texture [Imo17]. This surface texture was caused by the nickel mold, which creates a rugged surface texture during heating at 800 °C. The transferred depth of the micro-structures into the diamond surface was determined to be 20 nm (± 5 nm) and 83 nm (± 12 nm) at a pressure of 30 MPa and 60 MPa, respectively.

The authors compared mischmetal (composition in Table 4.9) and pure iron (99.5%) in a contact test with single crystal diamond at elevated temperatures [Bri09]. The motivation for this investigation was the higher solid solubility of carbon in mischmetal than in iron, as described by [Jin93]. Thus, if diamond material removal is limited by the solubility of carbon in the metal, higher solubility should produce a higher removal rate.

Table 4.9 Composition of mischmetal alloy as provided by the manufacturer

Element	Ce	La	Fe	Nd	Pr	Mg	Zn
mass%	40.3	23.6	20.0	10.2	3.3	1.97	<0.5

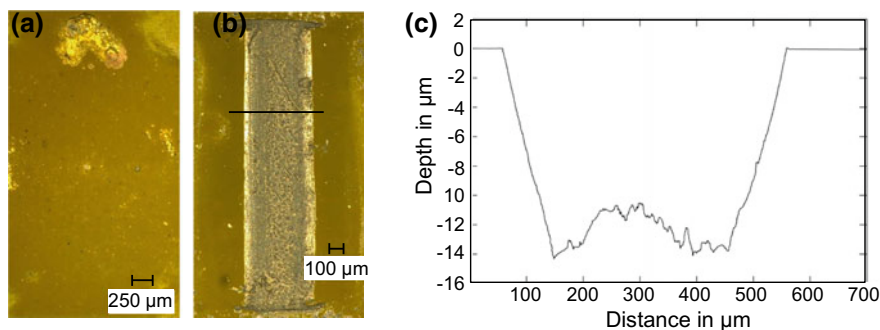


Fig. 4.73 Diamond surface after contact test with mischmetal at 750°C and 20 h (a) and iron at 850 °C and 5 h machining (b) and profile section of iron machined diamond (c) [Bri09]

It was found that mischmetal has no diamond removal effect for temperatures at 600 °C and holding times up to 24 h [Bri09]. Initial removal effects were determined at temperatures of 750 °C and holding times of 16 h or more. No removal of diamond material appeared over the complete contact area, and only certain locations on the diamond surface were etched. Contact tests with iron at 850 °C showed a diamond removal over the entire contact area with an increasing diamond removal as the holding time rose from 3 to 5 h. The authors showed that solid iron is a better catalyst material for defined shaping of single crystal diamond than mischmetal [Bri09] (Fig. 4.73).

4.7.2 Ultrasonic Assisted Friction Polishing

Previously performed investigations showed that machining of diamond with transition metals is possible. The methods used so far, i.e. dynamic friction polishing and non-moving thermo-chemical patterning, appear to be unsuitable processes due to the experimental setup or low diamond wear rates. To achieve higher diamond removal rates to shape complex diamond surfaces in a short time, the authors developed the technique of ultrasonic assisted friction polishing [Rob17a]. Therefore, a 20 kHz, 700 W ultrasonic generator was used to oscillate the metallic friction tool; a piezo ceramic converts the electrical voltage into a mechanical longitudinal vibration and the booster amplifies the amplitude. The friction tool was clamped in a non-amplifying sonotrode with an amplitude of about 8 μm in the z-direction. The machining setup is depicted in Fig. 4.74, which shows a schematic illustration (a) and the realized setup (b); for the machining, a single crystal diamond was fixed in a holder and pressed against the friction tool. The diamond holder was fixed on a dynamometer to control the force acting between the diamond and the friction tool. To prevent bending of the oscillating friction tool, a second diamond was fixed on the opposite side and pressed against the friction tool as a

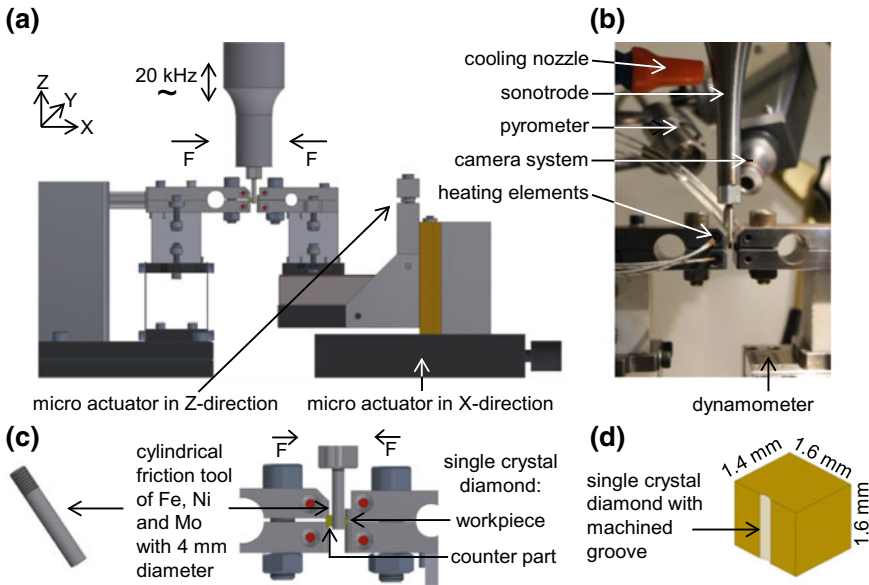


Fig. 4.74 Experimental setup of ultrasonic assisted friction polishing with pure metals: overall machining setup (a); realized setup (b); workpiece and tool engagement (c); machined single crystal diamond (d)

counterpart. In order to realize the required reaction temperature, heating elements were integrated in the holder close to the diamonds. The temperature of the machined diamond was determined by an optical pyrometer with a wavelength of $1.6 \mu\text{m}$. For this wavelength, single crystal diamond is almost fully transmissive and thus the temperature in the contact zone between the diamond and metal is measurable. The experiments were performed on synthetic single crystal diamonds of type Ib with dimensions of $1.6 \times 1.6 \times 1.4 \text{ mm}^3$ in the preferred (100) direction. As described above, the metal friction tool is used as the catalyst and the unbinding carbon from the diamond lattice can diffuse into the metal tool with the possibility of forming carbides, reacting with ambient oxygen to form CO and CO₂ or to transform into a graphite layer.

4.7.2.1 Diamond Removal by Ultrasonic Assisted Friction Polishing Using Pure Metals

The objective of the first part of this work was to determine the capability of the three different pure metals, iron (min. 99% Fe), nickel (min. 99% Ni) and molybdenum (min. 99% Mo) as catalyst materials, to increase the diamond removal rate. With respect to the formerly discussed theory from Paul et al. [Pau96], molybdenum has five, iron four and nickel two unpaired d-shell electrons. Experimental investigations were performed with a friction tool with 4 mm diameter which was pressed against the single crystal diamond during machining.

After machining, grooves with different removal depths could be detected. A schematic illustration is shown in Fig. 4.74.

Initially, the authors studied the influence of the different removal mechanisms: oxidation, diffusion and carbide forming, graphitization and possible mechanical abrasive diamond removal by the ultrasonic assisted friction polishing. To separate the effective diamond removal mechanism, a concept of varying experimental setups was developed as depicted in Fig. 4.75. By this concept, a separation of the effective diamond removal mechanisms and, therefore, a determination of the diamond removal caused by the mechanisms becomes possible. The basis of this concept is the ultrasonic assisted friction polishing process, which is carried out under atmosphere and in a high vacuum chamber. During polishing in atmosphere, all the diamond removal mechanisms (oxidation, diffusion and carbide forming, graphitization as well as mechanical diamond removal) are acting at the same time. When polishing in high vacuum, oxidation of cracked carbon atoms is prevented. To avoid a mechanical abrasive diamond removal, pure contact tests with non-moving contact parameters at elevated temperatures were performed.

The friction polishing experiments in atmosphere were conducted in a contact temperature range between 20 and 450 °C and in high vacuum between 20 and 300 °C. This means that the measured contact temperature during machining was kept constant. Due to the ultrasonically assisted friction tool, the contact temperature may increase lightning-fast for infinitely small areas; these localized temperatures are not detectable. Therefore a median temperature in the contact zone was measured. For each start of machining, the diamond was heated up externally

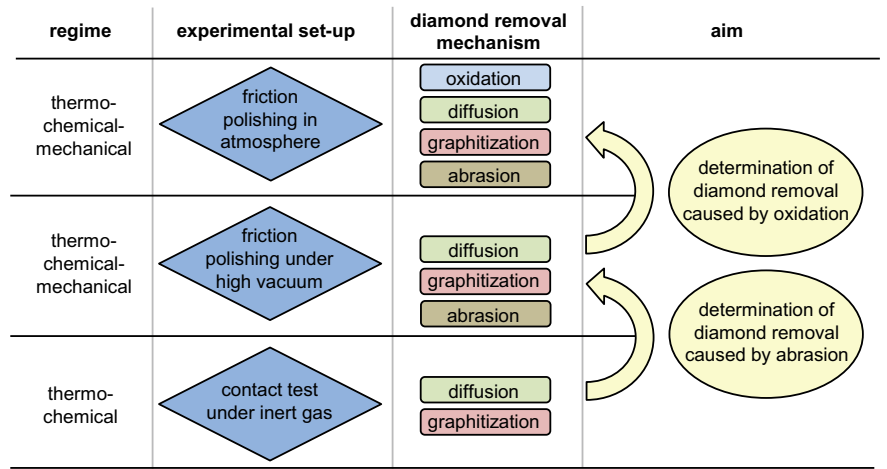


Fig. 4.75 Illustration of the experimental procedure for separating the diamond removal mechanism in machining of diamond

to the desired temperature and subsequently machined between 10 and 60 min with the moving friction tool. The contact load for all diamond removal tests with pure metals was kept at 5 N.

In addition, contact experiments were carried out in nitrogen atmosphere to avoid oxidation of carbon atoms in the heated chamber. During the contact tests, the diamond was fixed in a holder and a metal rod with 4 mm diameter was pressed against the diamond with a dead weight of 0.5 kg. Experiments were conducted in a temperature range between 600 and 850 °C with holding times between 0 and 60 min. Holding times of 0 min were used to determine the diamond removal which was achieved by solely heating and cooling the test sample. Diamond removal volumes without holding time were subtracted from each measurement with higher holding times and the same contact temperature.

After finishing all the machining experiments, the diamond was cleaned by etching with aqua regia at 100 °C for 60 min to dissolve residues from the diamond surface. Subsequently, a white light interferometer was used to measure the machined diamond surface; subsequently, the removed diamond volume at a length of 1 mm was evaluated by using SPIP software. The removed diamond volumes were plotted in 3-dimensional diagrams including a fit plane.

4.7.2.2 *Experimental Results*

Friction polishing experiments in ambient atmosphere with pure iron showed that, for all parameters, diamond removal was observed (Fig. 4.76). The removed diamond volume was measured between $6.18 \times 10^0 \mu\text{m}^3$ for 20 °C, 10 min, and $7.04 \times 10^6 \mu\text{m}^3$ for 450 °C, 50 min. These values lead to a median cavity depth of 0.25 μm and 19.76 μm , respectively. The results confirm the strong influence of the contact temperature. With rising temperature, the removed diamond volumes increased. Experiments without preheating showed the lowest diamond removal and a rough surface (condition A). With increasing temperature, the surface roughness decreased to a minimum (condition B) and rose with further increase of the contact temperatures (condition C). These different roughness values can be attributed to the varying regimes and varying diamond removal mechanisms, as well as the changing material properties of the friction tool condition for higher temperatures. Nevertheless, different mechanisms are acting in parallel. For experiments at lower contact temperature, the machined diamond shows a rutted surface with grooves in the direction of the vibration. In contrast to this, diamond surfaces machined at the contact temperature of 300 °C show a smooth surface with almost no surface fissuring. These results imply that at lower contact temperatures mechanically induced diamond wear takes place simultaneously with the thermo-chemical mechanism. The increasing surface roughness at elevated contact temperatures is due to the fact that the friction tool loses its mechanical strength. As a result, surface disruption occurred and the diamond surface mirrored the deteriorated surface of the tool. Further significant data points for iron as the tool material are summarized in Table 4.10 and will be discussed in the following.

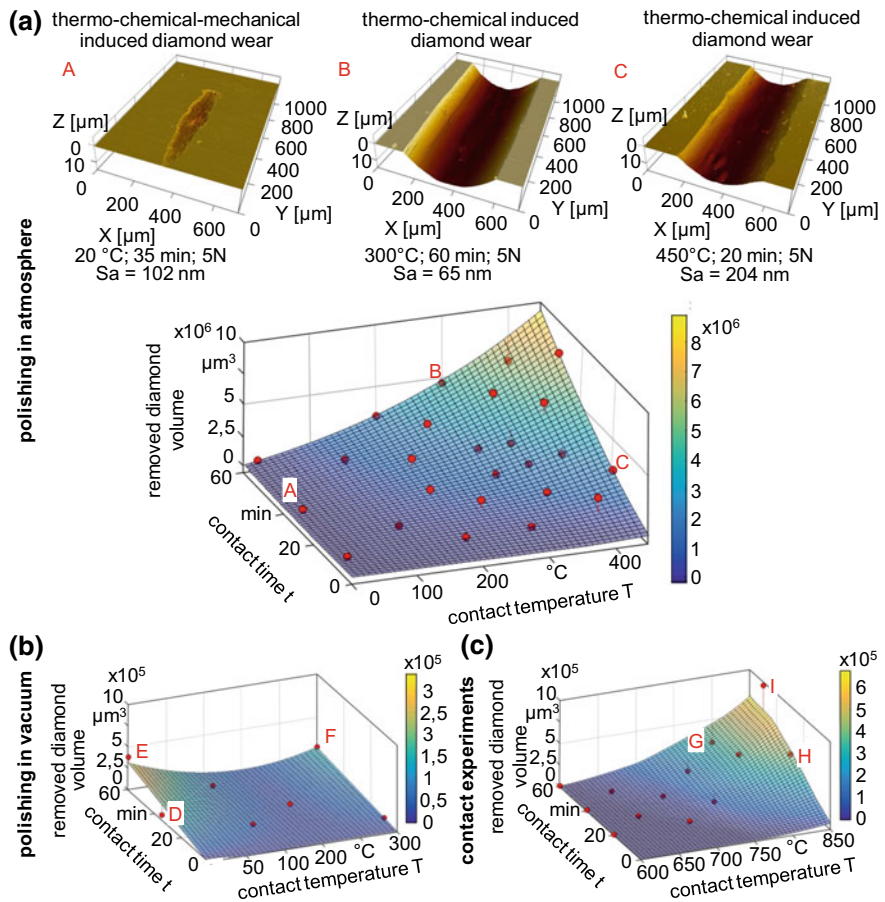


Fig. 4.76 Machined diamond surfaces after polishing in atmosphere and diamond removal diagram for polishing in atmosphere (a), polishing in high vacuum (b) as well as for contact test with pure iron (c)

Table 4.10 Significant data points with iron as tool material for different experimental setups and machining conditions

	Polishing in atmosphere			Polishing in high vacuum			Contact test		
Machining condition	A	B	C	D	E	F	G	H	I
Contact temperature [°C]	20	300	450	20	20	300	800	850	850
Contact time [min]	35	60	50	35	60	60	60	30	60
Surface roughness [nm]	102	65	204	82	196	68	1751	621	1004
Diamond removal $\times 10^6$ [μm^3]	2.72	4.26	7.04	0.05	0.04	0.14	0.22	0.43	0.93

Table 4.11 Diamond removal rates for polishing in atmosphere with iron as tool material

Contact temperature [°C]	200	300	400
Contact time [min]	10/30/40/60	10/30/40/60	10/30/40/60
Diamond removal rate [μm ³ /min/μm ²]	141/127/127/103	186/156/134/151	456/206/251/179

To analyze the effect of possible carbon diffusion into the tool material, the diamond removal rates were studied for experiments with contact temperatures of 200, 300 and 400 °C for machining times of 10, 30, 40 and 60 min (Table 4.11). To achieve comparable results for all contact temperatures, the diamond removal rates were related to 1 μm² of the machined diamond area. The experiments showed that the diamond removal rate after 10 min machining time is the highest for all contact temperatures compared to longer machining times.

With increasing machining time, the removal rate decreased slightly to similar diamond removal rates (Table 4.11). The slightly higher diamond removal rates for short machining times can be attributed to the cylindrical shape of the friction tool. At the beginning of the machining, the cylindrical friction tool is pressed against the diamond in line contact, which results in a higher contact load. After a short time, the tool is slightly flattened and the contact load decreases compared to the contact load with longer machining times. For experiments with a contact temperature of 400 °C, the diamond removal rates showed a much higher variability. Longer machining times showed no significant influence of the diamond removal rate, which is an indication that diffusion of carbon atoms into the tool material is negligible. For further proof, a metallurgical element analysis was carried out to identify the raised carbon content in the subsurface of the friction tool. For the analysis, a friction tool which was used at 300 °C and 60 min was chosen. The tool was cut and 10,000 measurements in an area of 0.5 mm × 0.1 mm from the contact zone into the tool material were taken as the depth profile. The investigation found no carbon atoms in the tool material, which underlines that diffusion is insignificant.

To investigate the influence of oxygen, polishing experiments were carried out in a high vacuum condition with 1×10^{-6} Pa and contact temperatures between 20 and 300 °C. Higher contact temperatures led to breakouts on the diamond surface, starting at the edge. In contrast to the experiments in atmosphere, the highest diamond removal was identified for machining conditions D and E without pre-heating. The removed diamond volume was two times higher than the diamond removal in atmosphere. Preheating of the diamond to contact temperatures reduced the diamond removal. With a further rise to 300 °C, the diamond removal increased again and the formation of graphite on the diamond surface was detected by Raman analysis, which is shown in Fig. 4.77. For lower contact temperature, the formation of graphite could not be detected.

In addition to polishing experiments, contact tests in a nitrogen atmosphere were conducted to analyze the possibility of diamond removal by graphitization and diffusion. The experiments were conducted at contact temperatures between 600 and 850 °C. Experiments with lower contact temperatures showed no (600 °C) or a

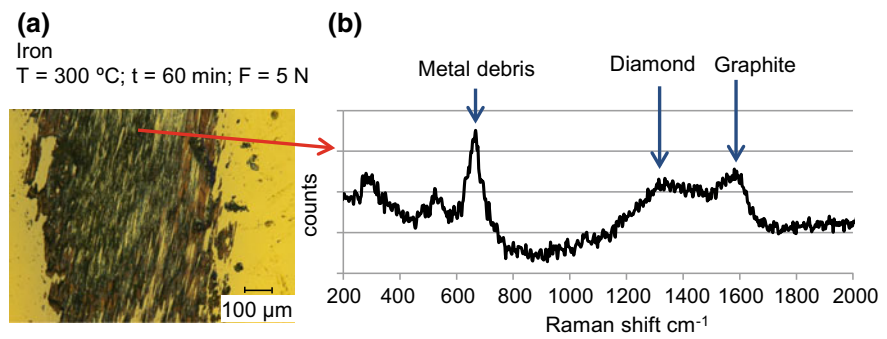


Fig. 4.77 Polished diamond surface in high vacuum (a) and Raman analysis (b)

very low (650°C) diamond removal. With increasing contact temperature up to 800 °C, the diamond removal increased steadily. Contact tests at a temperature of 800 °C (condition G) showed a lower diamond removal compared to vacuum experiments with a highest contact temperature of 300 °C (condition F). When increasing the contact temperature up to 850 °C, the diamond removal increased significantly. These results reveal that the formation of CO and CO₂ is the significant mechanism for ultrasonic assisted polishing of single crystal diamond in contact with pure iron. Experiments in atmosphere show up to 30 times higher diamond removal rates compared to experiments in high vacuum. With increased contact temperatures, the formation of graphite has a more relevant role under the elimination of oxygen. Lower contact temperatures in ambient atmosphere and in high vacuum lead to a strong abrasive diamond removal (Table 4.12).

In further experiments, nickel was used as the tool material for friction polishing at ambient atmosphere (Fig. 4.78). The removed diamond volume was measured between $3.63 \times 10^4 \mu\text{m}^3$ for 20 °C, 10 min and $3.25 \times 10^6 \mu\text{m}^3$ for 300 °C, 60 min. These parameters led to a median cavity depth of 0.75 µm and 8.25 µm, respectively.

In contrast to experiments without preheating and with iron as the tool material, nickel showed an almost nine times higher removed diamond volume (condition A). With rise of the preheating temperature and time, the removed diamond volume increases to the maximum at condition B and decreases slightly with a further rise of

Table 4.12 Significant data points with nickel as tool material for different experimental setups and machining conditions

Machining condition	Polishing in atmosphere			Polishing in high vacuum			Contact test		
	A	B	C	D	E	F	G	H	I
Contact temperature [°C]	20	300	450	20	200	300	750	850	850
Contact time [min]	35	60	50	35	60	60	50	30	60
Surface roughness [nm]	505	109	2344	127	106	/	153	240	239
Diamond removal x10 ⁶ [µm ³]	0.23	3.25	2.98	0.18	0.10	0.01	0.01	0.06	0.07

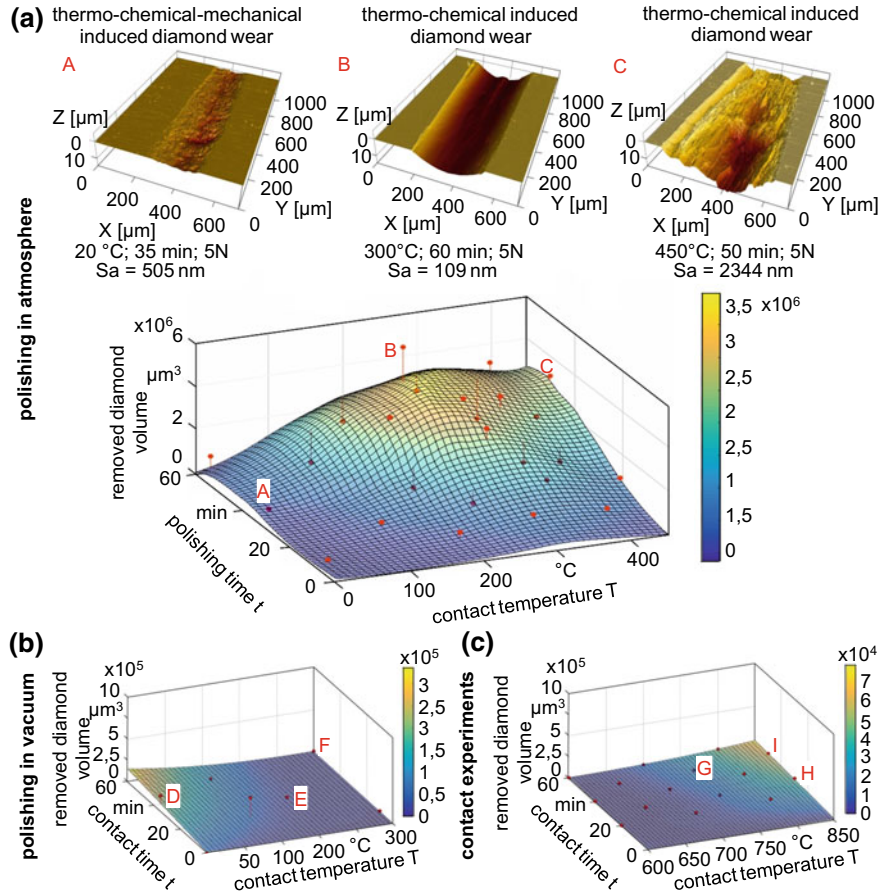


Fig. 4.78 Diamond removal for polishing in atmosphere (a), polishing in high vacuum (b) and for contact test (c) with pure nickel as well as machined diamond surfaces after polishing in atmosphere

preheating (condition C). The reduction of the ability to remove diamond is probably caused by the formation of nickel oxides. Experiments without preheating showed a rough surface and declined strongly with increasing temperature to a minimum at condition B. A strong rutted diamond surface was identified for condition C. Compared to the experiments with iron, nickel led to a higher diamond surface roughness after machining. For all the investigated contact temperatures, the diamond removal rates identified show a similar curved shape. For shorter machining times (10 min), the diamond removal rates showed high values. With increase of the machining time to 60 min the diamond removal rates decrease significantly for all the contact temperatures used. This means that nickel quickly loses the capability to remove diamond (Table 4.13).

Table 4.13 Diamond removal rates at polishing in atmosphere with nickel as tool material

Contact temperature [°C]	200	300	400
Contact time [min]	10/30/40/60	10/30/40/60	10/30/40/60
Diamond removal rate [μm ³ /min/μm ²]	227/106/124/72	285/244/201/127	212/113/147/120

In addition to friction polishing experiments at ambient atmosphere, the ability of nickel to remove diamond in the absence of oxygen in a high vacuum was investigated in a temperature range between 20 and 300 °C. Similar to experiments with iron, the removed diamond volume decreased substantially with increasing preheating temperature (Fig. 4.78b). The contact test for experiments with a contact temperature of 600 °C revealed a negligible removed diamond volume (Fig. 4.78c). With increased contact temperature, the removed volume increased slightly to $0.0125 \times 10^6 \mu\text{m}^3$ for condition G, which is eight times lower than the equivalent experiments with iron ($0.0926 \times 10^6 \mu\text{m}^3$). A rise of contact temperature up to 850 °C (conditions H and I) increased the removed diamond volume further. Overall, the diamond removal for nickel is about one order of magnitude lower than for iron (Table 4.13).

Friction polishing experiments at ambient atmosphere with molybdenum revealed the lowest capability to machine diamond (Fig. 4.79 and Table 4.15). Experiments without preheating exhibited no diamond removal at all. With increasing preheating temperature, the removed diamond volume increased slightly to a maximum at condition C, which is more than 20 times lower than the results obtained from the use of iron. The maximum diamond removal rates were identified for the shortest machining time of 10 min. With higher preheating temperatures, the diamond removal rates decreased for all the contact temperatures used. Furthermore, the removed diamond volumes exhibited a strong dependence on the contact temperature and machining time and showed for all parameters strong grooves aligned in the direction of vibration. The surface roughness was measured with $S_a = 104 \text{ nm}$ (condition A) and increased with rising preheating temperature to 551 nm (condition C). Higher contact temperatures did not lead to an increase of the surface roughness (Table 4.14).

Table 4.14 Significant data points with molybdenum as tool material for different experimental setups and machining conditions

Machining condition	Polishing in atmosphere			Polishing in high vacuum		
	A	B	C	D	E	F
Contact temperature [°C]	125	200	450	20	200	300
Contact time [min]	50	30	50	35	30	60
Surface roughness [nm]	104	305	551	190	202	351
Diamond removal $\times 10^6 [\mu\text{m}^3]$	0.02	0.04	0.31	0.19	0.18	0.33

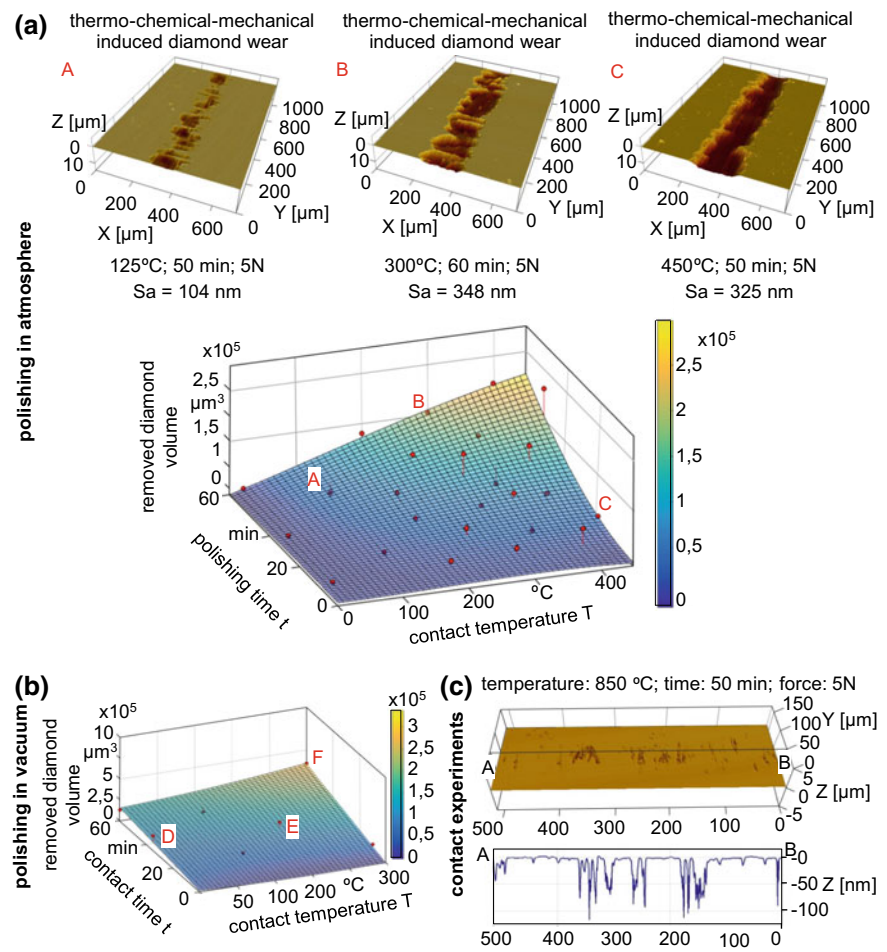


Fig. 4.79 Diamond removal for polishing in atmosphere (a) and polishing in high vacuum (b) with pure molybdenum. Diamond surface and profile after molybdenum contact test (c) with holding temperature of 850 °C and holding time of 60 min

Table 4.15 Diamond removal rates for polishing in atmosphere with molybdenum as tool material

Contact temperature [°C]	200	300	400
Contact time [min]	10/30/40/60	10/30/40/60	10/30/40/60
Diamond removal rate [$\mu\text{m}^3/\text{min}/\mu\text{m}^2$]	26/22/20/14	38/16/40/19	50/15/27/27

In contrast to the experiments at ambient atmosphere (Table 4.15), molybdenum showed a high removed diamond volume in high vacuum. The contact test with molybdenum showed no effect on the diamond surface. Only for the highest contact temperature of 850 °C and the longest holding time of 50 min a nearly negligible amount of removed diamond volume was detected with a maximum cavity depth of 112 nm.

These results exhibit that oxygen and diamond graphitization do not play a dominant role in removing diamond in a lower temperature range. Only in a higher temperature range oxygen does play a significant role. At lower temperature zones mechanically induced diamond wear is the key factor.

4.7.3 **Micro-Structuring of Single Crystal Diamond Using Ultrasonic Assisted Friction Polishing**

The second part of this report addresses the capability of the ultrasonic assisted friction polishing process to micro-structure single crystal diamond for linear [Rob17b] and circular [Rob17c] polishing. Therefore, 1.4310 steel was used as a favorable tool material due to its high hardness, higher elevated temperature strength and better machinability against pure metals. The composition of the stainless steel 1.4310 is shown in Table 4.16.

Ultrasonic assisted friction polishing tests were carried out to investigate the capability of steel 1.4310 to remove diamond in the same procedure as described above for pure metals. Experiments were conducted with contact temperatures in a range of 200 to 400 °C with a machining time between 20 and 120 min and a contact load of 5 N. Additionally, diamond removal experiments were carried out with contact loads of 2 N, 5 N, 8 N, 12.5 N and 25 N to investigate the influence of the contact load. These experiments were performed at contact temperatures of 125, 200, 300 and 400 °C and a machining time of 40 min.

4.7.3.1 *Experimental Results*

Diamond removal tests in contact with steel 1.4310 showed similar results as for the experiments on pure iron. Figure 4.80 shows that the diamond removal is strongly dependent on the temperature and time. The maximum volume of removed diamond was identified for condition C. In addition to a predictable removed diamond

Table 4.16 Composition of stainless steel 1.4310 (data provided by supplier)

Element	C	Si	Mn	P	S	Cr	Mo	N	Ni
Min mass%	0.05	–	–	–	–	16.00	–	–	6.00
Max mass%	0.15	2.00	2.00	0.045	0.015	19.00	0.80	0.110	9.50

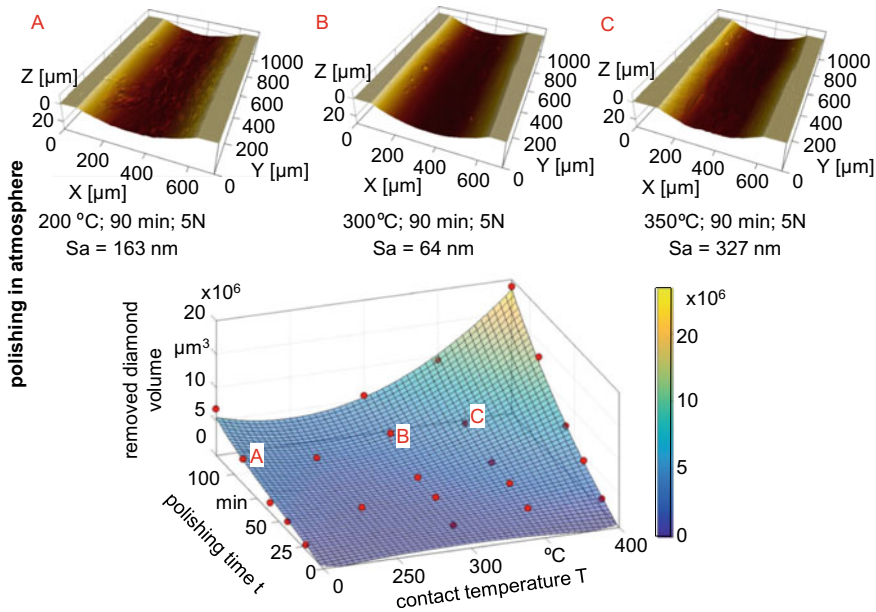


Fig. 4.80 Diamond removal for polishing in atmosphere with steel 1.4310

volume, knowledge of the minimum diamond surface roughness was important to use efficient parameters to micro-structure single crystal diamond. The minimum surface roughness was detected in the temperature range between 250 and 300 °C with the lowest surface roughness at condition B.

In addition to the contact temperature and machining time, the contact load plays an important role in micro-structuring single crystal diamond. To identify the influence of the contact load on the removed diamond volume and surface roughness, experiments with five different contact loads (2 N, 5 N, 8 N, 12.5 N, 25 N) were conducted.

Figure 4.81 shows that the removed diamond volume is strongly dependent on the contact load. In the temperature range between 125 and 300 °C, the removed diamond volume increased slowly with the increasing contact temperature, apart from the experiments with 25 N. With an increase of the preheating temperature to 400 °C, the removed diamond volume increased to around $4.2 \times 10^6 \mu\text{m}^3$ for all the contact loads used (except for 25 N). Experiments with a contact load of 2 N and 5 N showed the lowest surface roughness with $S_a = 45 \text{ nm}$ (200 °C) and 52 nm (300 °C), respectively. At the high pressure of 25 N, the friction tool lost its strength and a very rough diamond surface with $S_a = 603 \text{ nm}$ was generated.

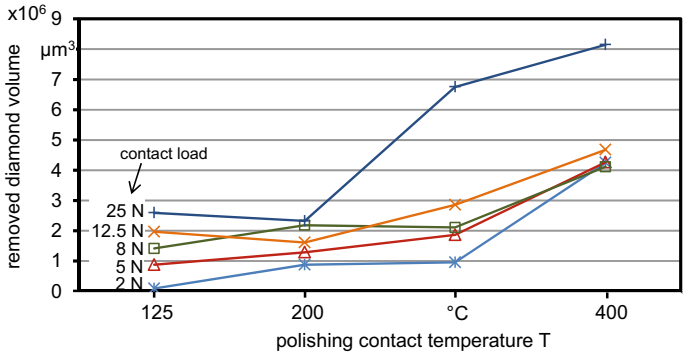


Fig. 4.81 Diamond removal depending on contact load and contact temperature by polishing with steel 1.4310 as tool material

4.7.3.2 Setup for Micro-Structuring Single Crystal Diamond

To micro-structure single crystal diamond, the shape of the friction tool was changed. The transformed tool featured two flat and parallel sides, where one side exhibited a small pin of $1 \times 1 \times 1 \text{ mm}^3$. The parallel exterior side of the pin, which was perpendicular to the centerline of the friction tool, was micro-structured by micro milling. The experimental setup is shown in Fig. 4.82.

Two different kinds of micro-structure, convex and concave, were chosen as shown in Fig. 4.83 (left column a–d). Figure 4.83a represents a linear convex micro-structure of $600 \mu\text{m} \times 200 \mu\text{m} \times 120 \mu\text{m}$ (length, width, height) which is aligned in the direction of the vibration. The friction tool with a concave micro-structure possesses the same parameters and is shown in Fig. 4.83b. To characterize a “smear effect” based on the tool motion during the ultrasonic assisted friction polishing, an L-shaped structure was chosen (Fig. 4.83c and d) with the same dimensions. With respect to the polishing and contact load experiments, a preheating temperature of $250 \text{ }^{\circ}\text{C}$, a machining time of 120 min and a contact load of 4 N for the concave and 2 N for the convex micro-structured friction tools was chosen.

The experimental results exhibit for all four micro-structures the possibility of shaping single crystal diamond by ultrasonic assisted friction polishing (Fig. 4.83

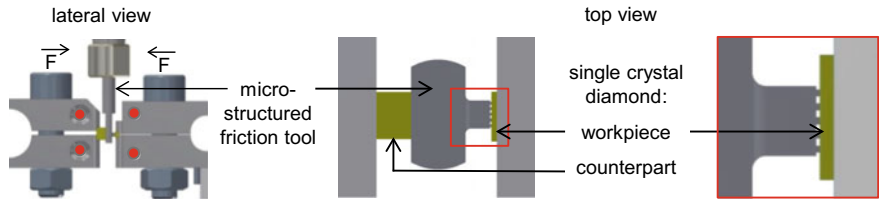


Fig. 4.82 Experimental setup of ultrasonic assisted friction polishing for micro-structuring single crystal diamond

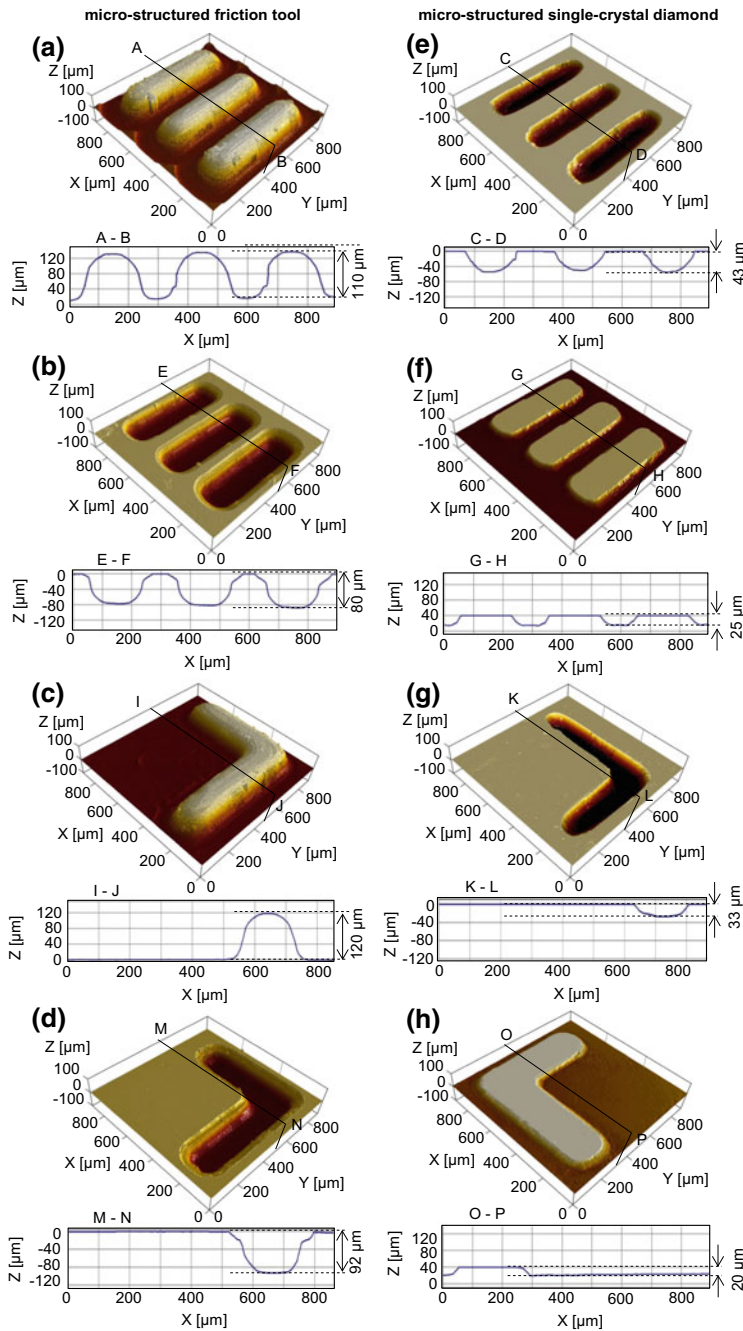


Fig. 4.83 Micro-structured friction tool **a–d** and micro-structured single crystal diamond **e–h**

right column e–h). It can be seen that the shape of the transferred micro-structure on the top of the diamond has sharp edges and has the same dimensions as the friction tool. This confirms that the micro-structure is transferred accurately into the diamond and the micro-structured friction tool can keep the geometry during processing. Convex micro-structured diamond surfaces show a deeper micro-structure ($43\text{ }\mu\text{m} + 33\text{ }\mu\text{m}$) than concave micro-structured diamond surfaces ($25\text{ }\mu\text{m} + 20\text{ }\mu\text{m}$). This result is based on a better oxygen feed to the convex micro-structured friction tool than to the concave micro-structured friction tool with a plane surface which has a tight contact with the diamond surface.

References

- [Alt06] Altintas, Y.: *Manufacturing Automation: Metal Cutting Mechanics, Machine Tool Vibrations, and CNC Design*. Cambridge University Press (2006)
- [Ara08] Aramcharoen, A., Mativengaa, P.T., Yangb, S., Cookeb, K.E., Teerb, D.G.: Evaluation and selection of hard coatings for micro milling of hardened tool steel. *Int. J. Mach. Tools Manuf.* **48**(14), 1578–1584 (2008)
- [Ara09] Aramcharoen, A., Mativenga, P.T.: Size effect and tool geometry in micromilling of tool steel. *Precis. Eng.* **33**(4), 402–407 (2009)
- [Ass02] Asmussen, J., Reinhard, D.K. (eds.): *Diamond Films Handbook*. Marcel Dekker, New York Basel (2002). ISBN: 978-0824795771
- [Bae11] Bäuerle, D.: *Laser Processing and Chemistry*. Springer, Heidelberg, p. 482 (2011)
- [Beh15] Behrens, G., Ruhe M., Tetzl, H., Vollertsen F.: Effect of tool geometry variations on the punch force in micro-deep drawing of rectangular components. *Product. Eng. Res. Dev.* **9**, 195–201 (2015)
- [Ber99] Bertsekas, D.P.: *Nonlinear Programming*, 2nd edn. Athena Scientific (1999)
- [Bhu04] Bhushan, B., Nosonovsky, M.: Comprehensive model for scale effects in friction due to adhesion and two- and three-body deformation (plowing). *Acta Mater.* **52**, 2461–2474 (2004)
- [Blu03] Blunt, L., Jiang, X. (eds.): *Advanced techniques for assessment surface topography: development of a basis for 3D surface texture standards “surfstand”*. Kogan page science (2003)
- [Bob08] Bobe, U.: *Die Reinigbarkeit technischer Oberflächen im immmergierten System*. Univ. Diss., München, Deutschland: Technische Universität München (2008)
- [Böh14] Böhmermann, F., Preuß, W., Riemer, O.: Manufacture and functional testing of micro forming tools with well-defined tribological properties. In: *Proceedings of the 29th ASPE Annual Meeting*, vol. 29, pp. 486–491 (2014)
- [Böh16] Böhmermann, F., Riemer, O.: Tribological Performance of Textured Micro Forming Dies, *Dry Metal Forming OAJ FMT 2*, pp. 67–71 (2016)
- [Böh18] Böhmermann, F., Riemer, O.: Methodology for reliable tribological investigations applying a micro tribometer in ball-on-plate configuration. In: *Proceedings of the 5th International Conference on New Forming Technology (ICNFT)*, MATEC Web of Conferences, vol. 190, pp. 15011-1–15011-6 (2018)
- [Boy14] Boyd, S., Vandenberghe, L.: *Convex Optimization*. Hrsgs. Cambridge Press (2014)

- [Bra12] Brandt, C.: Regularization of Inverse Problems for Turning Processes. Dissertationsschrift, Universität Bremen, Logos Verlag (2013)
- [Bri09] Brinksmeier, E., Klopfsstein, M.J.: Thermochemical material removal of diamond by solid iron and mischmetal. *Product. Eng.* **3**(3), 225–229 (2009)
- [Bri10] Brinksmeier, E., Riemer O., Twardy S.: Tribological behavior of micro-structured surfaces for micro-forming tools. *Int. J. Mach. Tools Manuf.* **50**(4), 425–430 (2010)
- [Bun96] Bundy, A.P., Basset, W.A., Weathers, M.S., Hemley, R.J., Mao, H.K., Goncharov, A.F.: The pressure-temperature phase and transformation diagram for carbon; updated through 1994. *Carbon* **34**(2), 141–153 (1996)
- [But03] Butt, H.-J., Graf, K., Kappel, M.: *Physics and Chemistry of Interfaces*. Wiley-VCH, Weinheim (2003)
- [Cam12] Camara, M.A., Rubio, J.C., Abrao, A.M., Davim, J.P.: State of the art on micromilling of materials: a review. *J. Mater. Sci. Technol.* **28**, 673–685 (2012)
- [Cas12] Casella, G., Berger, R.L.: *Statistical Inference*. China Machine Press (2012)
- [Che09] Chen, Y., Zhang, L.-C.: Polishing of polycrystalline diamond by the technique of dynamic friction, part 4: Establishing the polishing map. *Int. J. Mach. Tools Manuf.* **49**(3–4), 309–314 (2009)
- [Che10] Cheng, K., Huo, D., Wardle, F.: Design of a five-axis ultra-precision micromilling machine-UltraMill. Part 1: holistic design approach, design considerations and specifications. *Int. J. Adv. Manuf. Technol.* **47**(9), 867–877 (2010)
- [Che13] Chen, Y., Zhang, L.-C.: *Polishing of Diamond Materials*. Springer Verlag London (2013). ISBN: 978-1-84996-407-4
- [Czi10] Czichos, H., Habig, K.H.: *Tribologie-Handbuch-Tribometrie, Tribomaterialien, Tribotechnik*. Vieweg + Teubner Verlag (2010)
- [Dat87] Datta, M., Romankiw, L.T., Vigliotti, D.R., von Gutfeld, R.J.: Laser etching of metals in neutral salt solutions. *Appl. Phys. Lett.* **24** (1987)
- [Den14] Denkena, B., Vehmeyer, J., Niederwestberg, D., Maaß, P.: Identification of the specific cutting force for geometrically defined cutting edges and varying cutting conditions. *Int. J. Mach. Tools Manuf.* **82**, 42–49 (2014)
- [Dow04] Dow, T.A., Miller, E.L., Garrard, K.: Tool force and deflection compensation for small milling tools. *Precis. Eng.* **28**, 31–45 (2004)
- [Eck17a] Eckert, S., Köhnsen, A., Vollertsen, F.: Surface finish using laser-thermochemical machining. In: *Proceedings of the Laser in Manufacturing Conference LIM 2017*, pp. 1–8 (2017)
- [Eck17b] Eckert, S.; Messaoudi, H.; Mehrafsun, S.; Vollertsen, F.: Laser-thermochemical induced micro-structures on titanium. *Journal of Materials Science and Surface Engineering* **5**(7), (2017) 685–691, doi:10.1016/j.jmsse/2348-8956/5-7.3
- [Eck18] Eckert, S., Vollertsen, F.: Mechanisms and processing limits of surface finish using laser-thermochemical polishing. *CIRP Ann. Manuf. Technol.* **67**(1), 201–204 (2018). <https://doi.org/10.1016/j.cirp.2018.04.098>
- [Flo13] Flosky, H.; Vollertsen, F.: Wear behavior of a micro blanking and deep drawing tool combination with different drawing ratio. In: *IDDRG 2013 Conference*, Zurich (2013)
- [Flo14a] Flosky, H., Veenas, S., Feuerhahn, F., Hartmann, M., Vollertsen, F.: Flaking during a micro blanking and deep drawing process. In: *Proceedings of the 9th International Conference on Micro Manufacturing (ICOMM2014)*, Bremen (2014)
- [Flo14b] Flosky, F.; Vollertsen, F.: Wear behavior in a combined micro blanking and deep drawing process. *CIRP Ann. Manuf. Technol.* **63**, 281–284 (2014)
- [Flo14c] Flosky, H., Krüger, M., Vollertsen F.: Temperature measurement with thermocouples during micro deep drawing process. In: *Proceedings of the 4th International Conference on Nanomanufacturing (nanoMan2014)* (2014)

- [Flo15] Flosky, H., Krüger, M., Vollertsen, F.: Verschleißmessung in der Mikroumformung mittels Silikonabformverfahren an einem kombinierten Schneid-Ziehring. In: Tagungsband 7. Kolloquium Mikroproduktion. Aachen (2015)
- [Flo16] Flosky, H., Feuerhahn, F., Böhmermann, F., Riemer, O., Vollertsen, F.: Performance of a micro deep drawing die manufactured by selective laser melting. In: Proceedings of the 5th International Conference on Nanomanufacturing (nanoMan2016), Macau, China (2016)
- [Gar18a] N.N.: Gartner says smartphone sales surpassed one billion units in 2014. <https://www.gartner.com/newsroom/id/2996817>. Accessed 18 Apr 2018
- [Gar18b] N.N.: Gartner says worldwide sales of smartphones recorded first ever decline during the fourth quarter of 2017. <https://www.gartner.com/newsroom/id/3859963>. Accessed 18 Apr 2018
- [Gei01] Geiger, M., Kleiner, M., Eckstein, R., Tiesler, N., Engel, U.: Microforming. CIRP Ann. Manuf. Technol. **50**, 445–462 (2001)
- [Gei97] Geiger, M., Engel, U., Pfestorf, M.: New developments for the qualification of technical surfaces in forming processes. Ann. CIRP **46**(1), 171–174 (1997)
- [Geo03] McGeough, J.A., Pajak, P.T., De Silva, A.K.M., Harrison, D.K.: Recent research & developments in electrochemical machining. Int. J. Electr. Mach. **8**, 1–14 (2003)
- [Goc08] Goch, G., Lübke, K.: Tschebyscheff approximation for the calculation of maximum inscribed/minimum circumscribed geometry elements and form deviations. CIRP Ann. Manuf. Technol. **57**(1), 517–520 (2008)
- [Gre66] Greenwood, J.A., Williamson, J.B.P.: Contact of nominally flat surfaces. Proc. R. Soc. A **295**(1442) 300–319 (1966)
- [Gup16] Gupta, K., Neelesh, K.J., Laubscher, R.F.: Electrochemical hybrid machining processes. In: Hybrid Machining Processes. Springer Briefs in Applied Sciences and Technology, pp. 9–32. Springer, Cham (2016). https://doi.org/10.1007/978-3-319-25922-2_2
- [Gut86] Gutfeld von, R.J.: Laser-enhanced plating and etching for microelectronic applications. IEEE Circuits Devices Mag. **2**(1), 57–60 (1986)
- [Han16] Han, W., Kunieda, M.: Influence of machining conditions on machining characteristics of micro-rods by micro-ECM with electrostatic induction feeding method. In: Proceedings of the 18th CIRP Conference on Electro Physical and Chemical Machining (ISEM XVIII), Procedia CIRP **42**, pp. 819–824 (2016)
- [Hau15] Hauser, O., Mehrafsun, S., Vollertsen, F.: Einfluss der Abtragsbahnfolge auf die resultierende Geometrie bei der laserchemischen Bearbeitung von Stellite 21. In: Hopmann, Ch., Brecher, Ch., Dietzel, A., Drummer, D., Hanemann, T., Manske, E., Schomburg, W.K., Schulze, V., Ullrich, H., Vollertsen, F., Wulfsberg, J.-P. (eds.) Tagungsband 7. Kolloquium Mikroproduktion, IKV Aachen, pp. 8–14 (2015). ISBN: 978-3-00-050-755-7
- [Hau15] Hauser, O., Mehrafsun, S., Vollertsen, F.: Electrolytes for sustainable laser-chemical machining of titanium, Stellite 21 and tool steel X110CrMoV8-2. Appl. Mech. Mater. **794**, 262–269 (2015)
- [Hau15a] Hauser, O., Mehrafsun, S., Vollertsen, F.: Electrolytes for sustainable laser-chemical machining of titanium, Stellite 21 and tool steel X110CrMoV8-2. In: Wulfsberg, J.P., Röhlig, B., Montag, T. (eds.) Progress in Production Engineering, WGP Kongress (2015). TransTech Publications Pfaffikon/CH, pp. 262–269 (2015)
- [Hu10] Hu, Z., Huferath-von Luepke, S., von Kopylow, C., Vollertsen, F.: Characteristics of wear behavior of micro deep drawing tools. In: International Conference on Advances in Materials and Processing Technologies (AMPT2010), pp. 335–340 (2011)
- [Hu11a] Hu, Z.; Vollertsen, F.: Auslegung von Mikrotiefziehwerkzeugen zur Bestimmung der Werkzeuglebensdauer. In: 5. Kolloquium Mikroproduktion, Karlsruhe (2011)
- [Hu11b] Hu, Z., Wielage, H., Vollertsen, F.: Economic micro forming using DLC- and TiN-coated tools. J. Plast. (JTP) **51**–57 (2011)
- [Hu12] Hu, Z., Schubnov, A., Vollertsen, F.: Tribological behavior of DLC-films and their application in micro deep drawing. J. Mater. Process. Technol. **212**, 685–688 (2012)

- [Imo17] Imoto, Y., Yan, J.: Thermochemical micro imprinting of single-crystal diamond surface using a nickel mold under high-pressure conditions. *Appl. Surf. Sci.* **404**, 318–325 (2017)
- [Jin12] Jin, B., Maass, P.: Sparsity regularization for parameter identification problems. *Inverse Probl.* **28**(12), 23001 (2012)
- [Jin93] Jin, S., Chen, L., Graebner, J., McCormack, M., Reiss, M.: Thermal conductivity in molten-metal-etched diamond films. *Appl. Phys. Lett.* **63**(5), 622–624 (1993)
- [Jus07] Justinger, H., Hirt, G.: Scaling effects in the miniaturization of deep drawing process. In: *International Conference on New Forming Technology (2nd ICNFT07)*, pp. 167–176 (2007)
- [Kim03] Kim, G.M., Kim, B.H., Chu, C.N.: Estimation of cutter deflection and form error in ball-end milling processes. *Int. J. Mach. Tools Manuf.* **43**, 917–924 (2003)
- [Klo13] Klocke, F., Zeis, M., Klink, A., Veselovac, D.: Technological and economical comparison of roughing strategies via milling, EDM and ECM for titanium- and nickel-based blisks. In: *Proceedings of the 1st CIRP Global Web Conference on Interdisciplinary Research in Production Engineering, Procedia CIRP 2*, pp. 98–101 (2013)
- [Kra08] Kray, D., Fell, A., Hopman, S., Mayer, K., Willeke, G.P., Glunz, S.W.: Laser Chemical Processing (LCP)—a versatile tool for microstructuring applications. *Phys. A* **93**, 99–103 (2008)
- [Kub16] Kubota, A., Shin, N., Touge, M.: Improvement of material removal rate of single-crystal diamond by polishing using H_2O_2 solution. *Diam. Relat. Mater.* **70**, 39–45 (2016)
- [Kwo12] Kwon, H., Baek, W.-K., Kim, M.-S., Shin, W.-S., Yoh, J.J.: Temperature-dependent absorbance of painted aluminum, stainless steel 304, and titanium for 1.07 μm and 10.6 μm laser beams. *Opt. Lasers Eng.* **50**, 114–121 (2012)
- [Lea13] Leach, R. (ed.): *Characterisation of Areal Surface Texture*. Springer (2013)
- [Lech09] Lechleiter, A., Rieder, A.: *Towards a General Convergence Theory for Inexact Newton Regularization*. Springer (2009)
- [Lou01] Louis, A.: *Inverse und schlecht gestellte Probleme*. Hrsgs. Teubner, Stuttgart (2001)
- [Lüb12] Lübke, K., Sun, Z., Goch, G.: Three-dimensional holistic approximation of measured points combined with an automatic separation algorithm. *CIRP Ann. Manuf. Technol.* **61**(1), 499–502 (2012)
- [Man08] Manabe, K., Shimizu, H., Koyama, H., Yang, M., Ito, K.: Validation of FE simulation based on surface roughness model in micro-deep drawing. *J. Mater. Process. Technol.* **204**, 89–93 (2008)
- [Meh12] Mehrafsun, S., Stephen, A., Vollertsen, F.: Comparison of laser-thermal and laser-chemical machining. In: Fang, F., Kuriyagawa, T. (eds.) *3rd International Conference on Nanomanufacturing (nanoMan2012)*, July 25–27. Wako, Saitama, Japan (2012)
- [Meh13] Mehrafsun, S., Vollertsen, F.: Disturbance of material removal in laser-chemical machining by emerging gas. *CIRP Ann.* **62**(1), 195–198 (2013)
- [Meh16a] Mehrafsun, S., Harst, S., Hauser, O., Eckert, S., Klink, A., Klocke, F., Vollertsen, F.: Energy-based analysis of material dissolution behavior for laser-chemical and electrochemical machining. In: *3rd CIRP Conference on Surface Integrity (CIRP CSI)*. *Procedia CIRP* **45**, pp. 347–350 (2016)
- [Meh16b] Mehrafsun, S., Messaoudi, H., Vollertsen, F.: Influence of material and surface roughness on gas bubble formation and adhesion in laser-chemical machining. In: *Proceedings of the 5th International Conference on Nanomanufacturing (nanoMan 2016)*, pp. 1–10 (2016)
- [Meh18] Mehrafsun, S., Messaoudi, H.: Dynamic process behavior in laser chemical micro machining of metals. *J. Manuf. Mater. Process.* **2**, 54 (2018). <https://doi.org/10.3390/jmmp2030054>
- [Mes14] Messaoudi, H., Mehrafsun, S., Vollertsen, F.: Influence of the etchant on material removal geometry in laser chemical machining. In: *Proceedings of the 4th International Conference on Nanomanufacturing (nanoMan 2014)*, pp. 1–5 (2014)
- [Mes17a] Messaoudi, H., Eckert, S., Vollertsen, F.: Thermal analysis of laser chemical machining: part I: static irradiation. *Mater. Sci. Appl.* **8**, 685–707 (2017). <https://doi.org/10.4236/msa.2017.810049>

- [Mes17b] Messaoudi, H., Hauser, O., Matson, A., Mehrafsun, S., Vollertsen, F.: Fertigungsqualität laserchemisch hergestellter Mikroumformwerkzeuge, In: Vollertsen, F., Hopmann, C., Schulze, V., Wulfsberg, J. (eds.) Fachbeiträge 8. Kolloquium Mikroproduktion. BIAS Verlag, pp. 171–178 (2017). ISBN: 978-3-933762-56-6 (online)
- [Mes18] Messaoudi, H., Böhmernann, F., Mikulewitsch, M., von Freyberg, A., Fischer, A., Vollertsen, F.: Chances and limitations in the application of laser chemical machining for the manufacture of micro forming dies. In: Proceedings of the 5th International Conference on New Forming Technology (ICNFT2018), MATEC Web of Conferences 190, pp. 15010 (2018)
- [Mes18a] Messaoudi, H., Brand, D., Vollertsen, F.: Removal characteristics of high-speed steel in laser chemical machining. In: 14th International Symposium on Electrochemical Machining Technology INSECT2018, pp. 47–53 (2018)
- [Mik17] Mikulewitsch, M., von Freyberg, A., Fischer, A.: Adaptive Qualitätsregelung für die laserchemische Fertigung von Mikroumformwerkzeugen, In: Vollertsen, F., Hopmann, C., Schulze, V., Wulfsberg, J. (eds.) Fachbeiträge 8. Kolloquium Mikroproduktion. BIAS Verlag, pp. 21–26 (2017). ISBN: 978-3-933762-56-6 (online)
- [Nak09] Nakashima, S., Sugioka, K., Midorikawa, K.: Fabrication of microchannels in single-crystal GaN by wet chemical-assisted femtosecond-laser ablation. *Appl. Surf. Sci.* **255**, 9770–9774 (2009)
- [Nie18] Nielsen, C.V., Bay, N.: Review of friction modeling in metal forming processes. *J. Mater. Process. Technol.* **255**, 234–241 (2018)
- [Now94] Nowak, R., Metev, S., Sepold, G.: Laser chemical etching of metals in liquids. *Mater. Manuf. Process.* **9**(4), 429–435 (1994)
- [Now96] Nowak, R., Metev, S.: Thermochemical laser etching of stainless steel and titanium in liquids. *Appl. Phys. A* **63**, 133–138 (1996)
- [Paj06] Pajak, P.T., De Silva, A.K.M., Harrison, D.K., McGeough, J.A.: Precision and efficiency of laser assisted jet electrochemical machining. *Precis. Eng.* **30**, 288–298 (2006)
- [Pau96] Paul, E., Evans C.J.: Chemical aspects of tool wear in single point diamond turning. *Precis. Eng.* **18**, 4–19 (1996)
- [Pio11] Piotrowska-Kurczewski, I., Vehmeyer, J.: Simulation model for micro-milling operations and surface generation. *Adv. Mater. Res.* **223**, 849–858 (2011)
- [Pio15] Piotrowska, I., Vehmeyer, J., Gralla, P., Böhmernann, F., Elsner-Dörge, F., Riemer, O., Maaß, P.: Reduzierung der Formabweichung beim Mikrofräsen, Tagungsband 7. Kolloquium Mikroproduktion in Aachen vom 16. bis 17. November 2015, IKV Aachen, pp. 23–30 (2015)
- [Qia14] Qiang, H., Chen, J., Han, B., Shen, Z-H., Lu, J., Ni, X-W.: Study of underwater laser propulsion using different target materials. *Opt. Express* **22**(14), 17532–17545 (2014). <https://doi.org/10.1364/oe.22.017532>
- [Rie03] Rieder, A.: Keine Probleme mit Inversen Problemen–Eine Einführung in ihre stabile Lösung. Hrsgs. Vieweg & Sohn Verlag/ GWV Fachverlag GmbH, Wiesbaden (2003)
- [Rie16] Riemer, O., Elsner-Dörge, F.: Forces and form deviations in micro-milling of CoCr alloys for dental prostheses. In: The 5th International Conference on Nanomanufacturing (nanoMan), pp. 15–17 August 2016, Macau, China (2016)
- [Rie17a] Riemer, O., Elsner-Dörge, F., Willert, M., Meier, A.: Forces, form deviations and surface roughness in micro-milling of CoCr alloys for dental prostheses. *Int. J. Nanomanufacturing* (not yet published)
- [Rie17b] Riemer, O., Elsner-Dörge, F.: Charakteristische Kraftverläufe und resultierende Geometrieabweichungen beim Mikrofräsen von Strukturen in einer Kobalt-Chrom-Legierung, Tagungsband 8. Kolloquium Mikroproduktion (not yet published)
- [Rob17] Robert, C., Messaoudi, H., Riemer, O., Brinksmeier, E., Vollertsen, F.: Modifikation der Oberflächenfeingestalt monokristalliner Diamanten. In: Vollertsen, F., Hopmann, C., Schulze, V., Wulfsberg, J. (eds.) Fachbeiträge 8. Kolloquium Mikroproduktion. BIAS Verlag, pp. 187–194 (2017). ISBN: 978-3-933762-56-6

- [Rob17a] Robert, C., Riemer, O., Brinksmeier, E.: Mikrostrukturierung von monokristallinem Diamant mittels Reibungspolieren. *wt Werkstattstechnik online* 6, pp. 467–471 (2017)
- [Rob17b] Robert, C., Riemer, O., Brinksmeier, E.: Micro-structuring of single crystal diamond by ultrasonic assisted friction polishing. In: *Proceedings of the 17th International Conference of the European Society for Precision Engineering and Nanotechnology*, pp. 187–188 (2017). ISBN: 978-0-9957751-0-7
- [Rob17c] Robert, C., Riemer, O., Brinksmeier, E.: Bestimmung der Diamantabtragsmechanismen beim ultraschall-unterstützten Reibungspolieren, 8. Kolloquium Mikroproduktion. BIAS Verlag (2017). ISBN: 978-3-933762-56-6
- [Sch08a] Schulze Niehoff, H.: Entwicklung einer hochdynamischen, zweifachwirkenden Mikroumformpresse. BIAS-Verlag, Bremen, 2008, *Stahltechnik Band 33* (Dissertation)
- [Sch08b] Schulze Niehoff, H.: Entwicklung einer hochdynamischen, zweifachwirkenden Mikroumformpresse. Dissertation, BIAS Verlag (2008)
- [Sev18] Seven, J., Heinrich, L., Flosky, H.: Inline tool wear measurement in lateral micro upsetting. In: Vollertsen, F., Dean, T.A., Qin, Y., Yuan, S.J. (eds.) *5th International Conference on New Forming Technology (ICNFT2018)*, Bremen, MATEC Web Conference, vol. 190, pp. 15009 (2018)
- [Shi15] Shimizu, T., Yang, M., Manabe, K.: Classification of mesoscopic tribological properties under dry sliding friction for microforming operation. *Wear* **330–331**, 49–58 (2015)
- [Sill1a] De Silva, A.K.M., Pajak, P.T., McGeough, J.A., Harrison, D.K.: Thermal effects in laser assisted jet electrochemical machining. *CIRP Ann.* **60**(1), 243–246 (2011)
- [Sill1b] De Silva, A.K.M., Pajak, P.T., McGeough, J.A., Harrison, D.K.: Thermal effects in laser assisted jet electrochemical machining. *CIRP Ann. Manuf. Technol.* **60**(1), 243–246 (2011)
- [Ste09a] Stephen, A., Walther, R., Vollertsen, F.: Removal rate model for laser chemical micro etching. In: Ostendorf, A., Graf, T., Petring, D., Otto, A. (eds.) *Proceedings of the 5th International Lasers in Manufacturing Conference (LIM 2009)*. München, pp. 615–619 (2009)
- [Ste09b] Stephen, A., Walther, R., Vollertsen, F.: Removal rate model for laser chemical micro etching. In: *Proceedings of the 5th International WLT Conference on Lasers in Manufacturing*, pp. 615–619 (2009)
- [Ste10] Stephen, A., Vollertsen, F.: Mechanisms and processing limits in laser thermochemical machining. *CIRP Ann.* **59**(1), 251–254 (2010)
- [Ste11] Stephen, A.: Vollertsen, F., Bergmann, R.B. (eds.) *Elektrochemisches Laser-Jet-Verfahren zur Mikrostrukturierung von Metallen*. *Strahltechnik* 46. BIAS Verlag Bremen (2011)
- [Suh87] Suh, N.P., Saka, N.: Surface engineering. *CIRP Ann.* **36**(1) 403–408 (1987)
- [Suz03] Suzuki, K., Iwai, M., Uematsu, T., Yasunaga, N.: Material removal mechanism in dynamic friction polishing of diamond. *Key Eng. Mater.* **238–239**, 235–240 (2003)
- [Tat16] Tatsumi, N., Harano, K., Ito, T., Sumiya, H.: Polishing mechanism and surface damage analysis of type IIa single crystal diamond processed by mechanical and chemical polishing methods. *Diam. Relat. Mater.* **63**, 80–85 (2016)
- [Twa14] Twardy, S.: Funktionsgerechte Fertigung von Mikroumformwerkzeugen durch Mikrofräsen. Dissertation Universität von Bremen (2014)
- [Uen08] Ueno, F., Kato, C., Motooka, T., Ichikawa, S., Yamamoto, M.: Corrosion phenomenon of stainless steel in boiling nitric acid solution using large-scale mock-up of reduced pressurized evaporator. *J. Nucl. Sci. Technol.* **45**(10), 1091–1097 (2008)
- [Uhl14] Uhlmann, E., Oberschmidt, D., Kuche, Y., Löwenstein, A.: Cutting edge preparation of micro milling tools. In: *6th CIRP International Conference on High Performance Cutting, HPC2014*, *Procedia CIRP*, vol. 14, pp. 349–354 (2014)
- [Veh12] Vehmeyer, J., Piotrowska-Kurczewski, I., Twardy, S.: A surface generation model for micro cutting processes with geometrically defined cutting edges. In: *Proceedings of the 37th International MATADOR Conference*, pp. 149–152 (2012)

- [Veh15a] Vehmeyer, J., Piotrowska, I., Böhmermann, F., Riemer, O., Maaß, P.: Least-squares based parameter identification for a function-related surface optimisation in micro ball-end milling. In: Proceedings of the 15th CIRP Conference on Modelling of Machining Operations (15th CMMO), Procedia CIRP, vol. 31, pp. 276–281 (2015)
- [Veh15b] Vehmeyer, J., Piotrowska, I., Böhmermann, F., Riemer, O., Maaß, P.: Least-squares based parameter identification for a function-related surface optimisation in micro-ball-end milling. In: Proceedings of the 15th CIRP Conference on Modelling of Machining Operations (15th CMMO), Procedia CIRP, vol. 31, pp. 276–281 (2015)
- [Veh17a] Vehmeyer, J.: Geometrische Modellierung und funktionsbezogene Optimierung der inhärenten Textur von Mikrofräsprozessen, Dissertationsschrift, Universität Bremen, Logos Verlag Berlin (2017)
- [Veh17b] Vehmeyer, J.: Geometrische Modellierung und funktionsbezogene Optimierung der inhärenten Textur von Mikrofräsprozessen, Logos Verlag Berlin (2017), Universität Bremen, Dissertation (2016)
- [Ver01] Vermeulen, M., Scheers, J.: Micro-hydrodynamic effects in EBT textured steel sheet. Int. J. Mach. Tools Manuf. **41**, 1941–1951 (2001)
- [Vol08] Vollertsen, F.: Categories of size effects. Prod. Eng. Res. Dev. **2**, 377–383 (2018)
- [Vol10] Vollertsen, F., Biermann, D., Hansen, H.N., Jawahir, I.S., Kuzman, K.: Size effects in manufacturing of metallic components. CIRP Ann. Manuf. Technol. **58**(2), 566–587 (2009)
- [Vol15] Vollertsen, F., Flosky, H., Seefeld, T.: Dry metal forming—a green approach. In: Tekkaya, A.E., Homberg, W., Brosius, A. (eds.) 60 Excellent Inventions in Metal Forming, pp. 119–123 (2015)
- [Vol18] Vollertsen, F.: Schwerpunktprogramm SPP 1676. BIAS GmbH. <http://www.trockenumformen.de/>. Accessed 21 June 2018
- [Wan06] Wang, C.Y., Chen, C., Song, Y.X.: Mechanochemical polishing of single crystal diamond with mixture of oxidizing agents. Key Eng. Mater. **315–316**, 852–855 (2006)
- [Wei01] Weima, J.A., Fahrner, W.R., Job, R.: Experimental investigation of the parameter dependency of the removal rate of thermochemically polished CVD diamond films. J. Solid State Electrochem. **5**, 112–118 (2001)
- [Wen12] Wendler-Kalsch, E., Gräfen, H.: Korrosionsschadenkunde. Nachdr. der 1. Aufl. 1998. Springer Vieweg, Berlin (2012)
- [Whe92] Wheeler, D.J., Chambers, D.S.: Understanding Statistical Process Control. SPC Press (1992)
- [Whi11] Whitelaw, J.H.: Convective heat transfer, thermopedia: guide to thermodynamics. Heat Mass Transf. Fluids Eng. (2011). https://doi.org/10.1615/AtoZ.c.convective_heat_transfer
- [Wol84] Wolf, G.W.: A mathematical model of cartographic generalization. Geo-processing 2 (1984) 271–286
- [Wol93] Wolf, G.W.: Data structures for the topological characterization of topographic surfaces. In: Proceedings of the 6th Colloque Européen de Géographie Théorique et Quantitative, vol. 6, pp. 24–34 (1993)
- [Yav94] Yavas, O., Oltra, R., Kerrec, O.: Enhancement of pulsed laser removal of metal oxides by electrochemical control. Appl. Phys. A **63**, 321–326 (1994)
- [Zha12] Zhang, P., Renken, V., Goch, G.: Cross-plane quality control concept of the bearing ring production. Materialwissenschaft und Werkstofftechnik **43**(1–2), 37–41 (2012)
- [Zha15] Zhang, P., Goch, G.: A quality controlled laser-chemical process for micro metal machining. Product. Eng. **9**(5), 577–583 (2015)
- [Zha17] Zhang, P., von Freyberg, A., Fischer, A.: Closed-loop quality control system for laser chemical machining in metal micro-production. Int. J. Adv. Manuf. Technol. **93**, 3693–3703 (2017)

Open Access This chapter is licensed under the terms of the Creative Commons Attribution 4.0 International License (<http://creativecommons.org/licenses/by/4.0/>), which permits use, sharing, adaptation, distribution and reproduction in any medium or format, as long as you give appropriate credit to the original author(s) and the source, provide a link to the Creative Commons license and indicate if changes were made.

The images or other third party material in this chapter are included in the chapter's Creative Commons license, unless indicated otherwise in a credit line to the material. If material is not included in the chapter's Creative Commons license and your intended use is not permitted by statutory regulation or exceeds the permitted use, you will need to obtain permission directly from the copyright holder.

